

© 2022 Hyungjoo Seo

IMPEDANCE- AND SPATIAL-DOMAIN ALIASING IN INTERFERENCE
MANAGEMENT TECHNIQUES

BY

HYUNGJOO SEO

DISSERTATION

Submitted in partial fulfillment of the requirements
for the degree of Doctor of Philosophy in Electrical and Computer Engineering
in the Graduate College of the
University of Illinois Urbana-Champaign, 2022

Urbana, Illinois

Doctoral Committee:

Assistant Professor Jin Zhou, Chair
Professor Romit Roy Choudhury
Professor Pavan Hanumolu
Associate Professor Songbin Gong

Abstract

In modern communication systems, interference management is crucial in recovering desired target signals corrupted by the channel from various unknown interference and noise.

In radio-frequency (RF) spectral interference problems in wireless communication, interference-tolerant RF front-end receiver design is becoming increasingly challenging, as modern wireless devices have to support many frequency bands with numerous front-end switches and costly acoustic filters. Since acoustic filters are mostly not tunable, $O(K)$ acoustic filters are needed to cover K bands with switches to select the right filters. On top of that, the cost and size of next-generation RF front-ends are further stressed by the new trends in multi-in-multi-out (MIMO), broadband, and dynamic spectrum access which exacerbates the front-end design issues. As a solution to this problem, we propose blocker-tolerant programmable RF front-end receiver architecture, called mixer-first acoustic-filtering front end, which utilizes N -path structure to translate the frequency response of $O(1)$ acoustic filter to cover $O(K)$ bands over wide range of continuous frequencies with minimal loss penalty. Also, we demystify the impedance aliasing phenomenon caused by uncertainty at the interface between two distinct domains such as acoustic-electromagnetic interface.

Also, aliasing property in spatial domain has been investigated to deal with spatial interference management problem. Unlike conventional approaches to prevent spatial aliasing issues in multi-sensor linear array, we propose a way to exploit the phenomenon to solve under-determined blind multi-target localization and source separation problems by aligning the interferers in spatial domain.

To my parents and family, for their love and support.

Acknowledgments

I would like to sincerely thank to my advisor Prof. Zhou for his absolute support of my Ph.D. research. His advice helped me in all the time of research including this thesis. He spent a tremendous amount of time to teach me how to research, write papers, and present my work. I feel extremely fortunate to have had the opportunity to learn from him and greatly appreciate his patience. I also would like to thank the rest of my doctoral committee: Prof. Roy Choudhury, Prof. Hanumolu and Prof. Gong. Their insightful comments and feedback improved my research from various perspectives. I thank all my lab colleagues and friends for the collaborations and the discussions. They helped me overcome setbacks and stay focused. The interactions with them made my time in graduate school much more fun. Lastly but most importantly, I would like to thank my family, whose endless love and encouragement made this dissertation possible. They have been and will be a constant source of love, support, and strength throughout my life.

Table of contents

Chapter 1	Introduction and Basic Definitions	1
Chapter 2	A Passive-Mixer-First Acoustic-Filtering Superheterodyne RF Front-End for Spectral Interference	13
Chapter 3	A Passive-Mixer-First Acoustic-Filtering Receiver Chipset Using Mixed-domain Recombination for Spectral Interference	49
Chapter 4	Rotational Motion for Angular Aliasing and Source Enhancement	84
Chapter 5	Conclusion and Future Works	100
References	107
Appendix A	Derivation of full equation solution with general LTI impedance response	121
Appendix B	Frequency Planning for Optimal IF Frequency Selection for Super-heterodyne Architectures	126

Chapter 1

Introduction and Basic Definitions

In nature, information transfer, so-called communication, happens mostly in the form of signals through the channel. Ideally, the transmitter sends out the target signal that contains information of interest to the receiver. However, signals are ubiquitous, whether or not they contain information; thus, the channel is typically full of noise and interference [1]. Interference includes not only natural ones such as a rainbow or the sound of the wind but also artificially modulated ones such as Wi-Fi and human speech signals. And these could easily interfere with the desired signal that the transmitter sent out, creating a mixture at the receiver. Therefore, dealing with such interference, so-called the interference management, is critical in order to properly recover desired target signal from the mixture.

While the definition may vary depending on signal and system types, interference management is generally a broad comprehensive terminology that includes steps such as sensing, decision making, and treatment [2], [3]. The sensing step is to explore the environment to identify the interferers. It allows the receiver to acquire features, pre-defined or learned, that could distinguish the target and interference signals. Next, decisions can be made on what action should be taken to recover the target signal the most by meeting optimal decision criteria that evaluates quality of recovery, such as signal-to-interference-and-noise-ratio (SINR) or signal-to-distortion-ratio (SDR). Lastly, based on decision, treatment step executes a adequate processing on received mixture data to mitigate the interference by leaving only the target signal.

As signals are composed of waves that propagate, the solution for interference management highly depends on the type of waves whether it is an electromagnetic (EM) wave such as radio-frequency (RF) and optics that follows Maxwell equation, or mechanical wave such as water, acoustic, seismic waves that are governed by Newton's law, or even a matter wave that requires quantum mechanics [4]. In this thesis, we constrain our interests into the first two types of waves in the application of radio-frequency (RF) spectrum for the former,

and audible, for humans, sound signal spectrum for the latter. In the introduction section, interference management challenges in each RF/wireless and acoustic domain are discussed, followed by the author’s contribution on interference management relating to the aliasing phenomena.

1.1 Aliasing Phenomenon

In signal processing and various physics disciplines, *aliasing* refers to an phenomenon that makes different signals indistinguishable when sampled [5]. In general, sampling action is to create discrete signals from continuous signals and can happen in various domains such as time and space.

1.1.1 Temporal Aliasing

When sampling happens in time domain, it’s called *temporal aliasing*, and can be mathematically shown in the following manner. From Fourier series[6] or transform[7], any practical signals can be represented as the summation of sinusoidal signals with different frequencies. Thus, each sinusoidal signal $s(t)$ that has a frequency value of f with the phase of ϕ can be represented as:

$$s(t) = \cos(2\pi ft + \phi) \tag{1.1}$$

where t represents continuous real time points. Now, let us consider sampling this continuous signal $s(t)$ with a sampling period of $T_s = \frac{1}{f_s}$ [sec] that we can represent $t = nT_s$ where n is n -th sample point. Then, sampled signal $s[n]$ can be expressed as:

$$s[n] = \cos(2\pi fnT_s + \phi) = \cos(2\pi(f + kf_s)nT_s + \phi) \tag{1.2}$$

In (1.2), second equality term holds for all n values as long as k is integer values since $f_sT_s = 1$. Thus, this means that we cannot distinguish between sinusoidal signals whose frequencies have a form of $f + kf_s$ with same phase. Note that, if there are two sinusoidal tones co-existing at frequencies of $f_0 + Pf_s$ and $f_0 + Qf_s$ where P and Q are integers, for instance, you would sense these tones as if there were two identical tones with same frequencies. Thus, there is intrinsic uncertainty of original frequency of a signal when measured, not to mention we cannot be sure of number of original signals which might have folded on top of each other when measured due to aliasing.

One can prevent aliasing by making f_s larger than twice the maximum frequency content of the signal, based on ”Nyquist-Shannon Sampling Theorem” that states that information of

any signal $s(t)$ that contains no frequency higher than B Hz can completely be recovered by sampling with, at least $2B$ Hz [8]. However, if we do not know maximum frequency content of interfering signals, it is not easy to prevent aliasing.

1.1.2 Spatial Aliasing

When sampling happens over space, it is called spatial aliasing, and if spatially repeating signal content has higher frequency than half the sampling frequency, then original signal patterns cannot be fully recovered because information has been lost. For instance, when the signal is an image and sampling space is 2-dimensional plane, image that contains repeating patterns appearing more frequently than twice the representing pixel size cannot represent original continuous image content any more due to spatial aliasing. Examples are shown in Fig. 1.1 and 1.2, where densely drawn patterns images are distorted after resampled with lower spatial frequency (low-pass filter is applied afterwards) .

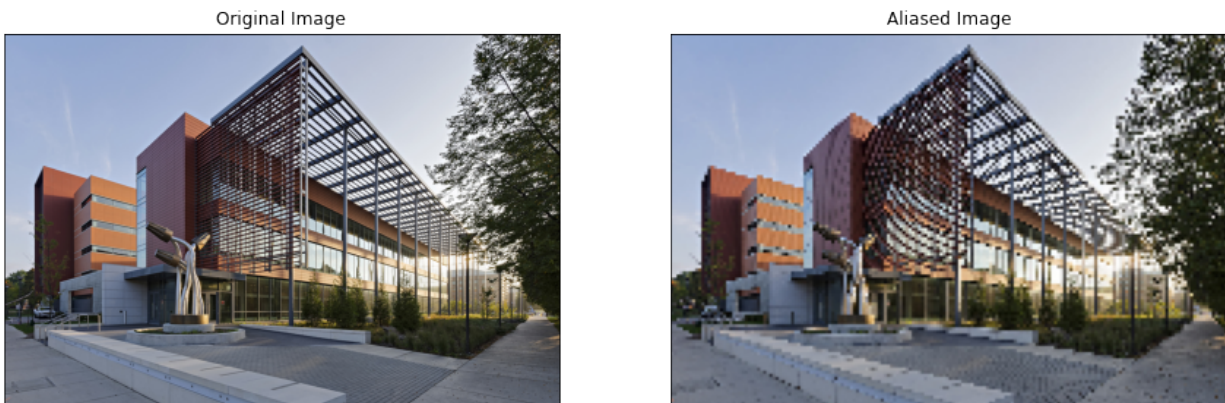


Figure 1.1: University of Illinois Electrical and Computer Engineering Building (left) which has frequent grid patterns that are effected by aliasing due to low-resolution pixels (right).

Now, similar things can be said in regard to a continuous signal $s(t)$ generated from far distance approaching towards sensor arrays with a spacing of d as in Fig. 1.3(a) with the angle of θ . Since these sensor arrays take measurements samples at different spatial locations with respect to incident angle θ , effective sampling spacing is $d\cos\theta$. Recall that when we sample over time, frequency is defined as the inverse of time. Similarly, spatial frequency is defined as the inverse of spacing where sampling is taken place. This is intuitively making sense because if repeating patterns have high frequency, then repeating spacing should be small. Thus, amongst all sinusoidal tone composing of $s(t)$ [6], maximum spatial frequency content is the inverse of wavelength of maximum frequency content of $s(t)$, shown as $\frac{1}{\lambda_{fmax}}$. As spatial sampling frequency is $1/d$, we can find the criteria for preventing spatial aliasing



Figure 1.2: Original picture of a baby (left) which has relatively-high frequency patterns on his shirt corrupted by aliasing effect due to low-resolution pixels (right).

from Nyquist-Shannon Sampling Theorem by enforcing the following condition for sensor spacing d :

$$\begin{aligned}
 2 \times f_{max} \leq f_s &\Leftrightarrow 2 \times \frac{1}{\lambda_{fmax}} \leq \frac{1}{d \cos \theta} \\
 &\Leftrightarrow d \leq \frac{\lambda_{fmax}}{2 \cos \theta} \leq \frac{\lambda_{fmax}}{2}
 \end{aligned} \tag{1.3}$$

Therefore, spacing between linear sensor array d should be lower than half the wavelength of maximum signal frequency content for any angle $\theta \in [-180, 180]$ to prevent the spatial aliasing effect. Now, what does it mean that we do not have ambiguity of spatial frequency for the signal along the axis of sensor array for any given incident angle θ ? This means that we have unique phase difference between one sensor and adjacent sensor nodes for each θ angle **along the axis of array**. However, since we do not have information along the perpendicular axis of the array, we cannot distinguish whether the angle is θ or $-\theta$, so called front-back ambiguity, which will be revisited in Chapter 4, focusing on how to exploit it instead of eliminating it.

In fact, this front-back ambiguity property can easily be imagined with mathematical concept of a hyperbola. Since we are interested in phase difference between two adjacent sensor nodes within a linear sensor array, the phase difference for tone with frequency f , $\Delta\phi = 2\pi f\Delta\tau$ where $\Delta\tau$ is delay difference. If we think about a hyperbola that has two focal points at sensor locations, hyperbola is drawn from its definition: $R_1 - R_2$ becomes constant where R_i ($i = 1, 2$) represents distance from two focal points to the target point as shown in Fig. 1.3(b). That is,

$$\Delta\tau = \frac{R_1}{v_p} - \frac{R_2}{v_p} = \frac{R_1 - R_2}{v_p} \quad (1.4)$$

Therefore, every point along this hyperbola yields the same delay difference, which is a same phase difference for a single tone, between two sensor nodes. And since this hyperbola approaches to asymptotic lines as the distance R_i increases at both directions (top and bottom), two far-field signals can generate same delay values which create delay-domain ambiguity (Fig. 1.3(b)).

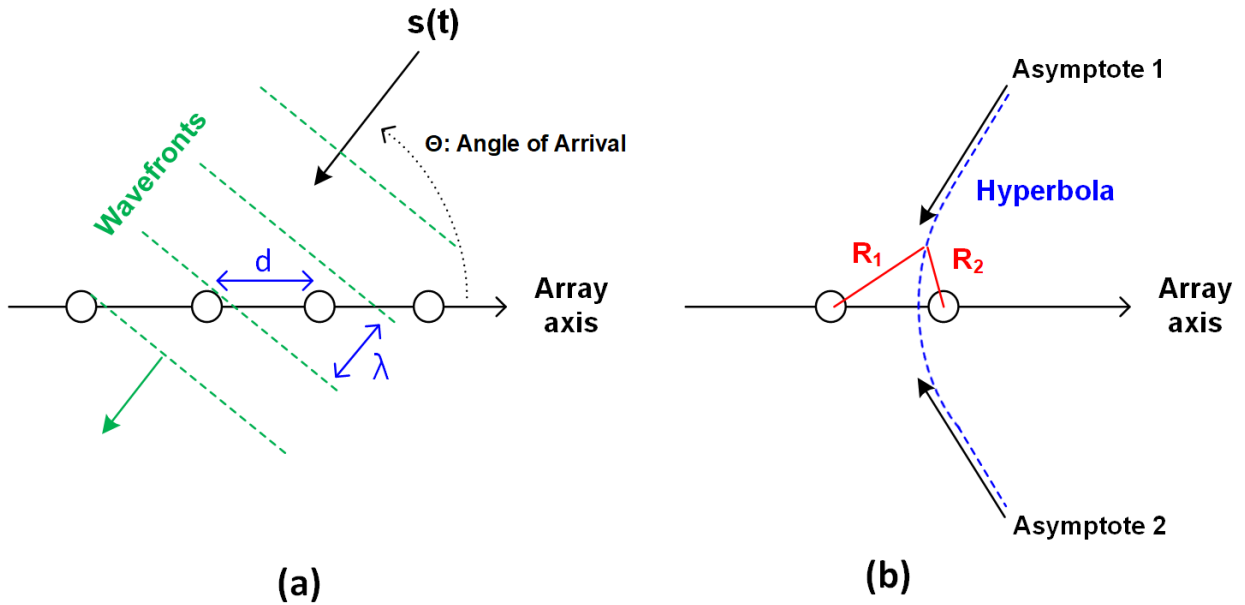


Figure 1.3: (a) Far-field signal from angle θ impinging on linear sensor arrays seen from top, (b) Hyperbola approaching asymptotic lines and front-back ambiguity.

1.2 Radio-frequency Signal Interference

One of the key challenges in RF/wireless communication system is that it requires RF front-ends at both transmitter and receiver sides. Fundamental hardware trade-off among

form factor, power consumption, bandwidth, and cost makes it difficult to perform the direct information exchange either in baseband or RF frequencies without any frequency conversion. For instance, communicating directly at baseband from DC to 100 MHz makes antenna-front-end form factor over 10 meters, which is too large for majority of mobile applications. Also, communicating directly at RF above GHz frequencies requires either direct-RF signal processing capability or ADC operating bandwidth above GHz. And it is challenging to meet such hardware specifications in both cases. Therefore, either super-heterodyne or direct-conversion architectures are adopted mostly in modern transceiver designs [9]. In such architectures, a carrier signal carries information, modulated at baseband with a finite bandwidth, through the channel from transmitter to receiver occupying one time-frequency bin regardless of duplexing method. Interference signal could show up in the channel corrupting the time-frequency bin; thus, it is desirable to sense the occupancy of each bin before transmitting the signal. Even if interference does not exist in the frequency of interest, it is still important to protect the receiver as much as one could because receiver can be jammed from reciprocal mixing [9], [10] if interferers exist in adjacent frequency.

However, such interference-tolerant RF front-end receiver design is becoming increasingly challenging as a modern device has to support many frequency bands with numerous front-end switches and acoustic filters [11]. Acoustic resonator-based bandpass filters are widely adopted in wireless applications because they show exceptional resonator performance in terms of loss and selectivity compared to electromagnetic counterparts in GHz frequency range. Critical downsides of using these acoustic devices in wireless transceiver are high cost and large area, due to the fact that it is not easy to tune the acoustic filter center frequency. Thus, more frequency band means more filters. On top of that, the cost and size of next-generation RF front-ends are further stressed by the new trends multi-in-multi-out (MIMO), broadband, and dynamic spectrum access which exacerbate the issue [12]–[14].

To deal with this issue, many silicon-based integrated circuit designs for monolithic reconfigurable RF front-ends such as N-path filters and mixer-first receivers have been proposed as possible alternatives to numerous fixed-frequency acoustic filters [15]. The key principle is to up-convert the sharp filter response created at baseband to desired RF frequency with minimal conversion loss. In terms of performance, Q-factor of filter response at baseband can be boosted by shifting up the frequency response because 3-dB bandwidth almost remains the same, but center frequency goes up by up-conversion, ideally. Also, for tuning capability, such response can be shifted upto any RF frequency of interest and continuous wide tuning of center frequency is possible in theory. For such frequency translation of filter LTI response can be implemented with a mixer circuit either through a nonlinear [16], [17] or time-varying system [18]. Because this up-converted filter structure should retain its operation even when

strong spectral interferers appear at the RF front-end, passive switch-based non-overlapping branches, so called a N-path structure, is a good candidate as it shows high linearity over active switching mixers or nonlinearity-based mixers [15].

1.3 N-path Structure

Fig. 1.4 shows the N-path structure that contains input power source and N identical branches containing switches and LTI impedance loads $Z_L(\omega)$. Each switch is closed in a periodic non-overlapping manner with a period of T_{LO} and duty cycle of $1/N$ driven by switching function $SW_i(t)$ where $i = 1$ to N . Here, LO represents local oscillator by which clocks are driven.

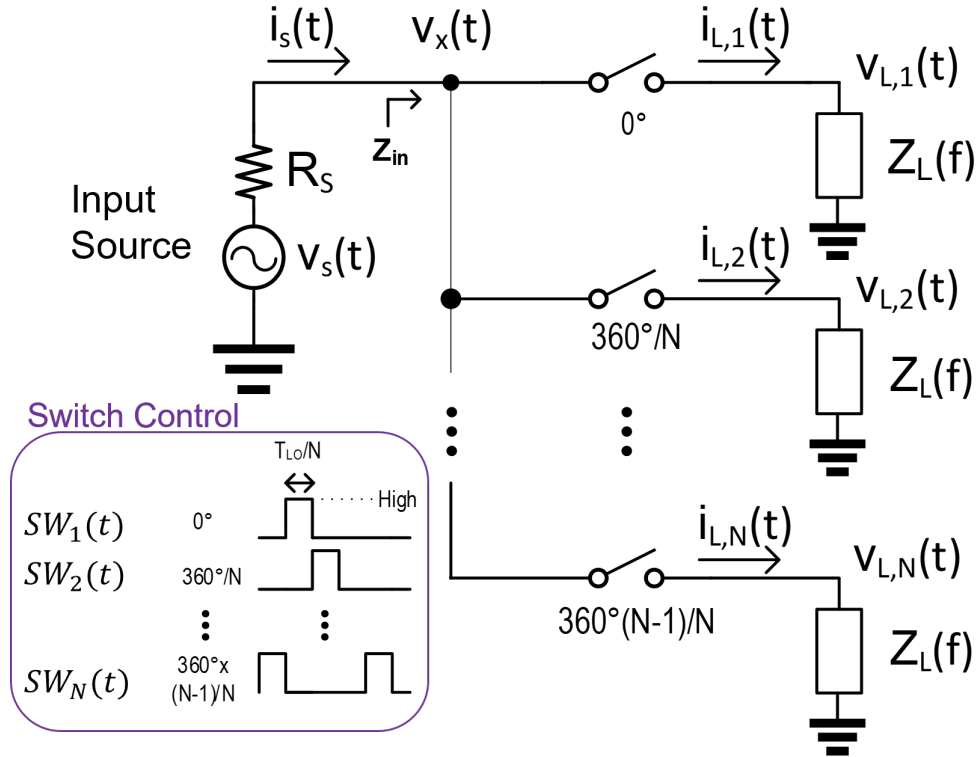


Figure 1.4: N-path structure with non-overlapping branches containing switches and identical LTI loads

When $Z_L(\omega)$ loads are generic LTI responses from current to voltage at i -th path, currently flowing through i -th load $i_{L,i}$ is given as:

$$i_{L,i}(t) = SW_i(t)i_s(t) \quad (1.5)$$

where $i_s(t)$ represents current coming out of input source.

By applying Fourier transform,

$$\begin{aligned}
I_{L,i}(\omega) &= SW_i * I_S(\omega) \\
&= \sum_{n=-\infty}^{\infty} a_{n,i} \delta(\omega - n\omega_{LO}) * I_S(\omega) \\
&= \sum_{n=-\infty}^{\infty} a_{n,i} I_S(\omega - n\omega_{LO}),
\end{aligned} \tag{1.6}$$

when switch function at i-th branch is defined as below:

$$SW_i(t) = \sum_{n=-\infty}^{\infty} a_{n,i} e^{-j\frac{2\pi nt}{T_{LO}}}$$

$$SW_i(\omega) = \sum_{n=-\infty}^{\infty} a_{n,i} \delta(\omega - n\omega_{LO})$$

where

$$a_{n,i} = \frac{\text{sinc}\left(\frac{n\pi}{N}\right)}{N} e^{-j\frac{n\pi}{N}(2i-1)}$$

Next, output of each LTI load response $V_{L,i}(\omega)$ is given as:

$$V_{L,i}(\omega) = I_{L,i}(\omega) Z_L \omega = \sum_{n=-\infty}^{\infty} a_{n,i} Z_L(\omega) I_S(\omega - n\omega_{LO}) \tag{1.7}$$

Each voltage created by input current at i-th branch from LTI response $Z_L(\omega)$ is also sampled back to the shared branch x. Thus, voltage at x is given as:

$$v_x(t) = \sum_{i=1}^N SW_i(t) v_{L,i}(t) \tag{1.8}$$

In frequency domain, voltage at shared node is given as:

$$\begin{aligned}
V_x(\omega) &= \sum_{i=1}^N SW_i(\omega) * V_{L,i}(\omega) \\
&= \sum_{i=1}^N \sum_{m=-\infty}^{\infty} a_{m,i} V_{L,i}(\omega - m\omega_{LO}) \\
&= \sum_{i=1}^N \sum_{m=-\infty}^{\infty} \sum_{n=-\infty}^{\infty} a_{m,i} a_{n,i} Z_L(\omega - n\omega_{LO}) I_S(\omega - (m+n)\omega_{LO})
\end{aligned} \tag{1.9}$$

Since complex values cancel out leaving N in-phase vectors,

$$V_x(\omega) = N \sum_{m=-\infty}^{\infty} \sum_{n=-\infty}^{\infty} a_m a_n Z_L(\omega - n\omega_{LO}) I_S(\omega - (m+n)\omega_{LO}) \quad (1.10)$$

where $m+n = Nk$, k is integer and $a_n = \frac{\text{sinc}(\frac{n\pi}{N})}{N} e^{j\frac{n\pi}{N}}$.

This result means that N-path structure driven by input current $I_S(\omega)$ at single frequency creates output response of $V_x(\omega)$ in multiple frequencies at $\omega - Nk\omega_{LO}$ where k is integer.

This interesting time-varying response can be represented as a two-step process as shown in Fig. 1.5 where mixer diagram is utilized for switch-based mixing for simplicity.

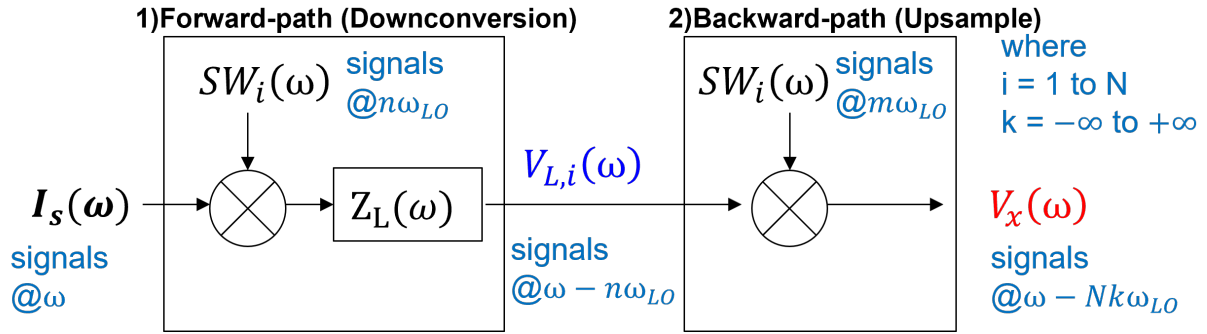


Figure 1.5: N-path structure's current to voltage time-varying response as a two-step process

For a current input at ω , impedance at ω can be found by:

$$Z_{x,open}(\omega) = \frac{V_x(\omega)}{I_S(\omega)} = \sum_{n=-\infty}^{\infty} \gamma_n Z_L(\omega - n\omega_{LO}) \quad (1.11)$$

where harmonic gain $\gamma_n = \frac{1}{N} \text{sinc}^2(\frac{n\pi}{N})$. This result is interesting because we can observe impedances at each frequency are folded on top of each other essentially creating aliasing in impedance domain [5]. This is intuitive, since we are sampling each current periodically using clock-driven switches then takes voltage values as outputs of LTI responses. Thus, a form of temporal aliasing while a sampled value is not a finite value but short sections of signals; thus, it has sinc-based coefficients.

In most of prior works [15], [19]–[21], load impedance has a low-pass response where peak is at DC and RF frequency is designed to be ω_{LO} apart from DC. This means that impedance seen at the N-path load is given as, $n = 1$ for (1.11),

$$Z_{x,1} = \gamma_1 Z_L(\omega - \omega_{LO})$$

As can be seen, original low-pass response is upconverted by ω_{LO} with a scaling factor.

What if the load response $Z_L(\omega)$ is not low-pass response as assumed in most of literature? If the load impedance is general LTI response, input impedance would just be (1.11) where impedance values at each harmonic location are summed up after scaled by respective harmonic gains. Therefore, all non-zero harmonic responses are aliased on top of each other, then appear at the single input frequency ω . This phenomenon is not desirable in filter applications in terms of input matching and wideband operation. Details are discussed in Chapter 2 and 3.

Also, it is important to note that the analysis provided in previous section is not a steady-state response because we assumed that current initially goes into the N-path structure and found the corresponding output step-by-step fashion. In reality, voltage generated from N-path structure at multiple frequencies generates new set of currents in respective frequencies re-starting the original current-input to voltage-out process repeatedly on its own until it converged. This situation can be depicted as in Fig. 1.6. Full derivation of steady-state condition is provided in A.

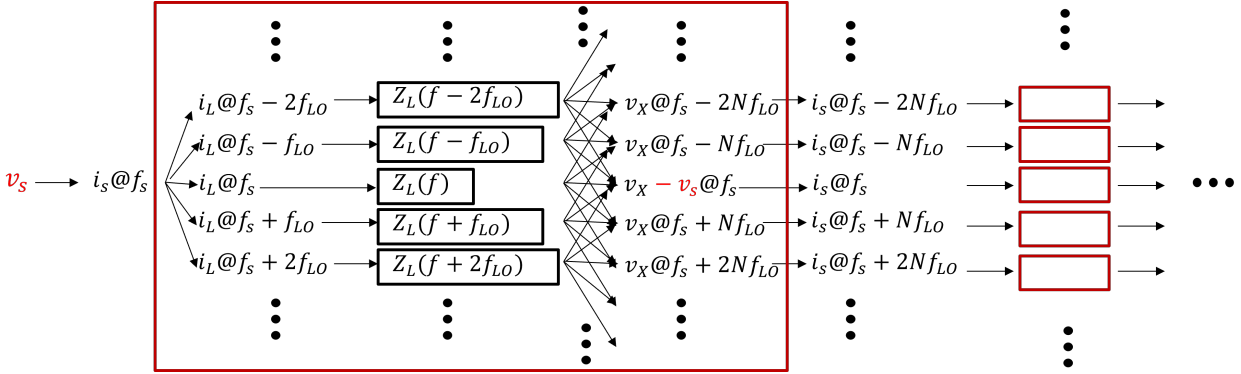


Figure 1.6: N-path structure's Harmonically Coupled Feedback Process

1.4 Audio Signal Interference

Unlike the case of radio-frequency signal, audible sound signal does not need up and down conversion because its frequency range is around DC to 20 kHz. Therefore, decent hardware performance on analog transceiver, microphone, speaker is achievable compared to that of RF case, even in direct baseband-to-baseband communication case.

However, there are different types of unique challenges in audio interference management. First, audio signals, e.g. speech sound from the human vocal system, are not generated by sophisticated machines like most of RF signals that the audio receiver should always be transparent to entire audible frequency range. Thus, desired signal and interference signals are

mixed at the microphone in whole continuous spectrum from DC to maximum frequency of interest due to lack of up- and down-conversion steps. This means front-end signal processing needs to deal with a wide range of spectrum with as fine granularity as possible to recover the entire spectrum of target signal. And this is challenging because interference and target signal could mix differently at each frequency [22].

Second, there is hardly any regulation on frequency band or modulation scheme in sound signal communication. In RF/wireless applications, the Federal Communications Commission (FCC) puts firm regulation on frequency bands depending on purpose of usage [23] so that collision between different signal usage, i.e. WiFi and GPS, does not happen. However, many audio sound signals are naturally generated ambient signal where there is no such restriction. What is more, desired target signal also tends to change depending on the condition of the speaker, context of the speech, etc. Therefore, separating the target and interference signals needs to be done in a blind manner, meaning the receiver cannot make too much assumption on impinging signals as it is often done in RF/wireless through preamble check, for instance.

For above-mentioned reasons, blind source separation (BSS) is crucial in mixture problems such as cocktail party problem [24], [25]. There are various source separation-based interference management algorithms in the literature [26]–[28] and most approaches rely on learning the features of each source signals from the mixture, since each source signal typically contains distinctive differences in some aspects. Examples of such distinctive aspects are spatial features where each source typically come from different angles of arrival (AoA) [29], stochastic properties where each source may have different type of distributions [30], and independence among each signals where there is no relevance between dog barking and bird chirping [31].

1.5 Thesis Contribution

The contribution of this thesis includes identification and analysis of an "impedance aliasing problem" in a linear-periodically-time-varying (LPTV) system where uncertainty exists between two distinct domain interfaces such as acoustic-EM. Acoustic-EM interface is common in modern RF/wireless transceivers that contain numerous costly acoustic filters in between silicon-based circuits especially in new standard of 5G or Software-defined radio (SDR) applications. We propose a novel programmable interference-tolerant, super-heterodyne receiver architecture solution utilizing LPTV circuits connecting to a limited number of acoustic filters to eliminate bulky and expensive acoustic filter banks.

In this domain, we propose two types of receiver architectures that utilize only one or two acoustic bandpass filters to cover the entire band of interest by programmable LO

tuning while meeting input impedance matching condition. For both architectures, N-path structure is adopted for frequency-translating the acoustic bandpass filter response at the antenna interface directly with minimal conversion loss, so called mixer-first acoustic-filtering front-end. Impedance shaper is introduced as an anti-aliasing filter, of impedance domain, in between CMOS-acoustic interface to prevent impedance aliasing phenomena. First type recombines multi-phase signals splitted by N-path structure using all-passive recombination network right before the acoustic device. Second version recombines these signals both at the intermediate frequency (IF) and baseband (BB). Details on each type are introduced in Chapter 2 and 3 respectively.

The next contribution is on utilization of spatial aliasing phenomenon for audio interference management problem. Instead of suppressing the spatial aliasing in multi-sensor array processing, we exploit it to come up with an algorithmic solution for the under-determined blind multi-target localization and source separation problem when there are more number of unidentified interfering signals than that of receiver sensor nodes. This seemingly ill-defined under-determined system has infinite number of solutions, meaning there is intrinsic information loss. But we propose that spatial aliasing through intentional motion-based interference alignment could reduce information loss in target source recovery when receiver array is surrounded by multiple independent sound sources. Details are highlighted in Chapter 4.

Lastly, Chapter 5 concludes the thesis by summarizing ideas and introduces potential future works extended from contributions in previous chapters relating to aliasing properties.

Chapter 2

A Passive-Mixer-First Acoustic-Filtering Superheterodyne RF Front-End for Spectral Interference

**

2.1 Introduction

The ever-increasing demands on wireless communications and sensing have been making the electromagnetic (EM) spectrum, particularly the portion that is below 6 GHz, highly sought-after and congested. This makes RF filtering that suppresses strong out-of-band (OOB) interference indispensable.

Acoustic filters using surface-acoustic-wave (SAW) and bulk-acoustic-wave (BAW) technologies are deployed for many modern commodity mobile devices because of their low loss, steep filter transition band roll-off, high linearity, and compact form factors [13]. Unfortunately, these acoustic filters generally cannot be tuned across a wide frequency range and have somewhat fixed and pre-defined operation frequencies. As more frequency bands are set to become available in the near future, e.g. the advent of sub-6-GHz 5G, a whopping 100 filters are expected in a next-generation mobile device; this imposes significant challenges on RF front-ends in terms of cost, size, and design complexity [14].

A possible solution is to employ widely-tunable and compact RF filters to replace numerous fixed-frequency acoustic filters in a mobile device. Also, widely-tunable and compact RF filters are essential for future high-performance software-defined and intelligent radios operating in

**This chapter is adopted from author's own works [32], [33]

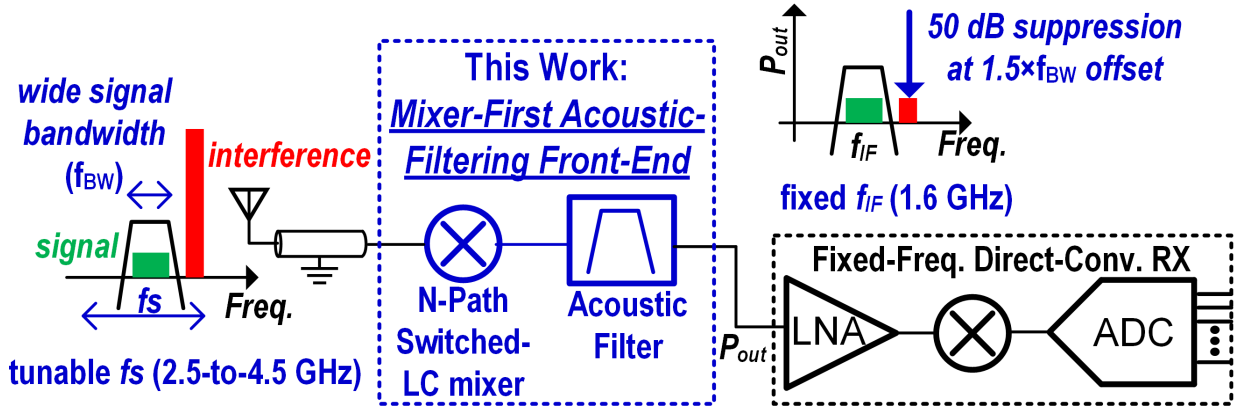


Figure 2.1: Mixer-first acoustic-filtering front-end: conceptual diagram.

a congested EM environment [34]. Hence, the development of such tunable RF filters has long been an important research topic.

Monolithic reconfigurable high-order band-pass filters using N -path switched-capacitor resonators have been reported recently [20], [35], [36]. However, due to lossy coupling networks, parasitic effects, and the need of multi-phase square-wave RF clocks, these filters have limited OOB rejection, moderate frequency tuning range, and do not perform well when operate beyond 3 GHz. High-order Q -enhanced LC -resonator-based RF band-pass filters at >3 GHz (e.g. [37]) have been demonstrated with widely-tunable operation frequency and bandwidth. However, Q -enhanced RF filters have large noise and degraded linearity as active components are utilized for achieving high- Q on chip. Widely-tunable mixer-first band-pass receivers that operate beyond 3 GHz have been reported (e.g. [38]–[41]) but have limited OOB linearity and suppression at close-in offset frequencies due to the low-order-filtering input impedance of their baseband amplifiers.

Tunable acoustic filters have also been demonstrated (e.g. employing ferroelectrics in [14]) but often have smaller tuning range compared to other solutions. Moreover, it should be noted that scaling acoustic filters towards high frequencies is critical but fraught with challenges [42]. For frequencies above 2.5 GHz, BAW filters are needed but come with significantly higher cost compared to SAW filters which are commonly deployed below 2.5 GHz [43].

Finally, widely-tunable RF filters have been demonstrated using cavity filters, micro-electromechanical systems (MEMS) devices, or EM structures with discrete microwave components [44]–[47]. However, these tunable filters are usually quite bulky and/or costly compared to acoustic or silicon-based solutions and hence are not suitable for many mobile applications.

In [32], we reported a hybrid CMOS-acoustic filtering front-end solution (Fig. 3.1), enabling widely-tunable and compact RF filtering front-ends. Our proposed front-end solution utilizes

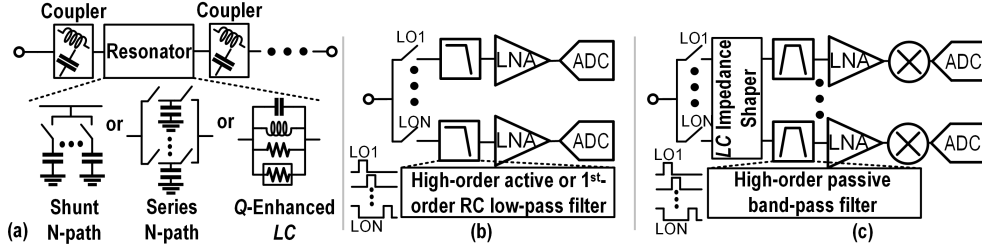


Figure 2.2: Silicon-based tunable RF filtering front-ends based on (a) coupled tunable high- Q resonators, (b) mixer-first direct-conversion architecture, and (c) mixer-first high-IF superheterodyne architecture.

a single fixed-frequency high-order acoustic filter after an N -path switched- LC mixer. This way, OOB interference at close-in offset frequencies is suppressed by the high-order acoustic filter while the front-end operation frequency is defined jointly by the mixer local oscillator (LO) and the acoustic filter – essentially a *mixer-first acoustic-filtering* RF front-end. Also, an all-passive implementation is adopted for high linearity and power handling. A prototype using a CMOS switched- LC passive mixer followed by an off-the-shelf 1.6-GHz SAW filter has been designed and implemented. In measurement, the RF front-end operates across 2.5-to-4.5 GHz achieving 5.5-dB noise figure (NF) and +29.4-dBm input-referred third-order intercept point (IIP3) at $1\times$ bandwidth offset.

This article is an expanded version from [32] and is organized as follows. Section II discusses tunable RF filtering front-end architectures. Section III unveils impedance aliasing in mixer-first front-ends. The proposed mixer-first acoustic-filtering front-end is described in Section IV. Design considerations and implementation details are presented in Section V. Finally, measurement results are discussed in Section VI, and Section VII concludes the paper.

2.2 Tunable RF Filtering Front-End Architectures

Many existing silicon-based tunable RF filtering front-ends may be grouped into two categories: (1) front-ends using tunable coupled high- Q resonators [see Fig. 2.2(a)] and (2) mixer-first low/zero-IF direct-conversion receivers [see Fig. 2.2(b)]. Our proposed mixer-first acoustic-filtering front-end opens a new design space with a *mixer-first high-IF superheterodyne architecture* [see Fig. 2.2(c)].

2.2.1 Filtering Front-Ends Using Tunable Coupled Resonators

High-order RF filters may be synthesized by coupling high- Q LC -resonators [see Fig. 2.2(a)]; hence, one natural way to construct a tunable filter is through tuning the LC -resonators

and their coupling networks. One fundamental challenge associated with this approach is that on-chip passives have poor quality factor Q , resulting in prohibitively high loss. To tackle this challenge, state-of-the-art works adopt either N-path resonators or Q -enhanced LC -resonators.

A Q -enhanced LC -resonator utilizes active transistors connected in a positive feedback to compensate the loss associated with on-chip passives [37], [48], [49]. The resonance frequency is made programmable by using a switched-capacitor bank, but its loss increases with its capacitance tuning range. Hence, large transistors are required to compensate the loss in a widely-tunable filter at the expense of an elevated noise level and degraded linearity.

A linear periodically time-variant (LPTV) N-path resonator up-converts an RC low-pass filtering response in the frequency domain, resulting in a band-pass response centered around an LO defined RF [19], [21]. This way, the N-path resonator center frequency can be tuned across a broad frequency range with a wideband LO. It has been shown that an N-path resonator has an RLC equivalent circuit whose Q factor is proportional to the LO frequency [19]. At low gigahertz frequencies, integrated N-path resonators with high- Q of around 100 have been demonstrated (e.g. [50]). Such a high- Q realized using passive components results in much better noise and linearity performance compared to Q -enhanced tunable LC RF filters. However, due to lossy coupling networks, parasitic effects, and the need of multi-phase square-wave RF clocks, these filters have limited OOB rejection, moderate frequency tuning range, and rarely operate above 2 GHz RF. N-path filters operate beyond 2 GHz have been reported (e.g. [51]) but are limited to a second-order filtering with poor suppression and linearity performance at close-in frequency offsets.

In sum, constructing a tunable filter by directly altering its resonators and coupling networks faces a tight trade-off between its operation frequency range and other filter metrics, e.g. noise, linearity, and stop-band or transition-band suppression. *From a fundamental perspective, this trade-off arises from the fact that RF tuning capability is tangled up with achieving high-order selectivity.*

2.2.2 Mixer-First Direct-Conversion Filtering Front-Ends

In a mixer-first receiver as shown in Fig. 2.2(b), a passive mixer (driven by a set of non-overlapping square-wave periodic RF pulses) frequency translates the impedance of baseband low-pass filters to RF, resulting in a band-pass filtering response at the receiver input [52], [53]. Similar to an N-path filter, the Q -factor of the frequency-translated band-pass filter in a mixer-first receiver gets boosted in this frequency translation process; the resultant Q -factor is proportional to the mixer LO frequency. Because of this high- Q at RF, mixer-first receivers

are considered a promising solution for tunable RF filtering front-ends [38]–[41], [54].

While an N-path-resonator-based band-pass filter and a mixer-first receiver both leverage LPTV operation for high Q , they adopt different methods for creating high-order filtering. The former makes *multiple* high- Q but low-order N-path filters first and then couples them to make a high-order filter (e.g. [20], [36]). In contrast, a mixer-first receiver often needs a *single* set of N-path switches followed by high-order baseband filters. Since a single N-path filter is utilized, complex LO generation circuitry and lossy coupling networks between N-path resonators are avoided, leading to higher operation frequency (e.g. [38]).

Hence, the beauty of a mixer-first approach, when compared to a front-end using tunable coupled resonators, is that *the RF tuning and high-order selectivity are achieved separately where a set of commutated switches performs RF dialing and a bank of high-order baseband filters rejects OOB interference; this breaks the trade-off between RF operation range and filter performance.*

The challenge associated with enhanced-selectivity mixer-first receivers is the design of low-pass high-linearity baseband circuits that provide high-selectivity input impedance [38]–[41], [54]. A high-order filter design at zero or low IF with a baseband bandwidth well below 1 GHz necessitates active-RC-based implementations which often result in limited linearity performance. By creating input-impedance notches using switched capacitor circuits, a zero-IF mixer-first receiver with high-order passive filtering was reported in [55]. However, it has a maximum operation frequency of 2 GHz with a high NF of 10.3 dB. High-order switched-capacitor discrete-time low-pass filters have been reported (e.g. [56]) but they cannot provide input matching at RF. Mixer-first receiver with high-order passive LC filters has been reported recently with RF between 21 and 29 GHz and a 1-GHz instantaneous RF bandwidth [57]. However, for a sub-6-GHz receiver front-end, LC passive filters with a bandwidth order-of-magnitude below 1 GHz are bulky and lossy.

2.2.3 Mixer-First High-IF Superheterodyne Filtering Front-Ends

The filtering front-end in this article opens a new design space for mixer-first receivers. As conceptually shown in Fig. 2.2(c), a passive mixer is followed by a bank of band-pass filters, instead of low-pass filters in traditional mixer-first designs. An LC -based impedance shaper is inserted between the mixer and IF filters and is to ensure minimal conversion loss while to preserve input matching as detailed in Section IV. After each IF filter, a second-stage zero-IF direct-conversion receiving path is utilized before analog-to-digital conversion.

The introduction of an additional mixer to the filtering front-end transforms a traditional low/zero-IF direct-conversion mixer-first receiver to a *high-IF superheterodyne receiver*. *This*

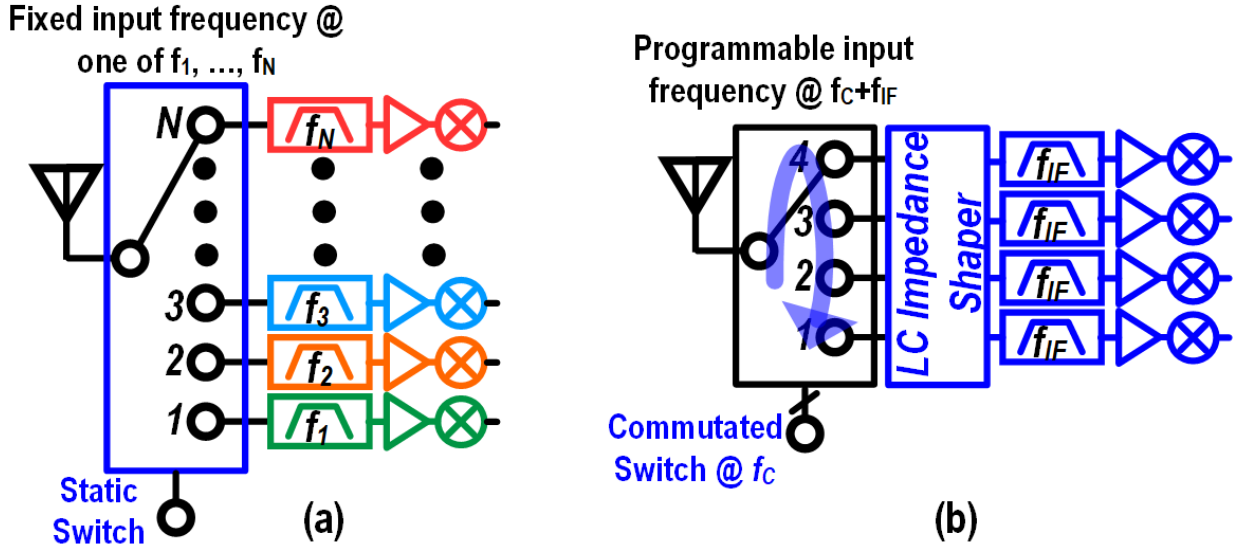


Figure 2.3: Conceptual comparison between (a) a filter-bank-based multi-band front-end design and (b) our proposed superheterodyne mixer-first front-end.

choice of a gigahertz high IF opens the door for compact and low-loss passive IF filters. While gigahertz acoustic IF filters are adopted in this work, integrated passive gigahertz band-pass filters may be utilized for a monolithic realization.

Comparing with traditional superheterodyne receivers [58]–[60], removing the first-stage RF low-noise amplifier (LNA) and having all passive components prior to high-order filtering significantly improve the front-end linearity and dynamic range; this is similar to LNA-less direct-conversion zero-IF or low-IF receivers [61]. Also, having a gigahertz IF significantly alleviate the image problem in a superheterodyne architecture [62].

Finally, it is also instructive to compare our proposed superheterodyne mixer-first front-end with a conventional filter-bank-based front-end design as shown in Fig. 2.3. In a conventional multi-band RF front-end, a bank of acoustic filters with different center frequencies connects to an antenna via a static RF single-pole-multi-throw switch [13]. This approach requires a large number of different filters and has a lack of flexibility to incorporate future frequency bands after deployment in the field. *Our design effectively makes the single-pole-multi-throw RF switch periodically rotate among a bank of identical filters, making the input frequency programmable and jointly defined by the switch rotational or commutation frequency and the filter center frequency.*

2.3 Impedance Aliasing in Mixer-First Superheterodyne Front-Ends

In this section, we unveil the concept of impedance aliasing in mixer-first superheterodyne front-ends. Impedance aliasing is often negligible in a direct-conversion mixer-first receiver but can be significant in a superheterodyne front-end, especially when loaded with high-order acoustic filters.

2.3.1 Mixer-First Superheterodyne Front-Ends

Let us start with a mixer-first high-IF superheterodyne receiver loaded with second-order LC band-pass filters similar to that in [63]. As shown in Fig. 2.4(a), an RF input port with a source resistance R_S is connected to a 4-path passive mixer driven by non-overlapping 25% duty-cycle LOs with frequency f_{LO} . Passive mixer switches have on-resistance of R_{SW} . A parallel LC tank which resonates at the IF f_{IF} connects to each mixer switch is further followed by a load resistance R_L .

This way, a desired signal with frequency $f_S = f_{IF} + f_{LO}$ at RF input port gets down-converted to the LC band-pass filter passband by the passive mixer, while an OOB interference is rejected by the LC filter. Input RF interference at the image and harmonic frequencies $f_{IF} + kf_{LO}$, where k is an integer and $k \neq 1$, also appears at IF after mixing. Due to the high IF, image signal gets suppressed before entering the mixer while input interference at harmonic frequencies experiences an increasingly small conversion gain with a large harmonic index $|k|$. Further suppression may be obtained through image and harmonic rejection architectures [58], [64].

In a mixer-first receiver, its IF impedance is frequency translated to RF due to the transparency property of the passive mixer [53]. The input impedance at RF of a zero/low-IF mixer-first receiver has been derived and modeled by a linear time-invariant (LTI) model in [53]. Using an analysis that is similar to that in [65], we derive an LTI representation of the input impedance at f_S (see Section III-B for more details) for the proposed mixer-first high-IF front-end as shown in Fig. 2.4(b), where

$$R_{sh} = (R_S + R_{SW}) \frac{N\gamma}{1 - N\gamma}, \quad (2.1)$$

$$\gamma = \frac{\text{sinc}^2(\pi/N)}{N}. \quad (2.2)$$

N is the mixer-first front-end number of paths. R_{sh} models the losses due to harmonic

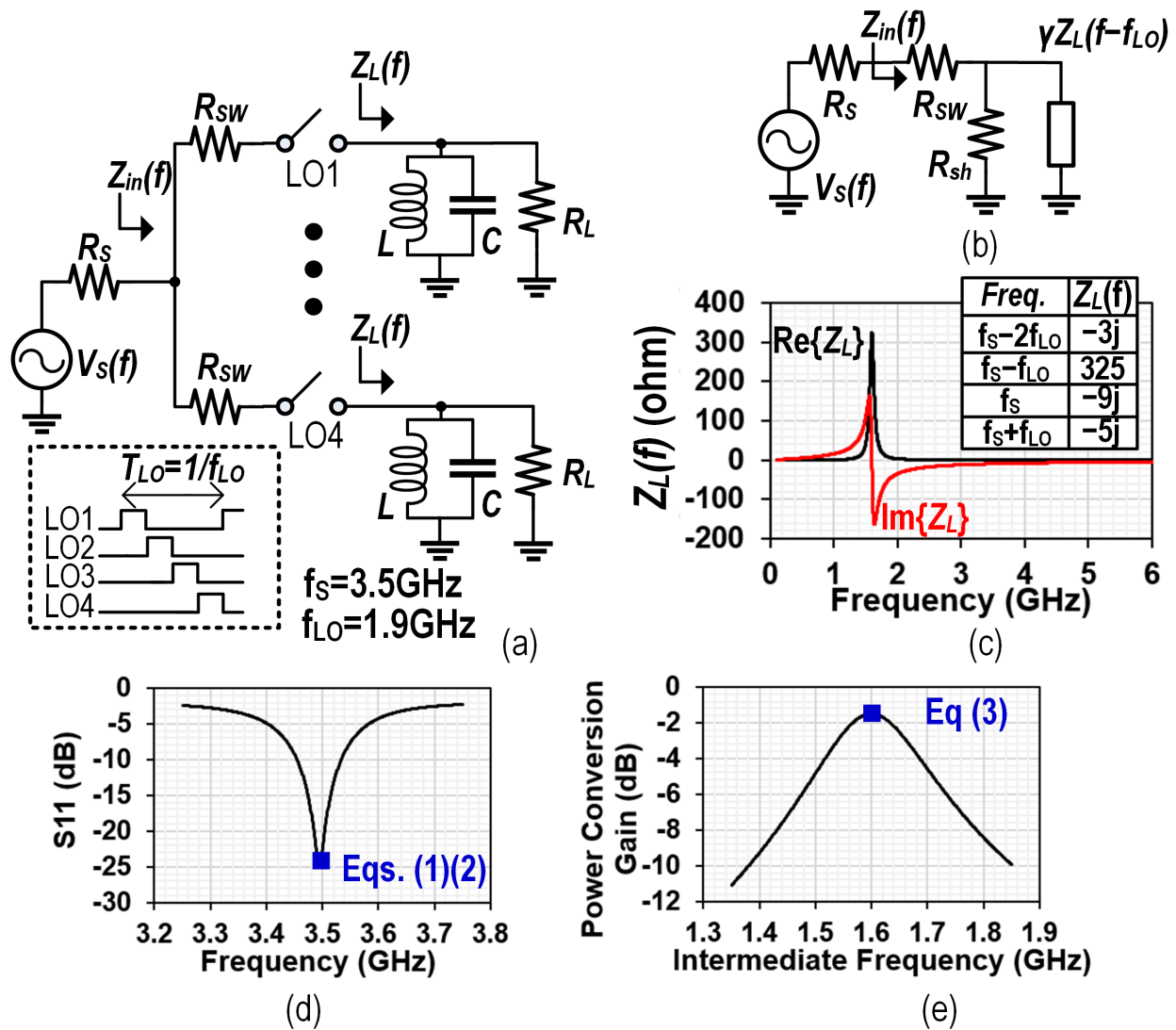


Figure 2.4: Switched-LC mixer-first front-end: (a) schematic; (b) RF LTI equivalent model; (c) second-order LC load impedance with its components at LO harmonic frequencies; (d)(e) simulated front-end input matching and power conversion gain.

re-radiation and γ is the scaling factor for the IF impedance at f_{IF} ; these are the same as those in a zero/low-IF mixer-first receiver [53]. It should be noted that we've assumed $2f_{LO}$ is much larger than the RF 3-dB bandwidth of the mixer load impedance Z_L ; this is equivalent to assuming the LO frequency is much larger than the RC low-pass 3-dB bandwidth in a zero/low-IF mixer-first N-path front-end [18], [21], [53].

In (2.1) and (2.2), we've assumed that $2f_{IF}$ is not integer multiples of f_{LO} . This avoids impedance aliasing which we will discuss shortly in Section III-B.

Based on the the LTI model in Fig. 2.4(b), (2.1), and (2.2), the power conversion gain which is the ratio between the power delivered to the load at $f_S - f_{LO}$ and the maximum available power from the source can be calculated as:

$$G = \frac{4}{(1 + \frac{R_S + R_{SW}}{R_{sh} || \gamma R_L})^2} \cdot \frac{R_S}{\gamma R_L}. \quad (2.3)$$

A design example is used to validate our model with $R_S=50 \Omega$, $L=3.125$ nH, $C=3.166$ pF, $R_L=325 \Omega$, $f_{IF}=1.6$ GHz, and $f_{LO}=1.9$ GHz. We've used ideal switches with $R_{SW}=5 \Omega$. R_L is significantly larger than a typical LNA input resistance and is obtained using an impedance transformer as detailed in Section V. The simulated and calculated input impedance at $f_S=3.50$ GHz are 56.4Ω and 56.5Ω , respectively, showing an excellent match. The small difference arises from finite clock rising and falling time in our simulation. The simulated front-end input matching and power conversion loss are shown in Fig. 2.4(d) and (e), respectively; the LTI equivalent model in Fig. 2.4(b) and (2.3) accurately predicts the 1.5-dB loss due to R_{sh} re-radiation, mixer switches, and input power reflection.

Our LTI model is identical to that of a zero/low-IF direct-conversion mixer-first receiver in [52]. This can be intuitively understood by observing the mixer load impedance Z_L as shown in Fig. 2.4(c). In both architectures, the mixer load impedance only has significant impedance around IF or a single peak around IF, while the impedances at harmonic frequencies are negligible. For instance, the impedance at $f_S=3.5$ GHz, $f_S+f_{LO}=5.4$ GHz and $f_S-2f_{LO}=-0.3$ GHz are $-9j \Omega$, $-5j \Omega$, and $-3j \Omega$, respectively; these are much smaller compared to the in-band $325\text{-}\Omega$ resistance and hence have negligible impact on the circuit.

Next, let us replace the second-order LC bandpass filters in Fig. 2.4 with high-order SAW band-pass filters as shown in Fig. 2.5. To emulate a SAW filter (e.g. the one that we used in our prototype [66]), we construct an eight-resonator ladder-type bandpass filters with a simple lossless Butterworth-Van Dyke (BVD) resonator model as shown in Fig. 2.5(b) [12], [14], [67]. A Ladder-type bandpass filter that consists of 5-to-20 series and parallel SAW or BAW resonators are used in many mobile applications, while a three-element BVD resonator circuit is commonly used to approximately describe the behavior of a SAW or BAW resonator

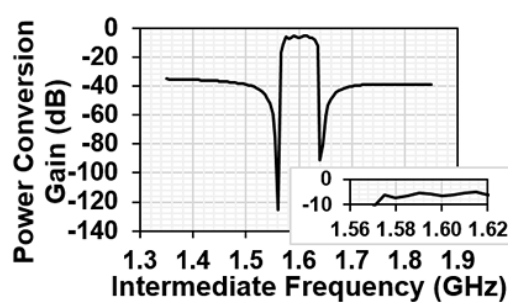
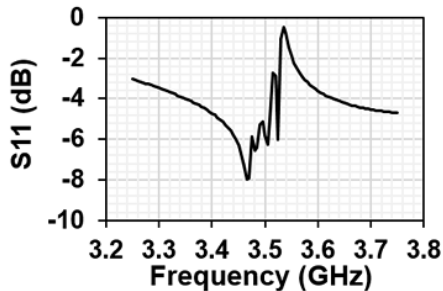
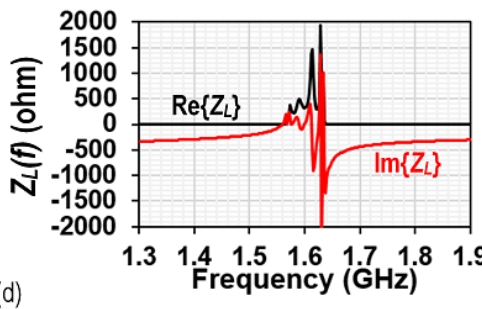
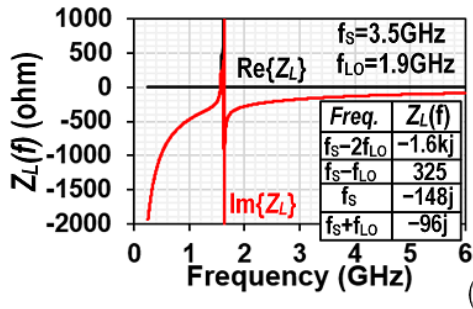
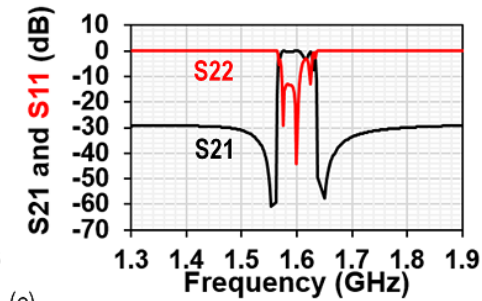
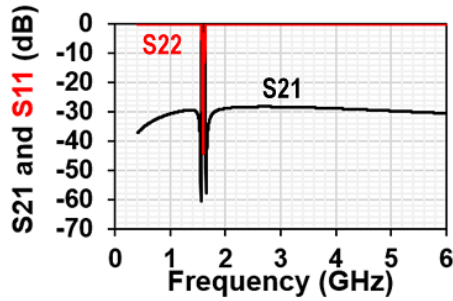
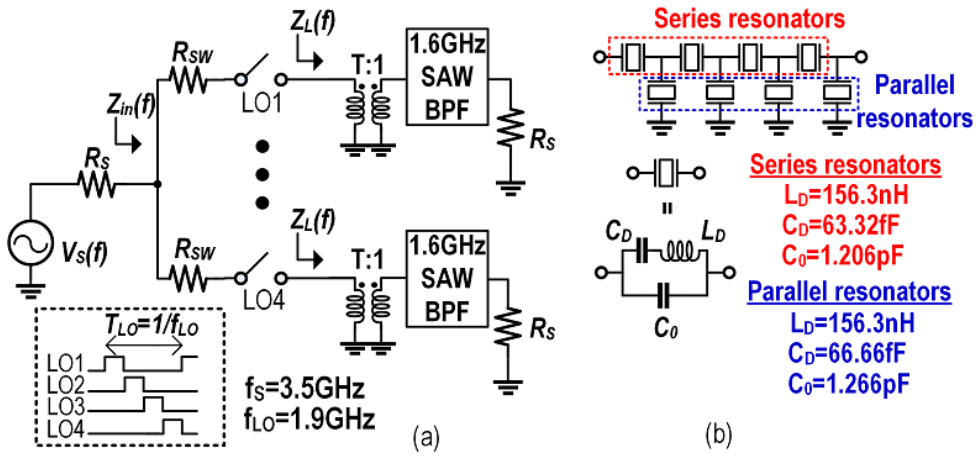


Figure 2.5: Switched-SAW-filter mixer-first front-end: (a) schematic; (b) ladder-type bandpass filter load; (c) simulated filter stand-alone input matching and insertion loss; (d) high-order acoustic filter load impedance with its components at LO harmonic frequencies; (e)(f) simulated front-end input matching and power conversion gain.

[12]. The static capacitance C_0 , dynamic inductance L_D and capacitance C_D of our series and parallel resonators are given in Fig. 2.5(b). The filter has a simulated in-band frequency range of 1.57 to 1.6 GHz with nearly 0-dB insertion loss and < -10 -dB input reflection as shown in Fig. 2.5(c). The simulated input impedance of the filter when loaded with a 50-ohm resistor and preceded by a $T=\sqrt{\frac{325}{50}}$:1 ideal transformer is given in Fig. 2.5(d). The transformer is used to boost the in-band resistance from 50 ohm to 325 ohm which is the load resistance we used in switched-second-order-LC front-end simulation (Section III-A, Fig. 2.4).

Using these ladder-type bandpass filters, the simulated mixer-first front-end input reflection and power conversion gain are depicted in Fig. 2.5(e) and (f), respectively. A sharp performance degradation is observed with -5.8 -dB input reflection at 3.5 GHz RF and -6.4 -dB power conversion gain at 1.6 GHz IF.

Let us look at the load impedance shown in Fig. 2.5(d); despite identical load resistance of 325 ohm at the 1.6-GHz IF as in Fig. 2.4(c), the BVD-model-based acoustic filter has significant impedance components at harmonic frequencies. As in Fig. 2.5(d), the load impedance at harmonic frequencies $f_S + f_{LO}=5.4$ GHz, $f_S=3.5$ GHz, and $f_S - 2f_{LO}=-0.3$ GHz are $-96j \Omega$, $-148j \Omega$, and $1616j \Omega$, respectively, order-of-magnitude larger than those of a second-order LC filter.

While the topology and implementation of acoustic filters for mobile applications vary in practice, it is not unfair to assume that high impedance exists across a wide OOB frequency range for most acoustic filters. Acoustic filters are designed to optimize in-band performance and OOB rejection [12]. However, OOB rejection does not always needs low impedance – a high impedance is also reflective and hence provides OOB suppression. More importantly, the variation in silicon-acoustic interconnects makes it nearly impossible for acoustic filters to maintain a low OOB impedance across a multi-GHz-wide frequency range. In Fig. 2.6, we plot the impedance (with the $\sqrt{\frac{325}{50}}$:1 ideal transformer) of the ideal SAW acoustic filter in Fig. 2.5(b) with that* of the off-the-shelf SAW filter used in our prototype [66]. We’ve assumed a tunable 2.5-to-4.5-GHz input frequency f_S and a fixed $f_{IF} = f_S - f_{LO}$ at 1.6 GHz; this results in OOB LO harmonic at $f_S + f_{LO}$ covering a multi-GHz-wide range from 3.4 to 7.4 GHz. In both cases, the in-band impedance is around $325+0j \Omega$ and significant impedance is seen at OOB LO harmonic frequencies. Also, the SAW filter impedance with a silicon-acoustic interconnect modeled by a 3-mm matched lossless transmission line is plotted Fig. 2.6. As expected, this interconnect has negligible impact at in-band frequencies, but alters the impedance noticeably at OOB frequencies.

*The off-the-shelf SAW filter impedance is obtained from its S-parameters provided by the vendor.

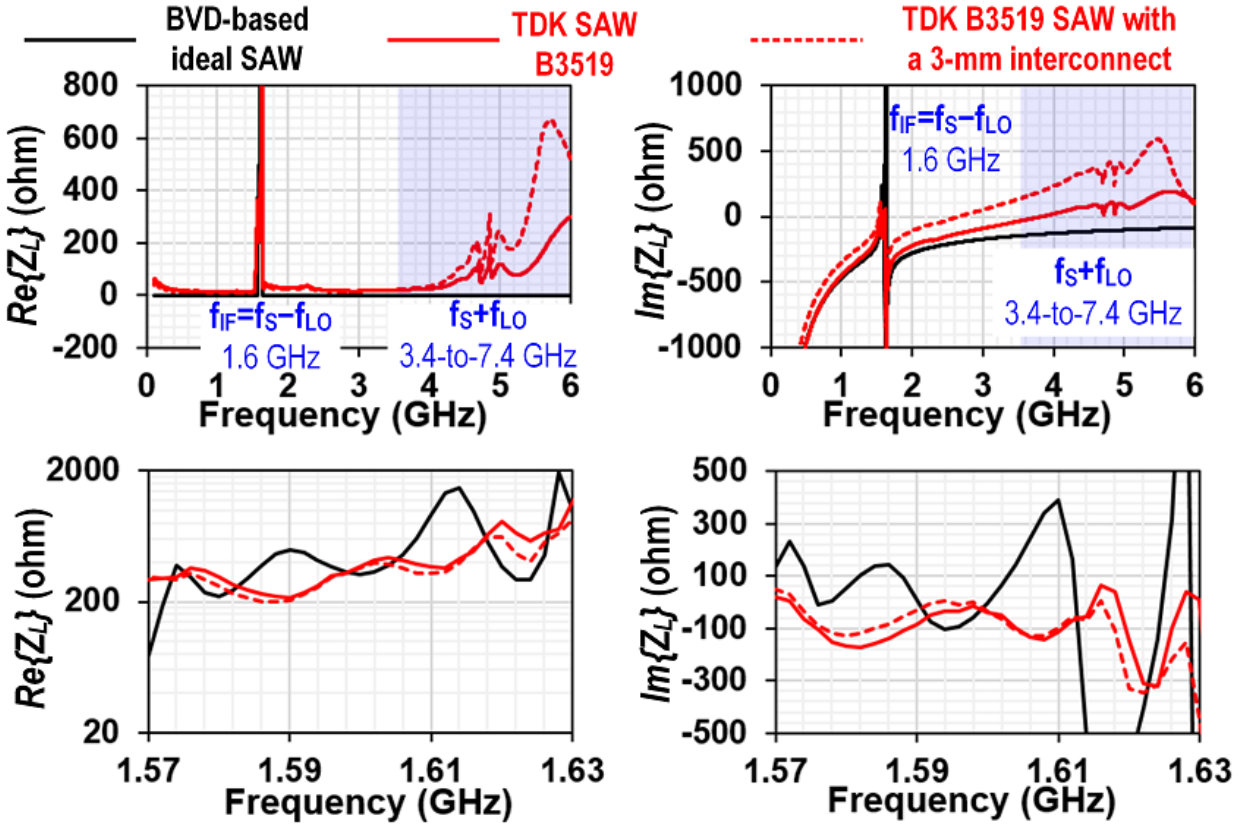


Figure 2.6: SAW filter input impedance (including the $\sqrt{\frac{325}{50}}:1$ ideal transformer in Fig. 2.5): BVD-model-based ideal SAW in Fig. 2.5(b), an off-the-shelf SAW [66] with and without silicon-acoustic interconnects. While the topology and implementation of acoustic filters for mobile applications vary in practice, it is reasonable to assume that low impedance is not guaranteed across a wide OOB frequency range for most acoustic filters.

2.3.2 Impedance Aliasing in Mixer-First Front-Ends

We attribute the sharp performance degradation of a switched-SAW front-end in Section III-A to a phenomenon that we call *Impedance Aliasing*.

As illustrated conceptually in Fig. 2.7(a), an incoming desired signal at $f_S = f_{IF} + f_{LO}$ is split into harmonic currents at frequencies $\dots, f_S - 2f_{LO}, f_S - f_{LO}, f_S, f_S + f_{LO}, \dots$ at IF after mixing with narrow-pulse LOs[†]. These harmonic IF currents flow into Z_L at LO harmonic frequencies, creating harmonic IF voltages. Through passive mixer IF-to-RF conversion, IF voltage V_{IF} components at the LO harmonic frequencies jointly set the RF input impedance. Through this process, the IF load impedance Z_L components at all these frequencies are translated to RF, not just the one at $f_{IF} = f_S - f_{LO}$.

It should be noted that due to the passive-mixer transparency property, the mixer RF-to-IF and IF-to-RF conversions depicted in Fig. 2.7(a) happen simultaneously and eventually converge to a steady state (see [53], [65] and our quantitative analysis in the appendix). However, we find that the artificial separation of the RF-to-IF and IF-to-RF conversions helps with providing an intuitive understanding.

We name the process illustrated in Fig. 2.7 impedance aliasing since IF load Z_L components at the LO harmonic frequencies become indistinguishable, or aliases of one another, when translated to RF input via the mixing operations.

In a direct-conversion zero/low-IF mixer-first receiver, while a desired input signal is also split into LO harmonic frequencies, only the IF current at $f_S - f_{LO}$ is in-band, seeing significant impedance [see Fig. 2.7(b)]. Hence, the impedance aliasing in a direct-conversion mixer-first front-end is often negligible.

On the other hand, in a superheterodyne mixer-first receiver with a high IF, multiple IF current components at different LO harmonic frequencies can experience significant load impedance when compared to $Z_L(f_{IF})$. As depicted in Fig. 2.7(b), two IF currents align with Z_L at $\pm f_{IF}$ assuming second-order *RLC* loads when $f_S = 2f_{LO} = 2f_{IF}$. With high-order acoustic filters, Z_L components at more frequencies could be aliased to RF.

If IF loads have significant impedance only around $\pm f_{IF}$ but not other LO harmonic frequencies, e.g. second-order *RLC* or acoustic filters with our proposed impedance shaper in Section IV, it is possible to avoid impedance aliasing in a superheterodyne mixer-first front-end by choosing f_{LO} such that $|f_S - kf_{LO}|$ does not fall near f_{IF} , where $k > 1$ is an integer. Letting $|f_S - kf_{LO}| = f_{IF}$, we find f_{LO} that results in impedance aliasing as $f_{LO} = 2f_{IF}/(k - 1)$. Hence, provided that $2f_{IF}$ is not integer multiples of f_{LO} as we've assumed in Section III-A, impedance aliasing in this case can be ignored.

[†]We've only considered the desired signal positive frequency component as the negative frequency component is correlated with its positive frequency counterpart and has a similar behavior.

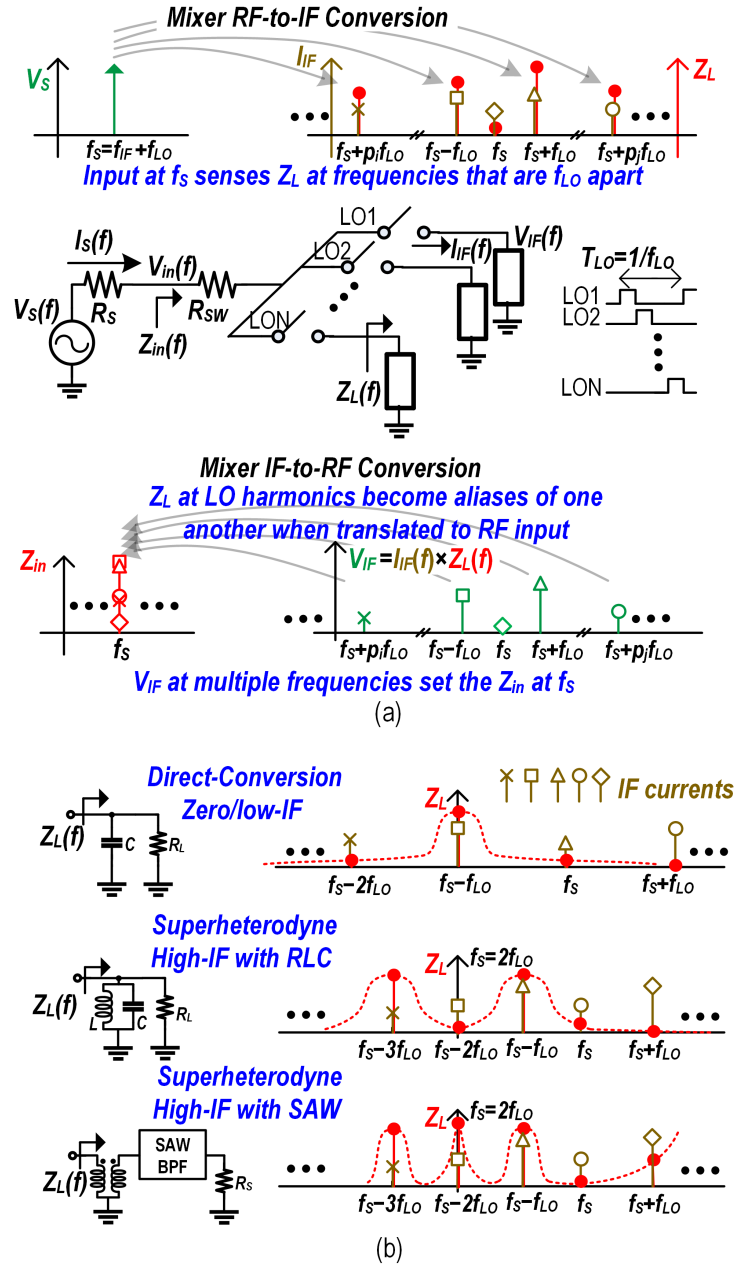


Figure 2.7: Impedance aliasing in a passive-mixer-first front-end. (a) A desired signal is split into IF currents, flowing into Z_L at the LO harmonic frequencies and creating IF harmonic voltages. These IF voltages jointly determine the RF voltage, aliasing Z_L components at harmonic frequencies to RF. (b) Mixer-first IF harmonic currents and Z_L in a direct-conversion and superheterodyne high-IF front-ends: while impedance aliasing is often negligible in a direct-conversion mixer-first receiver as only the IF current at $f_s - f_{LO}$ sees significant impedance, it can be significant in a superheterodyne front-end, especially when loaded with high-order acoustic filters as multiple IF currents experience significant impedance.

The constraint of $2f_{IF}$ being not integer multiples of f_{LO} leads to dead bands in a superheterodyne front-end. However, by choosing RF range judiciously, a reasonably wide tuning range could be obtained. Given an $f_{IF}=1.6$ GHz, LO frequencies corresponding to dead bands are $f_{LO}=0.8$ GHz, 1.6 GHz, and 3.2 GHz, where we've ignored even-order LO harmonics assuming a differential implementation. By limiting LO frequency between 0.9 GHz to 2.9 GHz, there will be only one dead band around 1.6 GHz f_{LO} . As discussed in Section V-C, the dead band occupies less than 15% of the tuning range in our prototype.

Next, we study impedance aliasing quantitatively by deriving an analytical solution of the input impedance Z_{in} at RF. Based on our analytical results, we propose an equivalent LTI model that captures impedance aliasing.

In contrast to existing analyses (e.g. [18], [53], [65]) that aim at low/zero-IF front-end with low-pass-filter loads, our analysis assumes a load impedance $Z_L(f)$ which could have significant impedance components at LO harmonic frequencies. These impedance components at LO harmonic frequencies result in impedance aliasing. As derived in the appendix, the RF input impedance Z_{in} can be expressed as

$$Z_{in} = R_{SW} + \frac{R_{SW} + R_S}{K - 1}, \quad (2.4)$$

where K is a complex coefficient that is given as

$$K^{-1} = N \sum_{i=0}^M [a_{1-p_i} Z_L(f + (p_i - 1)f_{LO}) Y_{p_i}(f - f_{LO})]. \quad (2.5)$$

In (2.5), N is the mixer-first front-end number of paths, $a_n = \frac{\text{sinc}(\frac{n\pi}{N})}{N} e^{-j\frac{n\pi}{N}}$ and admittance $Y_{p_i}(f)$ is the solution of a matrix equation given below:

$$[N\mathbf{Z}_M + (R_S + R_{SW})\mathbf{I}]\mathbf{y} = \mathbf{a}, \quad (2.6)$$

where \mathbf{I} is an identity matrix of size $M+1$, $\mathbf{y} = [Y_0(f), Y_1(f), \dots, Y_M(f)]^T$, $\mathbf{a} = [a_{-1}, a_0, \dots, a_{M-1}]^T$, and the i -th row and j -th column element of \mathbf{Z}_M is given as:

$$Z_{m,i,j} = Z_L(f + jf_{LO}) \sum_{k=-\infty}^{\infty} \text{sinc}\left(\frac{(Nk - 1 + i)\pi}{N}\right) \text{sinc}\left(\frac{(Nk - 1 + j)\pi}{N}\right) / N^2$$

If the load impedance $Z_L(f)$ only has significant impedance at one frequency $f_{IF} = f_S - f_{LO}$ and $2f_{IF}$ is not integer multiples of f_{LO} , (2.4) reduces to the LTI model given in Fig. 2.4(b),

(2.1), and (2.2).

It is instructive to examine the front-end behavior when there are two controlled impedance peaks in $Z_L(f)$: one at $f_{IF} = f_S - f_{LO}$, one at another harmonics $f_S + pf_{LO}$ where p is an integer and $p \neq -1$. In this case, (2.4) can be solved analytically as (A.15) in the appendix. (A.15) can be approximated as:

$$Z_{in,2peaks} \approx R_{SW} + R_{sh,-1} |(\gamma_{-1} Z_{IF,-1}) + R_{sh,p} |(\gamma_p Z_{IF,p}). \quad (2.7)$$

Based on (2.7), we propose an LTI equivalent circuit as depicted in Fig. 2.8(a). The input impedance can be viewed as mixer switch on-resistance in series with two parallel networks, modeling impedance aliasing of the these two impedance components; each parallel network consists of a re-radiation resistance and a scaled IF impedance at the corresponding harmonic frequency. Also, input signal power is split between the two parallel networks. Therefore, to minimize the mixing loss, we should suppress the impedance at the harmonic frequency $f_S + pf_{LO}$.

Our proposed LTI model in Fig. 2.8(a) is tested against simulation using the 4-path mixer-first front-end in Fig. 2.5 with an artificial load impedance Z_L made of ideal resistors, inductors, capacitors, and controlled sources. The simulated Z_L is depicted in Fig. 2.8(b). The Z_L at $f_S - f_{LO}=1.6$ GHz is fixed at 325 Ω , while the impedance at the other peak $f_S + f_{LO}=5.4$ GHz is swept. The resultant RF input resistance at 3.5 GHz is plotted in Fig. 2.8 (c) using both simulation and calculation based on our LTI model. Only the real part of the resistance is shown as the imaginary part is zero based on our theory and is negligible compared to the real part in the simulation. A reasonable match is seen between simulation and our LTI model. The error is partially due to ignored interactions among different harmonic responses when we reach (2.7).

When the impedance at the harmonic frequency R_{L2} is small, the input impedance is around 50 Ω and can be predicted by the simple LTI model in Fig. 2.4(b), (2.1), and (2.2). As R_{L2} increases, the RF input impedance starts to change and eventually saturates. This saturated resistance behavior proves the existence of additional re-radiation shunting resistance at harmonic frequencies as shown in our LTI model in Fig. 2.8(a).

We further extend our proposed LTI model in Fig. 2.8(a) to include a multiple shunting networks in series to capture a generic Z_L with an arbitrary frequency response. Using the same simulation setup in Fig. 2.5 and removing the impedance step-up transformers, we have simulated and calculated, using both the full equation in (2.4) and the LTI model, the RF impedance at $f_{IF} + f_{LO}$ with different LO frequencies as shown in Fig. 2.9. In our LTI model

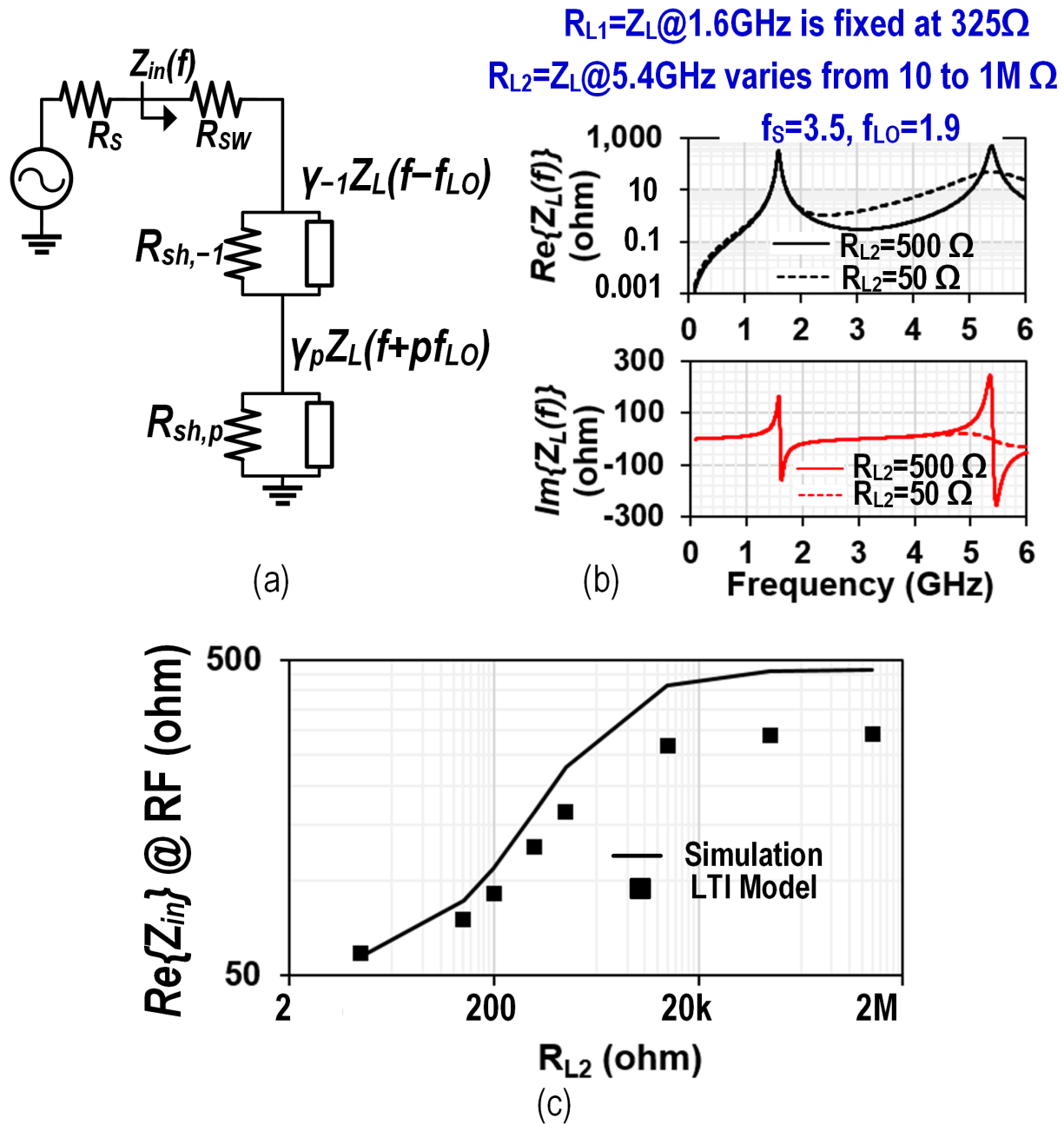


Figure 2.8: Investigation of mixer-first front-end loaded with an artificial two-peak load impedance Z_L : (a) LTI model capturing two peaks with one at IF $f_S - f_{LO}$ and the other at harmonic frequency $f_S + pf_{LO}$; (b) simulated load impedance Z_L which is made of ideal resistors, inductors, capacitors, and controlled sources; and (c) simulated and calculated input impedance at RF across different Z_L resistance at $f_S + f_{LO} = 5.4$ GHz.

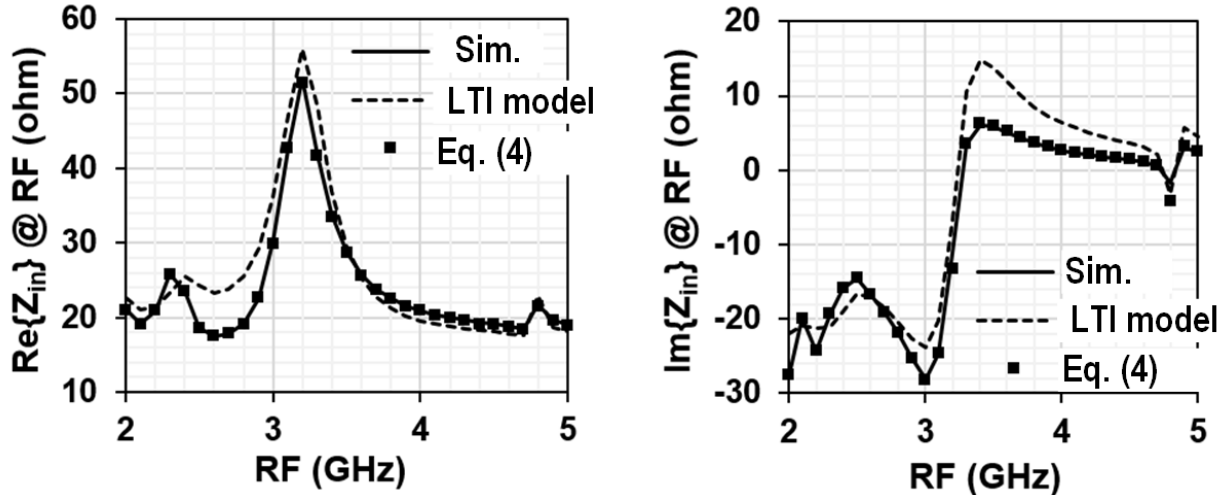


Figure 2.9: Simulated and calculated switched-SAW-filter mixer-first front-end input impedance.

and numerical results, 21 harmonics, $M=10$ in (2.6), are considered. A reasonable match is seen among simulation, our LTI model, and the numerical results based on (2.4).

2.4 Mixer-First Acoustic-Filtering Front-End Using an Impedance Shaper

2.4.1 Impedance Shaper Suppressing IF Filter OOB Impedances at Harmonic Frequencies

Through impedance aliasing discussed in Section III, mixer-first front-end load impedance components at harmonic frequencies can significantly deteriorate the front-end performance. In this work, we propose to insert an LC network, essentially an *Impedance Shaper*, right after mixer switches to suppress input impedance at the harmonic frequencies. The impedance shaper here is realized by second-order parallel LC tanks with resonance frequency at f_{IF} as in Fig. 2.10. At OOB low and high frequencies, impedance shaper inductor and capacitor provide low impedance to ground, respectively.

Unlike the acoustic filter that suppresses close-in interference, the LC tanks provide low impedance at harmonic frequencies that are gigahertz away and hence can be realized with low-order on-chip implementations.

In the proposed switched- LC mixer-first acoustic-filtering front-end (see Fig. 2.10), all circuit parameters are identical to those in Fig. 2.5 except that an LC impedance shaper is added with $L=1.56$ nH and $C=6.33$ pF. The simulated load impedance Z_L real and imaginary

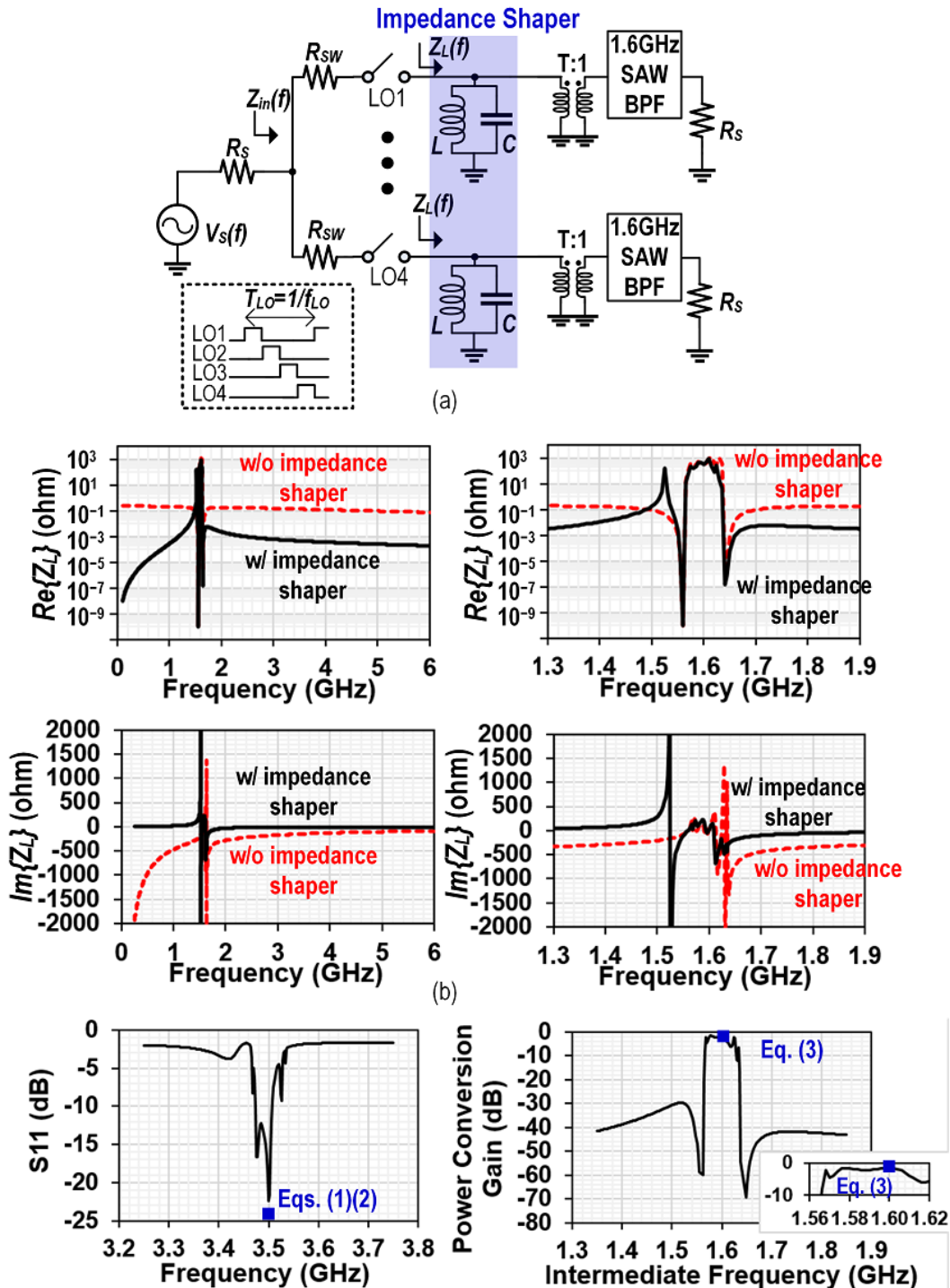


Figure 2.10: Introducing LC -tanks to suppress acoustic filter OOB impedance: (a) receiver diagram; (b) simulated load impedance before (dashed lines) and after (solid lines) suppression; and (c) simulated front-end input matching and power conversion gain.

parts with and without impedance shaper is depicted in Fig. 2.10(b). The load impedance absolute values at harmonic frequencies $f_s + f_{LO}=5.4$ GHz, $f_s=3.5$ GHz, and $f_s - 2f_{LO}=-0.3$ GHz are dropped by orders of magnitude from $96j \Omega$, $148j \Omega$, and $1616j \Omega$, to $5j \Omega$, $8j \Omega$, and $3j \Omega$, respectively.

As expected, the introduction of the LC impedance shaper results in resorted front-end performance in terms of input matching and power conversion gain as shown in Fig. 2.10(c). In fact, after introducing the impedance shaper, the front-end in-band behavior becomes nearly identical to the case when the loads are single-peak second-order LC bandpass filters in Fig. 2.4 with -24 dB S11 and 1.5 dB power conversion loss at 3.5 GHz RF. Let us look at the zoomed-in load impedance in Fig. 2.10(b). The LC impedance shaper does not change Z_L at in-band frequencies since the LC is tuned to the in-band center frequency and has a relatively small loaded quality factor. The impedance shaper does alter Z_L at close-in OOB frequencies. This only affects front-end input impedance or S11 at adjacent-band frequencies but the front-end in-band matching and filtering conversion gain are preserved as shown in Fig. 2.10(c).

A natural question arises is that how to choose the value for the impedance shaper inductance or capacitance given a resonance frequency at f_{IF} . A small inductance increases the load LC tank (without N-path switches and source resistance R_S) quality factor $Q_T = R_T/\omega_0 L$ where $R_T = R_S \cdot T^2$ and $\omega_0 = \omega_{IF}$ is the LC resonance frequency. A high Q_T has large suppression on load impedances at harmonic frequencies, leading to better matching and lower mixing loss. However, a high Q_T reduces transformer balun power transfer efficiency, resulting in large power loss inside the transformer. The design trade-off and considerations are detailed in Section V-B.

2.4.2 Single-Acoustic-Filter N-Path Filtering

One issue remains for the mixer-first acoustic-filtering front-end shown in Fig. 2.10 – it needs four acoustic filters and four IF receivers, which could lead to large form factor, high cost, and high power consumption.

In this work, we use a recombination network at IF to reduced the required number of acoustic filters and IF receivers as shown in Fig. 2.11. First, two transformer baluns reduce the number of paths from four to two as in Fig. 2.11(a). Then, a CLC lumped transmission-line equivalent circuit with a characteristic impedance of R_L and a phase shift of 90° at f_{IF} is introduced at the bottom path in Fig. 2.11(a). Finally, we combine the two paths using another transformer balun at the output side as in Fig. 2.11(b). With this IF recombination network, our front-end becomes similar to a Hartley image-rejection receiver [68].

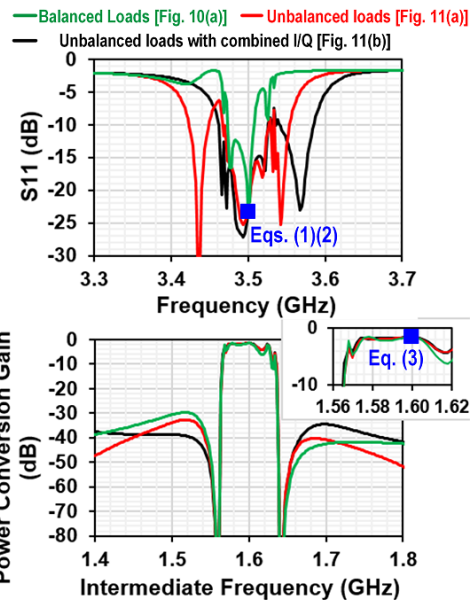
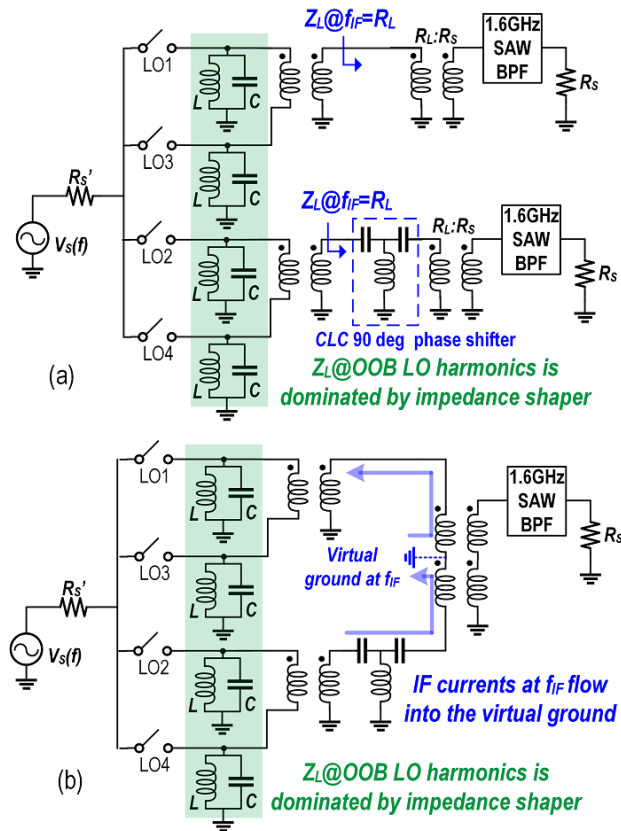


Figure 2.11: Single-acoustic-filter N-path filtering using all-passive recombination network at IF: (a) merging four paths into two with transformer baluns and a CLC 90-deg phase shifter, (b) combining in-phase and quadrature paths, and (c) simulated input matching and power conversion gain.

The mixer-first front-end in Fig. 2.11(a) has unbalanced loads compared to that in Fig. 2.10(a). Nevertheless, we expect the unbalance loads here will have negligible impact on the input matching and power conversion gain for the in-band signal. As illustrated in Fig. 2.11(a), mixer IF currents at f_{IF} on both the in-phase (I) and quadrature (Q) paths see identical load impedance R_L assuming the CLC circuit is tuned at f_{IF} ; regarding IF currents at OOB LO harmonic frequencies, they are mostly sunk by the LC impedance shaper which has identical impedance among all paths. Simulated input matching and power conversion gain in Fig. 2.11(c) validate our expectation. Also, as shown in Fig. 2.11(c), signals that are at close-in OOB or adjacent band frequencies are subject to the unbalanced loading, altering the input matching response. However, filtering response in the power conversion gain largely remains the same. Finally, for far-out OOB signals, the load impedance is dominated by the LC impedance shaper, minimizing the effect of unbalanced loads.

When the two paths in Fig. 2.11(a) are combined as in Fig. 2.11(b), the differential in-band signals at f_{IF} creates a virtual ground, isolating the two paths. Hence, the in-band S11 and power conversion gain remain unchanged; see the simulation results in Fig. 2.11(c). Adjacent band signals are subject to I-Q paths interaction which manifests itself in the simulated input matching in Fig. 2.11(c); however, filtering response is preserved. Similarly, for far-out OOB signals, the load impedance is dominated by the LC impedance shaper, shielding the front-end from the effect of combined I-Q paths. As shown in Fig. 2.11(c), while the filtering conversion gain exhibits a superior frequency selectivity, this selectivity does not directly translated to the input side. Therefore, high-linearity mixer switch design is critical for the front-end linearity performance as discussed in Section V-C.

The amplitude and phase mismatches between the two paths in our front-end limits the amount of image rejection. The CLC lumped transmission-line equivalent circuit is intrinsically narrowband. Nevertheless, thanks to a high IF of 1.6 GHz, a 65 MHz bandwidth (the bandwidth of our prototype front-end) corresponds to a small 4% fractional bandwidth. In our simulation, the CLC circuit has up to $\pm 4^\circ$ and 1 dB phase and amplitude variation across the entire bandwidth. These mismatches result in around 30 dB worst-case image suppression as shown in [62]. In addition, thanks to a gigahertz IF, image bands are well separated from the desired signal bands. In our prototype, image bands are below 1 GHz with 2.5-to-4.2-GHz RF. This wide frequency separation eases the design of a possible on-chip or off-chip high-pass pre-selection filter.

2.5 Design Considerations and Implementation

In this section, we address design considerations that optimize the front-end performance in the presence of implementation losses from impedance transformation and transformer baluns. Also, the circuit implementation details of our prototype front-end in a 65-nm CMOS process are discussed.

2.5.1 Trade-Off Between Number of Paths and Impedance Transformation Ratio

Similar to a conventional low/zero-IF mixer-first receiver [52], a large number of paths and a small switch on-resistance R_{SW} results in low power conversion loss in the proposed mixer-first acoustic-filtering front-end. Using (2.1)(2.2)(2.3), we plot power conversion loss versus R_{SW} for different path numbers in Fig. 2.12(a). As expected, an 8- or 16-path design offers lower loss compared to a 4-path design. However, more paths require larger IF load impedance for a given RF source impedance [52]. While large load impedance can be conveniently obtained in a low/zero-IF mixer-first receiver, it is challenging to have a large load impedance in our proposed mixer-first acoustic-filtering front-end.

Off-the-shelf acoustic filters are often designed to have 50- Ω source resistance R_S . However, this source resistance gets reduced significantly by the scaling factor γ in (2.2) when it is translated from IF to RF. This necessitates step-up impedance transformation for input matching to 50- Ω at RF.

The required overall impedance set-up ratio can be obtained by setting the input impedance at RF in Fig. 2.5(a) to be 50- Ω , i.e. $R_{SW} + R_{sh} || \gamma R_L = R_S$. We have ignored the IF recombination network here for simplicity and $R_L = T^2 R_S$ is the front-end IF in-band load impedance after impedance transformation. Based on these, the impedance set-up transformation ratio T^2 is given as

$$T^2 = \frac{1}{\gamma} \cdot \frac{R_S - R_{SW}}{R_S} \cdot \frac{R_{sh}}{R_{sh} - R_S + R_{SW}}. \quad (2.8)$$

Using (2.8), we plot T versus R_{SW} for 4, 8, and 16 paths in Fig. 2.12(b). Compared to a 4-path design, an 8- or 16-path design has about 0.5-dB lower loss with a 5- Ω R_{SW} but it comes at the expense of a significantly higher impedance transformation ratio. Generally speaking, the higher the impedance transformation ratio, the more lossy the transformer is [69]. In addition, an 8- or 16-path design would require a more complex IF recombination network and LO path design, adding more loss and complexity to the system. Finally, a larger number of paths leads to higher LO path power consumption and more switch parasitics at

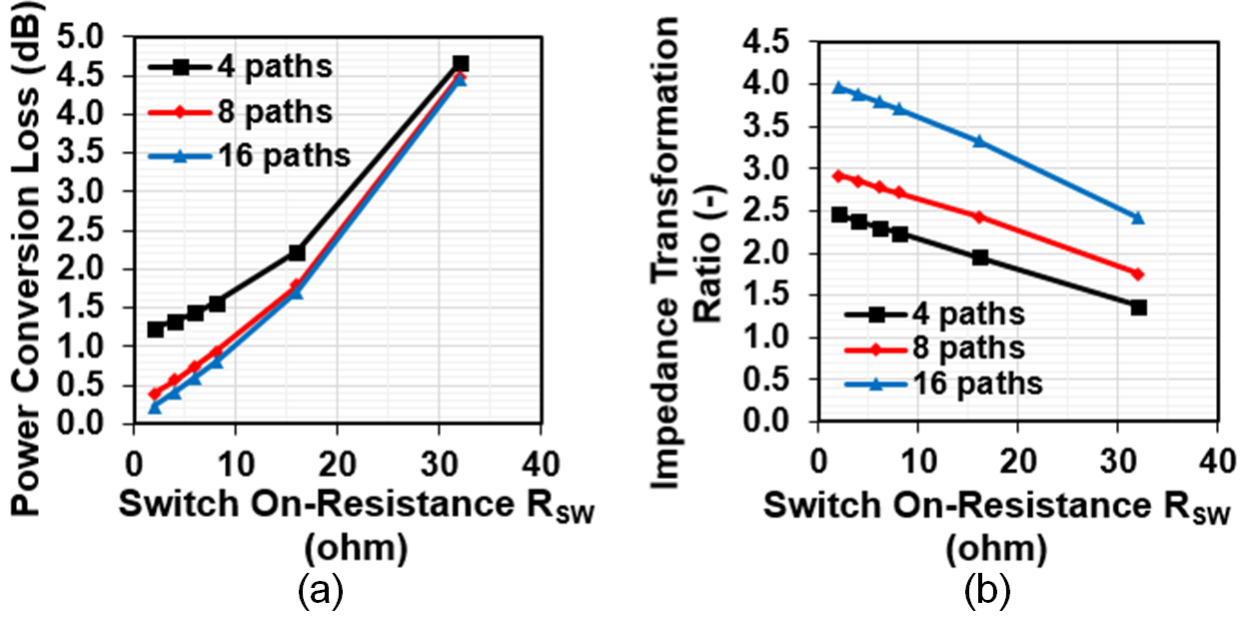


Figure 2.12: Mixer-first acoustic-filtering front-end (a) power conversion loss and (b) IF impedance transformation ratio versus switch-on resistance with different path numbers using (2.1)(2.2)(2.3)(2.8).

the RF input [70]. In our prototype implementation, a 4-path design is chosen with $R_{SW}=5 \Omega$.

2.5.2 Optimizing LC-Tank Q-Factor for Low Loss

As discussed in Section III-C, we introduce an LC impedance shaper to suppress IF filter input impedance at harmonic frequencies for input matching and low mixing loss. A large LC tank quality factor Q_T better suppresses the harmonic impedances, resulting in low loss. However, in the presence of a limited on-chip inductor quality factor Q_{ind} , a large Q_T could increase the power dissipated in the lossy inductor. Therefore, there exists a design trade-off associated with Q_T .

A narrow-band model of the front-end IF load at f_{IF} is depicted in Fig. 2.13(a) where we've ignored the capacitor loss and assumed tightly coupled transformer balun with negligible capacitive coupling. The inductor loss is modeled by a series resistance R_{ind} . R_L is the IF filter in-band resistance after impedance transformation. After converting R_{ind} into a parallel resistance $R_{indp} = (1 + Q_{ind}^2)R_{ind} \approx Q_{ind}^2 R_{ind} = Q_{ind}\omega_{IF}L$, we can calculate the power transfer efficiency at the IF load as

$$\eta = \frac{P_{load}}{P_{in}} = \frac{R_{indp} || R_L}{R_L} \approx 1 - \frac{Q_T}{Q_{ind}}, \quad (2.9)$$

where we've assumed $Q_T \approx \frac{R_L}{\omega_{IF}L}$.

From (3.13), we can see that a small $Q_T \ll Q_{ind}$ is needed for low inductor loss. Assuming $Q_{ind}=10$ and 50, we plot the front-end power conversion gain versus Q_T in Fig. 2.13(b) with $f_{LO}=0.9$ GHz. While mixing loss reduces with a large Q_T , the inductor loss increases. When $Q_{ind}=10$, the optimal Q_T is around 3 with 3.1-dB total loss. If a higher $Q_{ind}=50$ is available, the optimal Q_T becomes about 5 with 2.2-dB total loss. Finally, a high Q_{ind} not only offers a low overall front-end loss but also reduces the inductor size with a large Q_T as $L \approx \frac{R_L}{\omega_{IF}Q_T}$.

2.5.3 Circuit Implementation

We have designed a prototype mixer-first front-end in a 65-nm CMOS process (see Fig. 2.14)[‡]. A differential architecture is utilized to reduce LO clock leakage and harmonic responses around clock even harmonics similar to many mixer-first receivers and N-path filters [19], [36], [38], [41]. A wideband 1:1 off-the-shelf transformer is served as a balun at the RF input for single-ended to differential conversion. Also, the differential implementation reduces the source impedance seen by the mixer-first front-end, relaxing the impedance step-up transformation requirement as discussed in Section IV-A.

Mixer switches are designed to have an on-resistance of 5 Ω for shortening LO pulse rising and falling time and for a balance between front-end power conversion loss and LO path DC power consumption. An on-chip divide-by-2 circuitry is used to generate the 25% duty-cycle clocks driving the mixer switches. Mixer switches are realized using deep-N-well transistors, allowing us to use bootstrapping resistors at their bulk nodes [72]. The biasing voltages at the mixer switch drain and source nodes are designed to avoid false switching [72]. Let us consider the LO high and low voltages to be V_H and V_L , respectively. When the switch is on, the maximum allowable input voltage is $V_{IN,max} = V_H - V_{TH}$, where V_{TH} is the transistor threshold voltage; otherwise, the switched is falsely turned off as gate-source voltage is less than V_{TH} . Similarly, when the switch is off, the minimum allowable input voltage is $V_{IN,min} = V_L - V_{TH}$ to prevent false on. Given $V_H=1.2$ V, $V_L=0$ V, and $V_{TH}=0.4$ V, the input signal biasing voltage and amplitude can be calculated as $\frac{1}{2}(V_{IN,max} + V_{IN,min}) = 0.2$ V and $\frac{1}{2}(V_{IN,max} - V_{IN,min}) = 0.6$ V. In practice, we use a slightly higher biasing voltage of 0.25 V as the 25%-duty-cycled mixer switch spends more time in the off-state. This false-switching-tolerant design comes at the expense of degrading switch reliability as voltage between two transistor terminals can exceed V_{DD} . However, the natural of ac voltage reduces the impact as long as the voltage is no larger than $2V_{DD}$, and similar designs are not uncommon, e.g.

[‡]While there is some similarity to a 2-path double-balanced passive mixer driven by 50% duty-cycle LOs (e.g. [71]), a 2-path mixer itself cannot provide input matching with a small mixer switch on-resistance and suffer from excessive power loss when loaded with an IF bandpass filter.

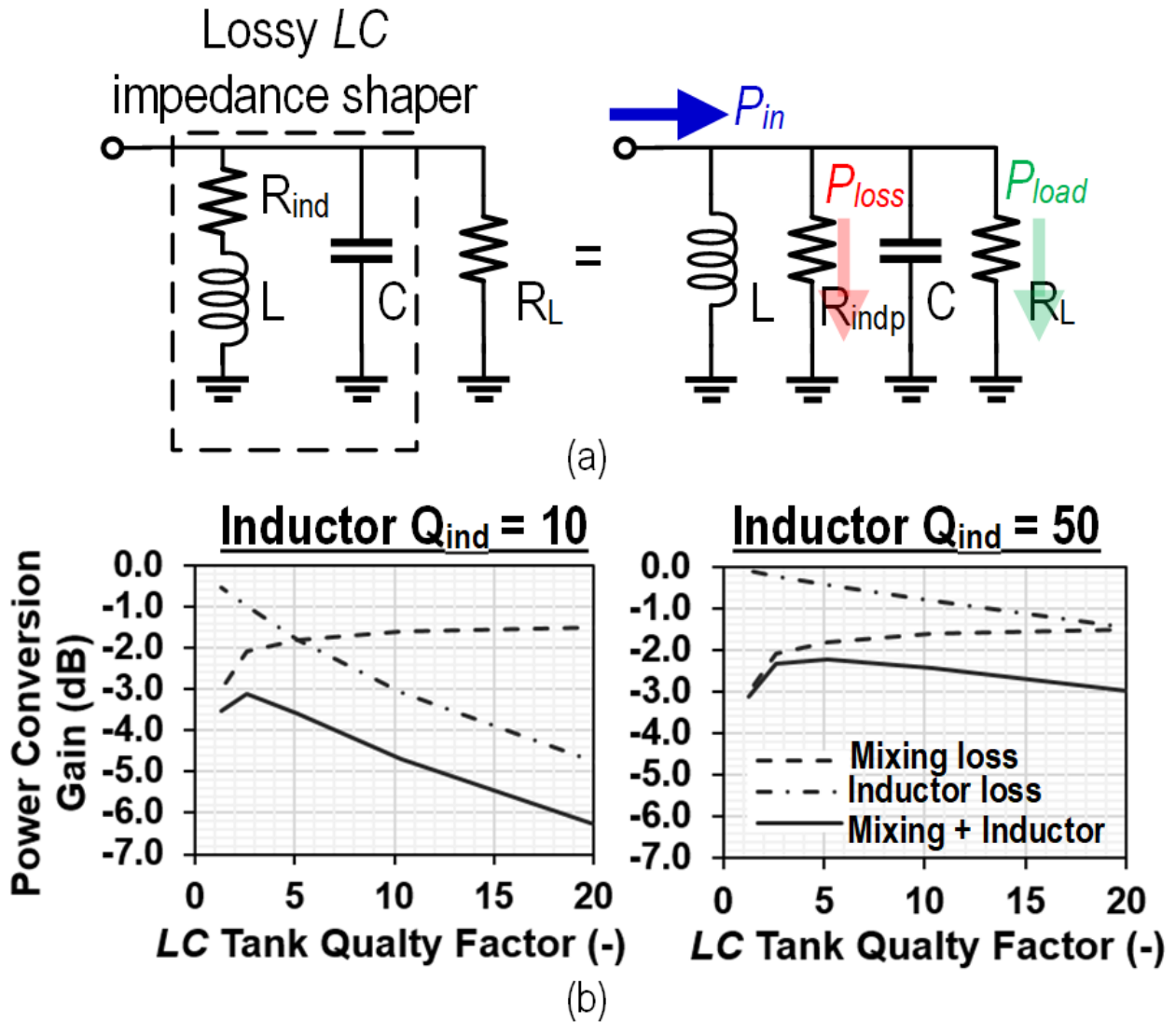


Figure 2.13: Design consideration with a lossy LC impedance shaper: (a) simplified IF load narrow-band circuit model and (b) total front-end power conversion gain with both mixing and inductor losses.

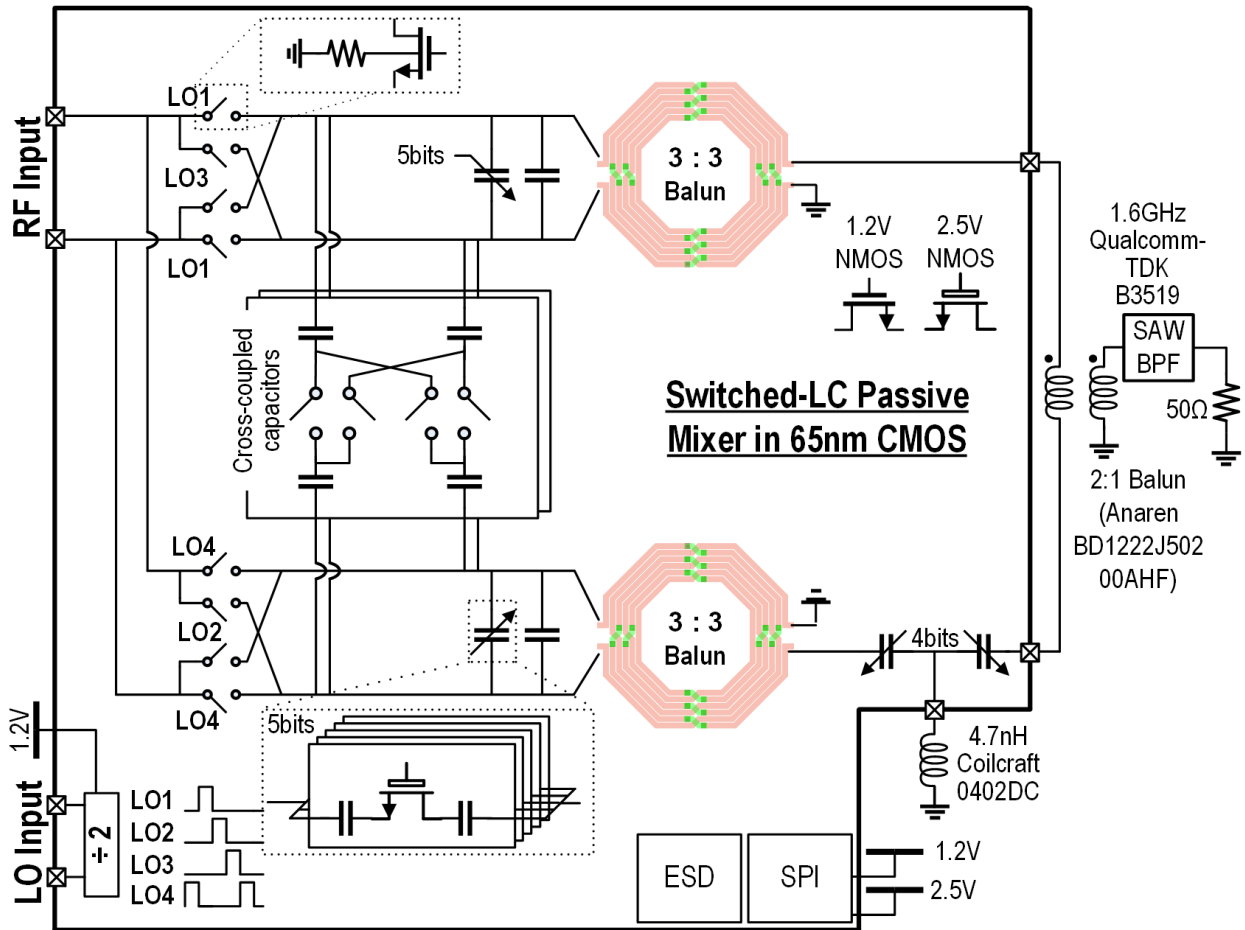


Figure 2.14: Schematic of our prototype mixer-first front-end in 65-nm CMOS with a 1.6-GHz SAW bandpass filter.

[50], [72], [73].

The on-chip impedance shaper is realized via a 5-bit switched-capacitor bank and a 3:3 coplanar transformer balun at each in-phase and quadrature branch. The transformer has simulated balanced inductance of 5 nH, a coupling coefficient of 0.83, and a quality factor Q_{ind} of 13.2. A *CLC* circuitry is employed in the recombination network to provide a 90° phase shift; the inductor is an off-chip 4.7-nH high-Q ceramic inductor, and the capacitor is realized by a 4-bit on-chip switched-capacitor bank. All switched capacitor banks use thick-oxide transistors for high power handling capability. At the differential output of the mixer-first front-end, an off-chip 2:1 transformer balun provided differential to single-ended conversion to interface with a 50-Ω 1.6-GHz SAW bandpass filter [66]. After impedance transformation from transformer baluns, the *LC* impedance shaper has a tank quality factor Q_T of around 2.5. Given $Q_{ind}=13.2$, we expect 1-dB power loss from on-chip transformer baluns based on (3.13).

As shown in Fig. 2.14, cross-coupled capacitors, similar to those in [74], are inserted between the I and Q paths. Leveraging the inherent 90° phase shift between the I and Q paths, these capacitors allow us to access a wider range of input impedance, compensating some VSWR variation from the antenna interface.

Regarding frequency planning, we choose a high IF of 1.6 GHz for relaxed image rejection requirements. This is because that the image and desired bands are separated by $2f_{IF}$, hence a high IF allows one to suppress image response via RF filtering. Using an even higher IF would make the mixer-filter assembly more challenging and lossy. The lowest RF is chosen to be 2.5 GHz. Further lowering this results in excessive power loss given an *LC* impedance shaper tank Q of 2.5. The highest RF operation frequency is limited by the LO circuitry. In post-layout simulation, we find our true-single-phase-clock-based LO circuitry stops working when operating beyond 3 GHz, corresponding to a 4.6 GHz RF. As discussed in Section III-B, there is one dead band with $f_{LO}=1.6$ GHz. Its bandwidth is determined by the *LC* impedance shaper quality factor. Given a quality factor of 2.5, the dead band has a bandwidth of 0.3 GHz around 3.2 GHz RF, assuming the harmonic current is outside of the impedance shaper 3-dB bandwidth.

2.6 Experimental Results

The proposed switched-LC mixer has been fabricated in a 65-nm CMOS process. This chip is packaged and mounted on an FR4 printed-circuit board followed by the transformer balun and 1.6-GHz SAW filter mentioned in Section IV-C. Annotated chip and front-end photographs are shown in Fig. 2.15. Since an all-passive implementation has been adopted for the mixer,

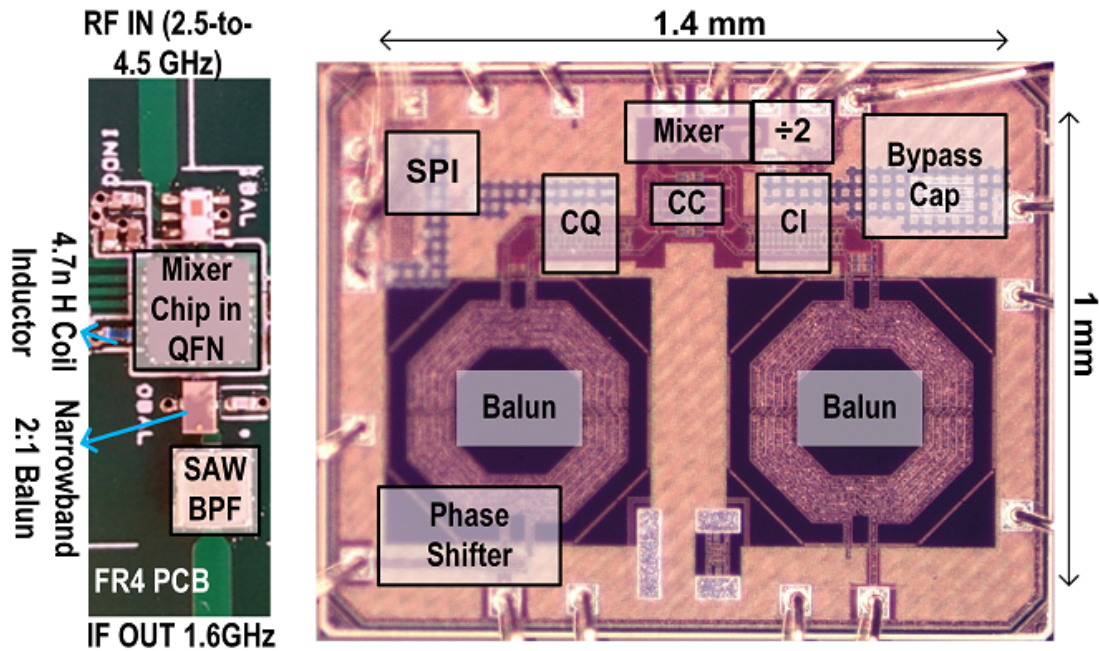


Figure 2.15: Annotated photographs of the switched- LC mixer chip in 65-nm CMOS and the mixer-first acoustic-filtering RF front-end.

the signal path draws zero DC power. The LO-path divider has a DC power of 12-to-26 mW when f_{LO} is swept from 0.9 GHz to 2.9 GHz (corresponding to a 2.5-to-4.5 RF range).

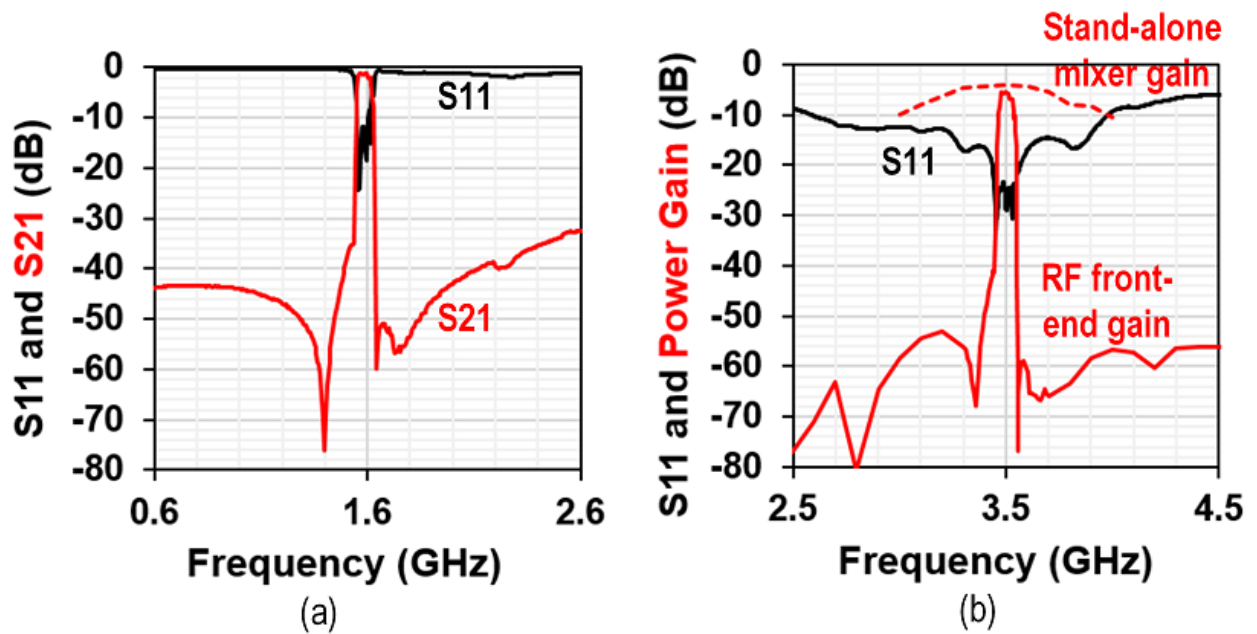


Figure 2.16: Measurement results of (a) the 1.6-GHz SAW filter S-parameters and (b) the mixer-first acoustic-filtering front-end input matching and power conversion gain.

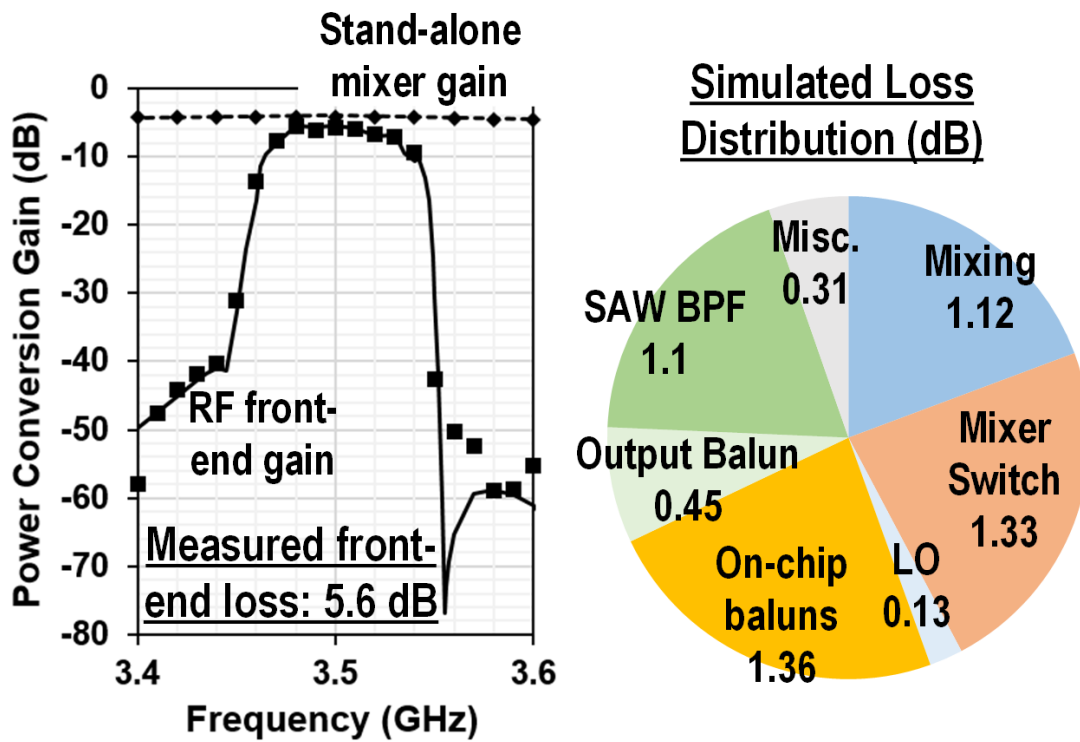


Figure 2.17: Measured (lines) and simulated (markers) mixer-first acoustic-filtering front-end power conversion gain and a simulated loss distribution pie chart.

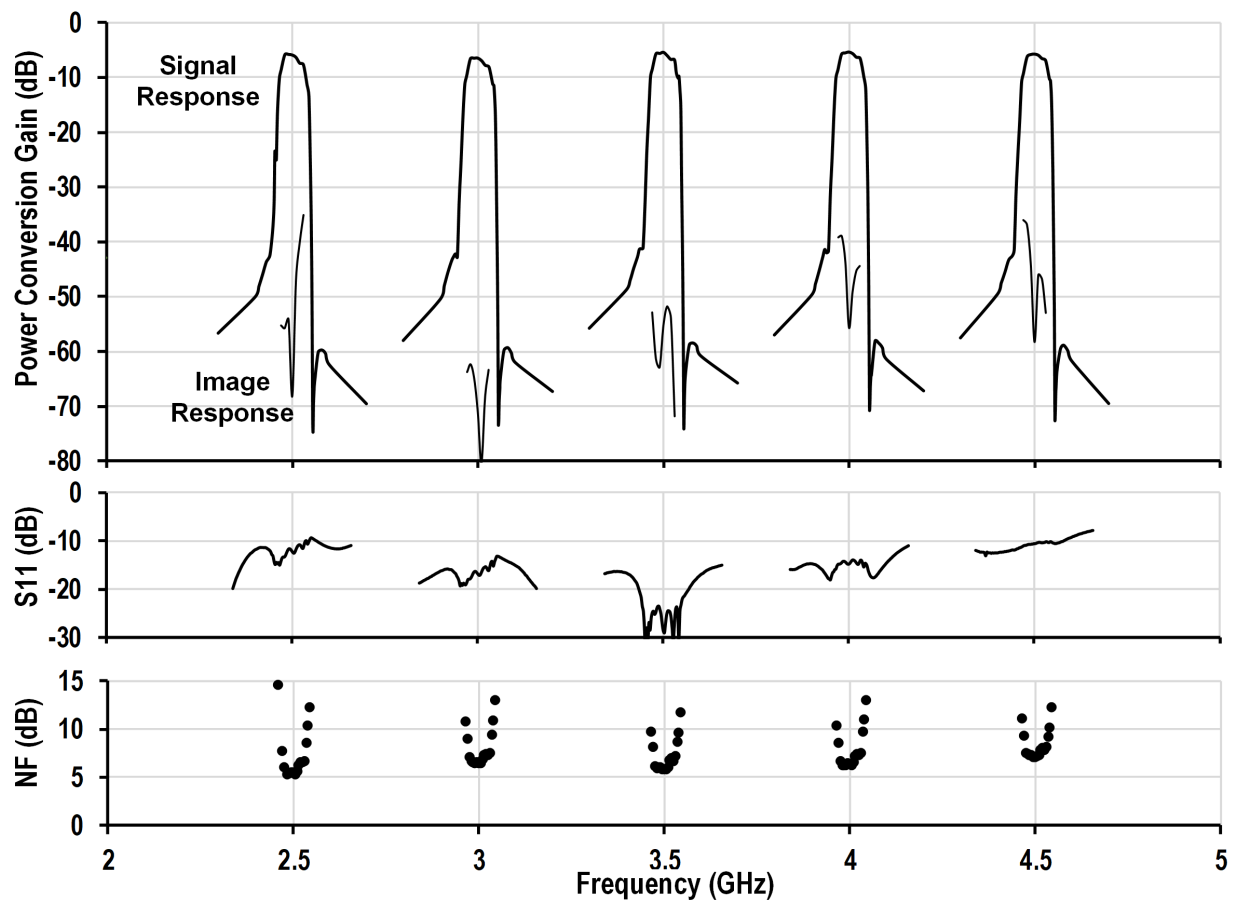


Figure 2.18: Measured mixer-first acoustic-filtering front-end power conversion gain, input matching, and SSB NF across input frequencies.

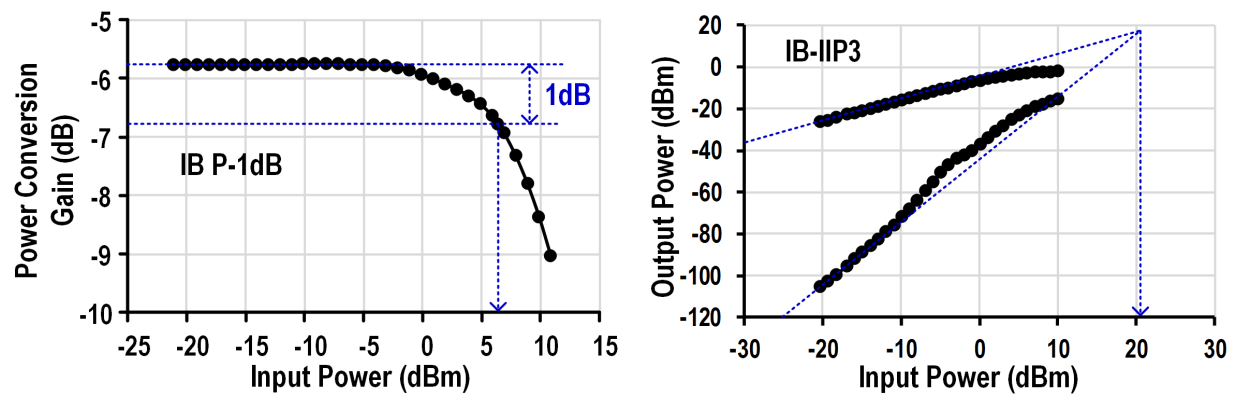


Figure 2.19: Measured mixer-first acoustic-filtering front-end in-band linearity performance when RF input is tuned at 3.5 GHz.

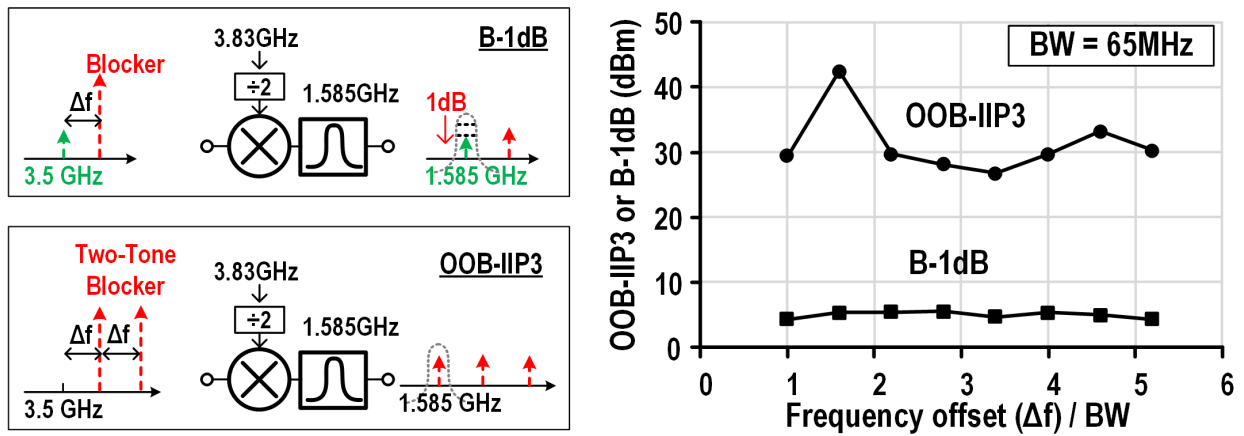


Figure 2.20: Measured mixer-first acoustic-filtering front-end OOB linearity performance when RF input is tuned at 3.5 GHz and diagrams of our measurement setups.

Table 2.1: Measurement summary and comparison with state-of-the-art works.

	JSSC 2019 [7]	JSSC 2019 [5]	JSSC 2018 [8]	JSSC 2020 [10]	JSSC 2020 [11]	JSSC 2018 [53]	JSSC 2016 [33]	This work
Topology	Q-Enhanced Bandpass Filter	High-Order N-Path Filter	Low-IF Mixer-First Receiver with Complex Pole Pair	Low-IF Mixer-First Receiver with Enhanced RF Selectivity	Low-IF Mixer-First Receiver with 3 rd -order TIA	Filter-by-Aliasing-based Receiver	SAW-Less Super-Heterodyne Receiver	Superheterodyne High-IF Mixer-First Acoustic Filtering
RF Range (GHz)	4.1 to 7.9	0.8 to 1.1	0.2 to 8.0	0.2 to 2	0.5 to 2	0.1 to 1	0.5 to 2.5	2.5 to 4.5
NF (dB)	7.6 to 15.7	5 to 8.6	3 to 4 (2.5-4.5 GHz RF)	4.3 to 7.6	5.5	6.5 to 8.5	2.1 to 2.6	5.5 to 7.1
3-dB RF BW (MHz)	120 to 1500 @ 6 GHz RF	30 to 50	20	18	260	2.5 to 40	6.5 to 20	65
IB-IIP3 (dBm)	N.R.	+25	0 to +5 (21 dB Rx gain)	0 to +5 (13 dB Rx gain)	-15 (34 dB Rx gain)	+8 (23 dB Rx gain)	N.R.	+20.3
OOB Rejection at 1.5xRF BW Offset (dB)	20	17	15	20	40	50	15	50
OOB-IIP3 at 1xRF BW Offset (dBm)	+10 to +15	+24	+5	+16	+16	+20	+14 ($\Delta f > 10 \times \text{RF BW}$)	+29.4
B-1dB at 1xRF BW Offset (dBm)	0 to +5	+9	+12 ($\Delta f = 8 \times \text{BW}$)	-3 to +5	-4.4	+3	N.R.	+4.3
Power (mW)	112 to 125	80 to 97	131 to 191 (2.5-4.5 GHz RF)	146.6 to 179	26 to 37	75 to 99	22 to 40	12 to 26
Silicon Technology	130 nm SiGe BiCMOS	65 nm CMOS	45 nm CMOS SOI	28 nm CMOS	28 nm CMOS	65 nm CMOS	28 nm CMOS	65 nm CMOS
Silicon Chip Area (mm²)	0.371	2.3	0.8	0.48	0.16	2.3	0.52	1.4

N.R. – not reported

The measured SAW filter S-parameters together with the RF front-end input matching and power conversion gain when $f_{LO}=1.9$ GHz are plotted in Fig. 2.16(a) and (b), respectively. The SAW filter has a measured center frequency at 1.6 GHz with an RF bandwidth of 65 MHz and insertion loss of 1.1 dB. The measured SAW filter stop-band rejection is about 30-to-40 dB. After the frequency translation of the switched-LC mixer using $f_{LO}=1.9$ GHz, the RF is centered at 3.5 GHz with measured power conversion gain of -5.6 dB. Similar to other works (e.g. [19], [36], [38], [41]), we have de-embedded the loss of input RF balun for our RF front-end. The acoustic-filtering front-end preserves the SAW filter 65-MHz signal bandwidth but offers more stop-band rejection due to the on-chip LC impedance shaper. The measured power conversion gain of a standalone mixer testing board is plotted in Fig. 2.16(b) as well, showing the bandpass response of the LC impedance shaper.

Let us take a closer look at the mixer-first acoustic-filtering front-end power conversion gain. A zoomed-in version of front-end power conversion gain from both measurement and simulation is plotted in Fig. 2.17. A good match between measurement and simulation has been observed. Based on this, a simulated loss distribution pie chart is also given in Fig. 2.17. The simulated 5.7-dB total loss consists of 1.1 dB from harmonic re-radiation, 1.3 dB from mixer switch on-resistance and its parasitic capacitance, 1.4 dB from on-chip transformer baluns, around 1.6 dB from off-chip balun and SAW filter, and finally 0.3 dB from board-level interconnects. Using (2.1)(2.2)(2.3), the calculated loss from both harmonic re-radiation (R_{sh}) and mixer switch on-resistance is 1.4 dB; this is about 1-dB lower compared to our simulation. The excess loss comes from the switches parasitic capacitance [70]. Using (3.13), the expected on-chip transformer balun loss is 1 dB which is also less than the loss in simulation. The 0.4-dB additional loss is due to the finite magnetic coupling which (3.13) does not take into account.

The power conversion gain, input matching, and NF of our mixer-first acoustic-filtering front-end are measured across 2.5-to-4.5 RF with f_{LO} from 0.9 GHz to 2.9 GHz as shown in Fig. 2.18. Power loss of 5.4-to-6.4 dB, S11 of < -10 dB, and SSB NF of 5.5-to-7.1 dB are seen across the entire RF range. While the LPTV operation results in noise folding, the same behavior also causes re-radiation, increasing power loss [70], [75]. Our measured NF is close to power loss as the noise and loss in an all-passive N-path filter reported in [76]. The SAW filter wide bandwidth of 65 MHz is preserved. The power conversion gain for image-band signals at $f_{IF} - f_{LO}$ is also measured and plotted in Fig. 2.18, achieving >50 -dB image rejection. Besides the Hartley image-rejection architecture of our IF recombination network, a large frequency separation of 1.8-to-5.2 GHz between the desired and image bands allows additional image filtering at RF input.

The measured mixer-first acoustic-filtering front-end linearity results are shown in Figs. 2.19

and 2.20. The measured in-band 1-dB compression point (P-1dB) is +6.4 dBm, while the in-band IIP3 is +20.3 dBm. At OOB ($1\times$ RF bandwidth offset Δf), blocker-induced 1-dB compression point (B-1dB) of +4.3 dBm and IIP3 of +29.4 dBm are measured. The B-1dB at $1\times$ RF bandwidth offset is degraded from in-band P-1dB due to high input impedance at close-in frequency offsets. This is because while the mixer load impedance at LO harmonic frequencies is suppressed by the *LC* impedance shaper, the impedance of close-in offsets is not. Interestingly, the IIP3 is higher at OOB than that from an in-band test. It is likely due to partial non-linear distortion cancellation [9]. Unlike in the compression and in-band IIP3 tests, the test tones in an OOB IIP3 measurement are separated by tens or hundreds of megahertz. This relatively large frequency separation makes it possible for the fundamental and inter-modulation tones experience different phase shifts in the front-end, resulting in the partial cancellation of inter-modulation tones [9].

Table I compares this work with state-of-the-art reconfigurable band-pass filters [36], [37] and receivers [38], [40], [41], [60], [77]. When compared with the high-order N-path filter in [36], this work exhibits 33 dB more OOB rejection, operates at $3\times$ higher RF with $5\times$ reducing in average power, while having comparable NF, IB and OOB linearity. Comparing with the zero-IF mixer-first receiver in [38], this work has 2-to-3 dB higher NF at 2.5-to-4.5 GHz but exhibits 29 dB more OOB rejection at $1.5\times$ BW offset frequency and 24 dB higher OOB IIP3 at $1\times$ BW while achieving significant power reduction. Comparing with superheterodyne receivers (e.g. [60]), this work exhibits order-of-magnitude higher linearity, thanks to the elimination of active devices before filtering.

2.7 Conclusion

We have demonstrated a mixer-first acoustic-filtering superheterodyne RF front-end. It represents a new reconfigurable RF receiver architecture that fuses the strength of a widely-tunable passive-mixer-first front-end with the advantage of high-selectivity acoustic filters, while compensating for their respective bottlenecks, namely tight trade-off among noise, linearity, and bandwidth in CMOS and the lack of frequency tuning in acoustics. Our analytical results and a corresponding LTI model have unveiled impedance aliasing in a mixer-first front-end – that is, mixer-first load impedances at harmonic frequencies are all translated to input at RF and leads to degraded input matching and excess power losses. To address this challenge, we have proposed an *LC*-based impedance shaper to suppress the load impedance at harmonic frequencies for low loss and input matching. An all-passive recombination network has been proposed to reduce the number of acoustic filters and for image rejection. Detailed practical design considerations in the presence of implementation losses from impedance

transformation and transformer baluns have been addressed. In measurement, a prototype front-end achieves superior performance in terms of OOB interference suppression and linearity at close-in frequency offset above 2.5 GHz while having comparable noise figure. Topics for future research include new architectures with reduced off-chip components, further enhancing power handling and lowering noise figure via advanced silicon technologies, as well as scaling the design beyond 6 GHz and into millimeter-wave frequencies.

Chapter 3

A Passive-Mixer-First Acoustic-Filtering Receiver Chipset Using Mixed-domain Recombination for Spectral Interference

**

3.1 Introduction

Radio-frequency (RF) front-end designs are becoming increasingly challenging, as a modern mobile device has to support many frequency bands with numerous FE switches and acoustic filters [11]. The cost and size of next-generation RF FEs are further stressed by the trend towards multi-in-multi-out (MIMO), broadband, and dynamic spectrum access.

Many silicon-based integrated circuit designs for monolithic reconfigurable RF front-ends have been reported as possible alternatives to numerous fixed-frequency acoustic filters. High-order N -path filters in CMOS provide acoustic-filter-like selectivity at close-in offset frequencies but have limited tuning range and rarely operate above 2 GHz due to lossy coupling networks, parasitic effects, and the need of multi-phase square-wave RF clocks[36], [50]. Q -enhanced LC -resonator-based RF band-pass filters have been demonstrated with wide frequency tuning ranges, but they suffer from elevated noise levels and degraded linearity as active components are utilized for achieving high- Q on chip [37]. Mixer-first direct-conversion or low-intermediate-frequency (low-IF) receivers are also widely tunable and have excellent

**This chapter is adopted from author's own works [78], [79]

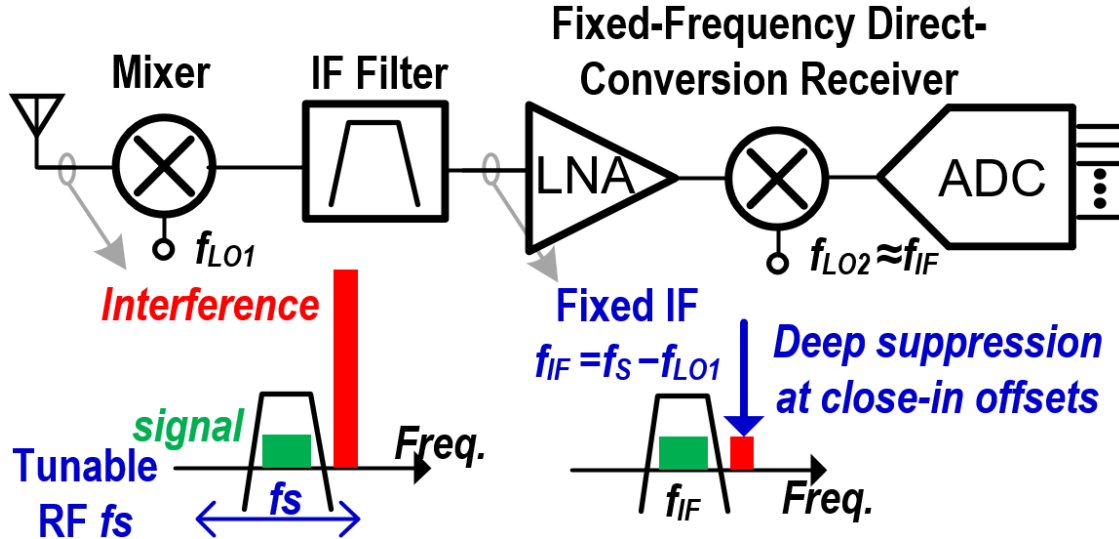


Figure 3.1: High-IF mixer-first superheterodyne front-end: conceptual diagram.

out-of-band (OOB) linearity in the presence of blockers at far-out frequency offsets; however, they have limited suppression and linearity for close-in interference [38]–[41], [54]. Finally, filtering-by-aliasing receivers have been reported with superior close-in interference suppression but are limited to sub-1-GHz RF operation even when implemented in advanced CMOS nodes [80].

By combining a passive or parametric mixer and high-order filters in a mixer-first high-IF superheterodyne architecture, several recent works have demonstrated a new direction for reconfigurable RF front-ends [32], [33], [81], [82]. The idea is straightforward (see Fig. 3.1). The mixer converts the frequency of an incoming signal to a fixed high IF. Then, an IF high-order filter with a sharp filtering response suppresses interference before connecting to active components that are prone to high-power interference. By varying the mixer local oscillator (LO) frequency, these mixer-first superheterodyne reconfigurable front-ends [32], [81] provide widely-tunable RF operations with a much smaller filter count compared to an exhaustive filter bank design (e.g. [11]).

Using parametric varactors modulation, low-noise and input-matched superheterodyne mixer-first RF front-ends have been demonstrated in [81], [82]. However, in a parametric mixer, both the LO and signal voltages are across the same two terminals of each varactor, resulting in spurious inter-modulation signals that are removed using bulky isolators in [81]. Also, parametric varactors modulation is inherently non-linear, deteriorating the mixer linearity performance especially for low-cost CMOS implementations [83].

Unlike the non-linear varactor-based parametric converters, linear periodically time-varying (LPTV) N -path passive mixers using transistor switches are highly linear [53]. A gigahertz-high-IF passive-mixer-first RF front-end using a surface-acoustic-wave (SAW) IF

filter – *essentially a passive-mixer-first acoustic-filtering front-end* – has been demonstrated with matched RF input, low noise, and high linearity in [32]. The key challenge associated with a passive-mixer-first acoustic-filtering superheterodyne front-end is the impedance aliasing that arises from 1) a high-IF superheterodyne architecture and 2) non-negligible out-of-band (OOB) impedance from IF acoustic filters [33]. An *LC*-based impedance shaping network has been introduced in [32] to suppress the impedance aliasing, concurrently achieving input matching, low noise, and high linearity. However, the work in [32], [33] uses many off-chip IF passive components and only has an RF bandwidth (BW) of 65 MHz.

In [78], we presented a mixer-first acoustic-filtering front-end with a new IF-and-baseband mixed-domain recombination architecture. Compared to the prior work [32], [33] that uses IF-only recombination, the proposed mixed-domain recombination supports a wider instantaneous BW and higher RF while reducing the number of IF passive components that are lossy and bulky.

This article is an expanded version from [78]. An overview of bulk-acoustic wave (BAW) filter basics and a new simplified *N*-path commutated-*LC* circuit analysis are described in Section II. Section III introduces the mixer-first acoustic-filtering RF front-end using mixed-domain recombination with additional analyses and discussions on image-rejection, frequency planning, and noise performance. More implementation and simulation details are reported in Section IV. Finally, updated and additional measurement results with more detailed discussions are presented in Section V.

3.2 LPTV Mixer-First Acoustic-Filtering Front-End

We start with a brief review of the key characteristics and challenges associated with acoustic filters. Understanding of these plays a pivotal role in engineering an RF front-end architecture with desired system-level performance. Then, we introduce LPTV passive-mixer-first acoustic-filtering front-ends and its architecture evolution using a new energy-conservation-based analysis for switched-band-pass-filter circuits.

3.2.1 RF Acoustic Filters

Acoustic wave propagation in common RF materials have orders-of-magnitude smaller wavelength and lower loss compared to those in their electromagnetic counterparts [84]. Due to these fundamental advantages, acoustic filters have low loss, high selectivity, and compact form factors, resulting in their pervasiveness in modern commodity mobile devices.

A high-frequency acoustic filter often consists of several bulk-acoustic wave (BAW)

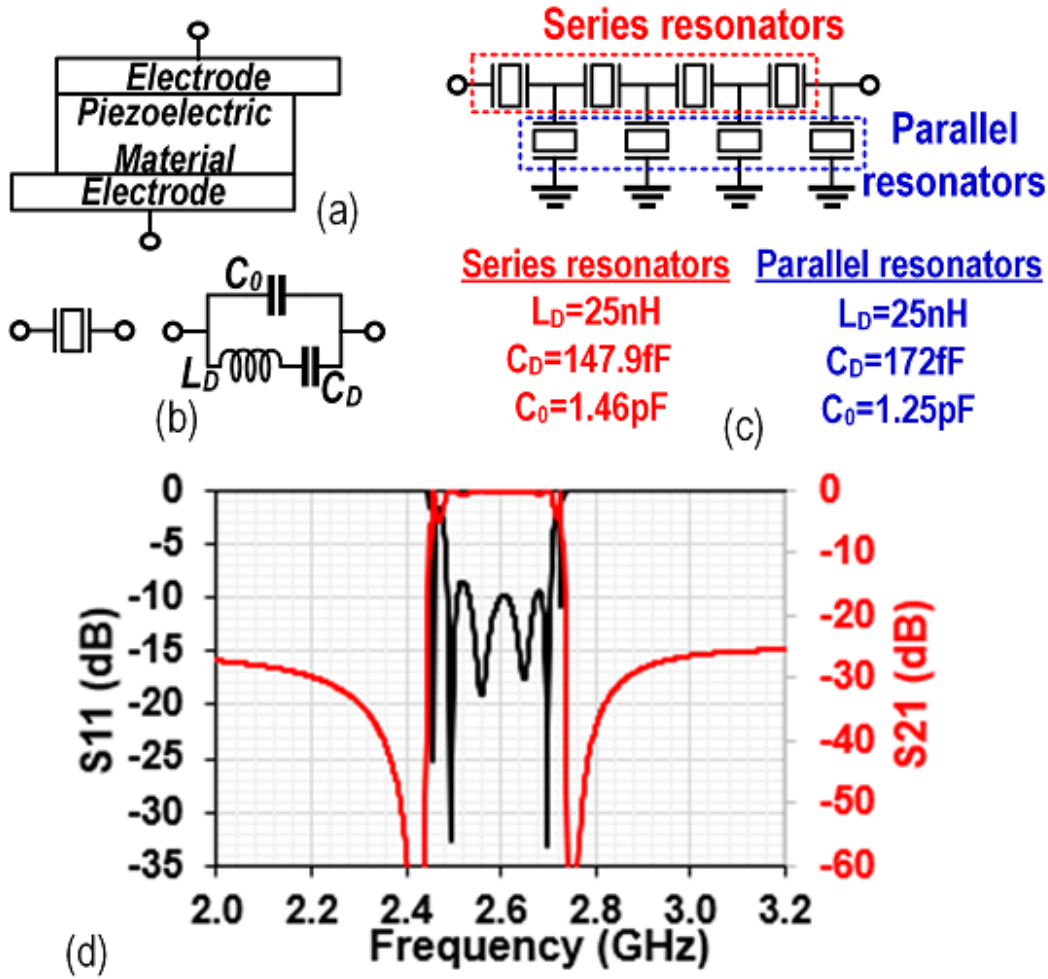


Figure 3.2: BAW ladder filter: (a) BAW resonator structure, (b) BAW resonator Butterworth-Van-Dyke (BVD) model, (c) a design example and (d) its simulated S-parameters.

resonators, while surface-acoustic wave (SAW) resonators are typically deployed for low frequency (e.g. below 2 GHz) applications [12], [85]. Given that the fractional bandwidths of acoustic filters are fundamentally limited by the efficiency of their electromechanical transduction [84], [85], we focus on BAW filters in this article as their high-frequency operation results in wide instantaneous bandwidths. A simplified BAW resonator structure is depicted in Fig. 3.2(a), consisting of a layer of piezoelectric material sandwiched between two metal electrodes [12]. The resonance frequency is determined by the thickness of the piezoelectric material layer and the thickness and mass of the electrodes. The electrical behavior of a BAW resonator can be approximately captured by an equivalent circuit using the Butterworth-Van-Dyke (BVD) model [12], [14], [67] as shown in Fig. 3.2(b) where C_0 is the static capacitance, L_D and C_D are dynamic (also called motional) inductor and capacitor, respectively.

By connecting several BAW resonators in a ladder topology, an acoustic filter can be constructed as depicted in Fig. 3.2. Although they are on the same wafer and, hence, have the same thickness of the piezoelectric material layer, the shunt resonators have lower resonance frequencies compared to the series ones by introducing a mass loading layer [85]. Following the principles summarized in [85], we build an acoustic filter made of BVD-based resonators centering at 2.6 GHz with a bandwidth of 200 MHz [see Fig. 3.2(c)]. The simulated filter S-parameters are shown in Fig. 3.2(d) with nearly zero insertion loss, excellent close-in and OOB rejection, and good input/output return loss.

Despite their pervasiveness, existing acoustic filter technologies face a couple of key challenges for future high-frequency and broadband RF applications. Firstly, acoustic filters generally cannot be tuned across a wide frequency range and have somewhat fixed and pre-defined operation frequencies which are defined by the thickness and mass of the building materials. As more frequency bands are set to become available, e.g. the advent of sub-6-GHz 5G and WiFi 6, a whopping 100 filters are expected in a next-generation mobile device [14]; this imposes significant challenges on RF front-ends in terms of cost, size, and design complexity. Secondly, acoustic filters often provide superior performance only up to 3 GHz. Scaling acoustic filters beyond 3 GHz faces many fundamental challenges as the thicknesses of acoustic structures become too small at high frequencies to be manufactured in a low-loss, low-cost, and reliable fashion [43], [84].

3.2.2 Mixer-First Acoustic-Filtering RF Front-End

Mixer-first high-IF acoustic-filtering front-ends address the aforementioned key challenges faced by acoustic filters.

As depicted in Fig. 3.1, the input RF of a high-IF mixer-first acoustic-filtering front-end is jointly defined by the LO frequency and the IF acoustic filter center frequency. By varying the LO frequency, the front-end RF can be made widely tunable with fixed-frequency acoustic filters. Moreover, a mixer-first acoustic-filtering front-end allows relatively low-frequency acoustic filters being used at high-frequency bands as signals are frequency down-converted prior entering the filters.

Mixer-first high-IF acoustic-filtering front-ends are distinguishable from monolithic mixer-first direct-conversion receivers [38]–[41], [54] by their IF choices [33], [78].

In a mixer-first direct-conversion receiver, a low or zero IF is used for a high integration level and low cost. For sub-6-GHz frequency bands, the upper frequencies of IF passbands are less than a couple of hundred megahertz. This relatively low upper frequency limit would make *LC*-based IF filters unacceptably bulky, and acoustic filters in this frequency range

have very narrow bandwidth (tens of kilohertz to a few megahertz, e.g. [86], [87]). Therefore, active RC -based baseband filters are often utilized in sub-6-GHz mixer-first direct-conversion receivers [38]–[41], [54]. However, active filters limit the front-end frequency selectivity at RF and the linearity at close-in frequency offsets.

In a mixer-first acoustic-filtering front-end, a high IF allows compact all-passive high-order filters with broad instantaneous bandwidth, providing deep suppression of adjacent channel interference with high linearity. The superior selectivity, linearity, and center frequency tunability of a passive-mixer-first acoustic-filtering front-end come at the expense of requiring off-chip acoustic filters and being not able to widely adjust filtering bandwidths, when compared to monolithic mixer-first direct-conversion receivers [38]–[41], [54]. The development of heterogeneously integrated mixer-first acoustic-filtering front-ends with tunable filtering bandwidths (e.g. [88]) could be an interesting future research topic.

3.2.3 Evolution and Analysis of Switched-BPF Circuits

Here, we present the evolution of mixer-first acoustic-filtering front-ends using a new energy-conservation-based analysis for switched-band-pass-filter circuits.

A mixer-first acoustic-filtering front-end can be simply constructed by having a double-balanced passive mixer in front of an IF filter [see Fig. 3.3(a)]. We use a second-order RLC band-pass filter first and replace it with acoustic filters later.

Let us derive the conversion gain and the input impedance of a double-balanced RF mixer with a narrow-band RLC load where the mixer LO or clock frequency f_C is significantly larger than the RLC filter 3-dB bandwidth. While double-balanced RF mixers have been studied extensively, most existing analyses have assumed either a purely resistive or an RC load [9], [89].

Given a sinusoid source voltage $v_S = V_S \sin(\omega_S t + \phi)$ where ω_S is the sum of the mixer LO frequency ω_C and the LC resonance frequency ω_O , we find the output voltage can be approximated as $v_O = V_O \sin(\omega_O t + \phi + \theta)$, i.e. a sinusoid with a constant amplitude V_O and phase shift θ . Intuitively, the output is a sinusoid as the high- Q RLC tank suppresses all the LO harmonics except at the resonance frequency $\omega_O = (LC)^{-0.5}$. In the steady state, the output amplitude can be approximated as a constant since the time constant of our high- Q RLC tank $2\pi RC$ is much larger than the LO period $1/f_C$.

To sustain a constant envelop sinusoid, the energy dissipated by the lossy RLC tank and the source resistance has to be replenished by the voltage source over time. This results in

$$\frac{V_O^2}{2R_L} MT_C = \int_0^{MT_C} \frac{v_S - v_{IN}}{R'_S} v_{IN}, \quad (3.1)$$

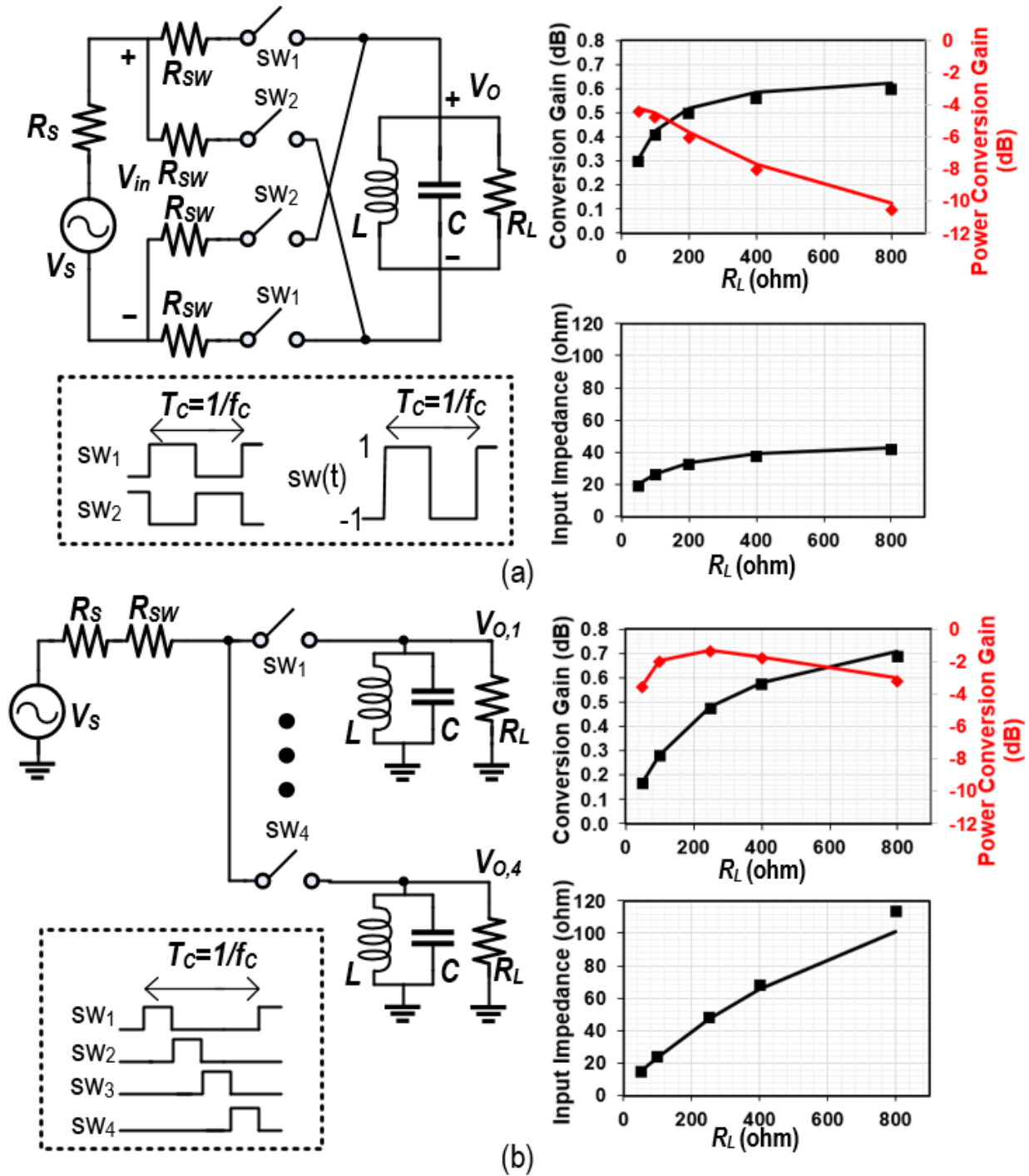


Figure 3.3: Calculated (markers) using (3.2)(3.3)(3.5)(3.6) and simulated (lines) switched-LC circuit conversion gain and input impedance ($R_S = 50$ ohm, $f_C = 2$ GHz, $f_O = 1/(2\pi\sqrt{LC}) = 2.6$ GHz): (a) a double-balanced passive mixer with an $R_L C$ tank ($R_{SW} = 3$ ohm and $R_L C$ tank Q of 30), and (b) a 4-path switched-LC circuit ($R_{SW} = 5$ ohm and $R_L C$ tank Q of 10).

where M is the number of mixer LO periods, $T_C = 1/f_C$, $v_{IN} = v_O(t)sw(t)$, $sw(t)$ is the square-wave LO waveform given in Fig. 3.3(a), and $R'_S = R_S + 2R_{SW}$ is the sum of source

and switches resistances.

Substituting $v_{IN} = v_O(t)sw(t) = v_O = V_O \sin(\omega_O t + \phi + \theta) \cdot sw(t)$ and $v_S = V_S \sin(\omega_S t + \phi)$ into (3.1) and letting $M \rightarrow \infty$, we arrive at the double-balanced mixer conversion gain as:

$$CG_{\text{DB}} = \frac{|V_o(\omega_O)|}{|V_s(\omega_S)|} = \frac{2\pi R_L}{\pi^2 R'_S + 8\alpha R_L}, \quad (3.2)$$

where $\alpha = \sum_{h=1}^H \frac{1}{(2h-1)^2}$ and H is the number of LO harmonics. It has been shown that given a high- Q RLC load with negligible load impedance at LO harmonics $f_O \pm k f_C$ where k is a non-zero integer, the RF input impedance $R_{in,\text{DB}}$ of the circuit in Fig. 3.3(a) is purely resistive [33], [90]. With that, θ can be determined as $\pi/2$. Meanwhile, the RF input impedance can be expressed as:

$$R_{in,\text{DB}} = \frac{V_{in}(\omega_S)}{I_{in}(\omega_S)} = \frac{R'_S R_L}{\pi^2 R'_S / 4 + (2\alpha - 1)R_L} + 2R_{SW}. \quad (3.3)$$

A design example is used to verify (3.2)(3.3) with $R_S = 50$ ohm, $R_{SW} = 3$ ohm, $f_C = 2$ GHz, $f_O = 1/(2\pi\sqrt{LC}) = 2.6$ GHz, and $R_L LC$ tank Q of 30, and varying R_L . The calculated and Cadence Spectre RF simulated conversion gains at 2.6-GHz IF and input impedance at 4.6-GHz RF are plotted in Fig. 3.3(a), showing a good match. Power conversion gain, defined as the ratio between the power delivered to R_L at f_O and the maximum available power from the source, can be readily calculated using (3.2). The simulated input impedance imaginary parts are much smaller compared to its real parts, hence are omitted in Fig. 3.3(a).

From (3.2)(3.3), we know that a double-balanced passive mixer cannot achieve input matching and low power loss at the same time. As in Fig. 3.3(a), the input impedance increases with R_L , and a R_L of 800 ohm results in an RF input impedance of 42 ohm. However, this results in a -10 -dB power gain, or a 10-dB power loss. Alternatively, a 50-ohm input impedance can be obtained by increasing R_{SW} , but this increases power loss as well as more power will be dissipated by R_{SW} .

An N -path switched- LC circuit breaks the matching-loss trade-off as the multiple paths result in reduced harmonic components at RF [33], similar to that in an N -path switched- RC circuit [18], [21], [90]. Here, conservation of energy is applied to the 4-path switched- LC circuit in Fig. 3.3(b), resulting in

$$\frac{V_O^2}{2R_L} MT_C = \sum_{m=0}^{M-1} \int_{mT_C + (k-1)T_C/4}^{mT_C + kT_C/4} \frac{v_S - v_{O,k}}{R'_S} v_{O,k}. \quad (3.4)$$

where k corresponds to the k -th path of the 4-path switched- LC circuit in Fig. 3.3(b).

Substituting $v_{O,k} = V_O \sin[\omega_O t + \phi + \theta + (k-1)\pi/2]$ and $v_S = V_S \sin(\omega_S t + \phi)$ into (3.4)

and letting $M \rightarrow \infty$, we arrive at the conversion gain and the input impedance of the 4-path switched- LC circuit as

$$CG_{4path} = \frac{|V_{o,k}(\omega_O)|}{|V_s(\omega_S)|} = \frac{2\sqrt{2}}{\pi} \frac{R_L}{R_L + 4R'_S}, \quad (3.5)$$

$$R_{in,4path} = R_{SW} + R_{sh} || (\gamma R_L), \quad (3.6)$$

where $R_{sh} = R'_S \frac{N\gamma}{1-N\gamma}$, $\gamma = \frac{\text{sinc}^2(\pi/N)}{N}$, and we've assumed $2f_{IF}$ does not equal integral multiples of f_C and let $\theta = \pi/4$ for resistive input impedance. The generalized analysis in [33] yields the same results when loaded with high- Q RLC tanks.

Figure 3.3(b) shows a design example with $R_S = 50$ ohm, $R_{SW} = 5$ ohm, $f_C = 2$ GHz, $f_O = 1/(2\pi\sqrt{LC}) = 2.6$ GHz, $R_L LC$ tank Q of 10, and a varying R_L . The calculated and simulated conversion gains at 2.6-GHz IF and input impedance at 4.6-GHz RF are plotted in Fig. 3.3(b), showing a good match. Power conversion gain, the ratio between the power delivered to all load resistors at f_O and the maximum available power from the source, can be readily calculated using (3.5). The simulated input impedance imaginary parts are much smaller compared to its real parts, hence are omitted in Fig. 3.3(b).

As shown in Fig. 3.3(b), a matched input impedance of around 50 ohm and low power loss of 1.4 dB can be achieved simultaneously in a 4-path switched- LC circuit with R_{SW} of 5 ohm and R_L of 250 ohm.

Next, let us replace the LC filter in Fig. 3.3(b) with the 2.6-GHz BVD-based BAW filter given in Fig. 3.2(c). The switched-BAW-filters circuit is shown in Fig. 3.4(a) with $R_S = 50$ ohm, $R_{SW} = 5$ ohm, $f_C = 2$ GHz, $f_O = 1/(2\pi\sqrt{LC}) = 2.6$ GHz, and ideal 2.2:1 transformers to boost the in-band impedance from 50 ohm to 250 ohm.

However, directly replacing the LC filter with the BAW filter results in poor RF input matching of around -5 dB and excess power loss of 7 dB as in Fig. 3.4(a). We attributed the sharp performance degradation to *impedance aliasing* as detailed in [33]. Compared to a second-order RLC filter, a high-order BAW filter together with its inter-chip connections have significant impedance at out-of-band LO harmonic frequencies. Through the switching-based mixing operation, the load impedance Z_L components at the LO harmonic frequencies are all translated to RF, becoming indistinguishable, or aliases of one another. Therefore, impedance aliasing degrades input matching and introduces excess loss; this is especially prominent with a wide RF range, as a large number of RF impedances can be aliased.

We found in [32], [33] that it is possible to mitigate impedance aliasing by suppressing the Z_L at out-of-band LO harmonic frequencies via an impedance shaper as shown in Fig. 3.4(b). The shunt LC circuit with a tank Q of 10 provides low impedance path at out-of-band LO

harmonic frequencies, restoring the RF input matching and reducing power loss from 7 dB to 2.5 dB. The simulated input reflection and power loss are slightly worse compared to those predicted by (3.5)(3.6) due to the finite impedance suppression provided by the LC impedance shaper.

3.3 Mixer-First Acoustic Filtering Using Mixed-Domain Recombination

Despite favorable input matching and power loss, the mixer-first acoustic-filtering front-end in Fig. 3.4(b) requires four IF paths and lacks analog-domain image rejection. Each IF path consists of an acoustic filter and an IF receiver. Having too many IF paths increases the system cost, size, and power consumption. Without analog-domain image rejection, an image-band blocker could stress the receiver baseband and analog-to-digital converter (ADC) dynamic range requirements, again, adding cost, size, and power consumption.

To reduce the IF paths count and to suppress image-band interference, an IF recombination network was introduced in [32] (see Fig. 3.5). With the IF recombination, the filtering front-end resembles a Hartley image-rejection receiver which needs a 90° phase shift and a signal summation before the IF filter [9], [89]. For high linearity, a lumped CLC phase shifter and a transformer balun were used as in Fig. 3.5.

However, the mixer-first acoustic filtering with the IF-only recombination in Fig. 3.5 comes with two drawbacks.

First, the usage of many lossy IF passive components degrades the sensitivity of the front-end. To reduce the loss of passives, a low IF is preferred as electromagnetic-induced losses typically increase with frequency. But, a low f_{IF} results in narrow acoustic filter bandwidth $f_{BW} = k_{FBW} \times f_{IF}$ as the fractional bandwidth k_{FBW} is fundamentally limited by the electromechanical coupling [85], [91]. Also, a low IF reduces image-band blocker filtering as detailed in Section III-C.

Another drawback lies in the capability of coping with in-phase and quadrature (I-Q) imbalance which needs to be kept small for high image rejection. Tuning IF passive components can compensate the I-Q imbalance, but it comes with significant loss penalty especially with inductance tuning.

3.3.1 Architecture

In this work, we propose a new IF-and-baseband mixed-domain recombination architecture for mixer-first acoustic filtering as shown in Fig. 3.6. Following a 4-path switched- LC passive

mixer, there are two on-chip transformer baluns. Each I- or Q-path balun acts as the LC impedance shaper inductor and the first-stage IF recombination that merges 4 paths into 2, halving the IF filter and receiver count. After the IF BAW filters suppressing out-of-band interference, two IF quadrature direct-conversion receivers are adopted. The I-Q baseband outputs of the IF receivers are connected, acting as the second-stage recombination at baseband.

Quantitatively, the RF front-end operates as follows.

Modeling an incoming desired signal as a sinusoid $V_S \cos(\omega_s t)$ and the RF front-end mixer differential LOs as $\cos(\omega_{LO1} t + \phi_{LO1})$ and $\sin(\omega_{LO1} t + \phi_{LO1})$, the outputs at IF after the RF mixer and IF recombination can be expressed as $x_I = g_1 V_S \cos(\omega_{IF} t - \phi_{LO1})$ and $x_Q = -g_1 V_S \sin(\omega_{IF} t - \phi_{LO1})$, where $\omega_{IF} = \omega_s - \omega_{LO1}$ and g_1 is the RF front-end conversion gain.

Since the IF receivers and the baseband recombination in Fig. 3.6 form a complex mixer [92], let us define $x = x_I + jx_Q$, $y = y_I + jy_Q$ and $w = w_I + jw_Q$, where y_I and y_Q are the outputs after the IF BAW filters and w_I and w_Q are the IF mixer I-Q LOs. This way, the final outputs after the baseband recombination can be written as $z = z_I + jz_Q = g_2 y \cdot w$, where g_2 is the IF receiver conversion gain.

Given $x = g_1 V_S e^{-j(\omega_{IF} t - \phi_{LO1})}$, we have $y = g_1 g_F(\omega_{IF}) V_S e^{-j[\omega_{IF} t - \phi_{LO1} + \phi_F(\omega_{IF})]}$, where $g_F(\omega_{IF})$ and $\phi_F(\omega_{IF})$ are the magnitude and phase responses of the BAW filter at ω_{IF} , respectively.

Finally, assuming the IF mixer LOs as $w = w_I + jw_Q = e^{j(\omega_{LO2} t + \phi_{LO2})}$, the final complex output is

$$z_S = g_2 y \cdot w = g_1 g_F(\omega_{IF}) g_2 V_S e^{j[\omega_{BB} t + \phi_{LO} - \phi_F(\omega_{IF})]}, \quad (3.7)$$

where $\omega_{BB} = \omega_{LO2} - \omega_{IF} \approx 0$ and $\phi_{LO} = \phi_{LO1} + \phi_{LO2}$.

From (3.7), we see that the desired incoming signal at ω_S is received at baseband, while a strong close-in blocker is suppressed significantly thanks to the high frequency selectivity in BAW filter gain g_F .

If an image-band interference $V_{IM} \cos(\omega_{IM} t)$ enters the front-end, where $\omega_{IM} = f_{IF} - (f_S - f_{IF}) = 2f_{IF} - f_S$, the complex output after the IF filters becomes $y_{IM} = g_1 g_F V_{IM} e^{j(\omega_{IF} t + \phi_{LO1} + \phi_F)}$. The output at the receiver baseband is

$$z_{IM} = g_2 y_{IM} \cdot w = g_1 g_F(\omega_{IF}) g_2 V_{IM} e^{j[2\omega_{IF} t + \phi_{LO} + \phi_F(\omega_{IF})]}. \quad (3.8)$$

This means that the image signal is frequency translated to a much higher frequency ($2\omega_{IF} \gg \omega_{BB}$) and can be subsequently filtered along the receiver baseband chain.

When compared with the prior IF-only recombination design in Fig. 3.5, the new mixed-domain architecture pushes the 90° phase shift and final stage recombination from the IF signal path to IF receiver LO path and baseband, respectively.

By having LO-path phase shift and baseband recombination after the IF receiver low-noise amplifier (LNA), their associated noise penalty is minimized. Also, comparing to the intrinsically narrowband signal-path *CLC* phase shifter, LO-path 90° phase shifting is broadband and readily available in high-performance IQ receivers.

Compared to the IF-only recombination design, it is less lossy to incorporate a higher IF in the proposed architecture as the mixed-domain recombination eliminates the IF *CLC* phase shifter and final stage IF transformer balun. This high IF enables a wider acoustic filter bandwidth as it is proportional to its center frequency. A high IF also eases the filtering of image-band blocker as detailed in Section III-C.

The benefits of our proposed architecture come at the expense of requiring one more IF acoustic filter and receiver. However, since only two *identical* acoustic filters are needed, they can be fabricated together using the same process and, hence, have a significantly lower cost compared to having two acoustic filters at different frequencies [11]. In fact, it is essential to use two adjacent acoustic filters on the same die to reduce the I-Q mismatch in the proposed mixed-domain recombination architecture as discussed shortly in Section III-B. The additional IF receiver does consume more power and chip area, but it reduces the front-end noise figure (see Section III-D) and modern inductorless receivers in nanoscale CMOS processes are compact and power efficient.

Our proposed architecture resembles a Weaver image-rejection receiver but has two distinctions compared to prior works (e.g. [93]). Firstly, eliminating the RF LNA and utilizing a mixer-first design significantly enhances the front-end dynamic range. Secondly, the choice of a gigahertz IF allows us to use high-linearity passive acoustic filters to replace active filters. Also, a gigahertz high IF leads to a wide frequency separation between the image band and the desired signal band, easing the design of a high-pass image filter [94].

A conceptual comparison between our proposed mixer-first acoustic filtering and a conventional filter-bank-based front-end is depicted in Fig. 3.7. In a conventional multi-band RF front-end, a bank of acoustic filters with different center frequencies connects to an antenna via a static RF single-pole-multi-throw switch and matching networks (MNs) [12], [14]. Each acoustic filter is then connected to a dedicated radio-frequency integrated circuits (RFIC) LNA. A multiplexer switch selects one of the LNAs for further signal processing [95]. This approach requires a large number of different filters and lacks flexibility to incorporate future frequency bands after deployment in the field. Our design effectively makes the single-pole-multi-throw RF switch periodically rotate among a bank of identical filters, making the

input frequency programmable and jointly defined by the switch rotational or commutation frequency and the filter center frequency.

3.3.2 I-Q Mismatch and Image Rejection Compensation

One challenge in our architecture is the I-Q mismatch which leads to degraded image rejection. While it has been shown that image rejection can be obtained in the digital domain [96], an image-band blocker could stress the dynamic range requirement of the analog front-end and saturate the receiver.

Let us re-calculate the image-band response in presence of I-Q mismatches. Assume that the I-Q mismatch is dominated by the the BAW filters, including the BAW-RFIC interconnects, and the I-Q BAW filters have magnitude and phase responses of $[1 \pm \Delta g(f)]g_F(f)$ and $\phi_F(f) \pm \Delta\phi_F(f)$, respectively. The receiver normalized complex baseband output can be found as

$$\begin{aligned} \frac{z_{IM,mis}}{g_1 g_F(\omega_{IF}) g_2 V_{IM}} &\approx e^{j[2\omega_{IF}t + \phi_{LO} + \phi_F(\omega_{IF})]} \\ &- \Delta g(\omega_{IF}) \cdot e^{j[\omega_{BB}t - \phi_{LO} - \phi_F(\omega_{IF})]} \\ &+ j\Delta\phi_F(\omega_{IF}) \cdot e^{j[\omega_{BB}t - \phi_{LO} - \phi_F(\omega_{IF})]}, \end{aligned} \quad (3.9)$$

where we have neglected higher-order mismatch terms, e.g. terms that include $\Delta g \cdot \Delta\phi_F$.

Comparing (3.8) and (3.9), we see that the second and the third terms in (3.9) are the results of I-Q mismatches. They fall inside the receiver passband after IF mixers, corrupting the desired signal. This finite image rejection is quantified through image rejection ratio (IRR) [9], and it can be found from (3.9) that $IRR = 10\lg(\Delta g^2 + \Delta\phi_F^2)$.

To quantify the amount of gain and phase mismatches, we measured two Qorvo QPQ1285 BAW filters. As shown in Fig. 3.8, the worst-case gain and phase mismatch of 0.2 dB and 7 degree are observed. This mismatch results in 24 dB image rejection based on (3.9).

To suppress the spurious tones in (3.9) due to I-Q mismatches, we introduce I-Q mismatch compensation circuitry at baseband akin to that in [93]. As shown in Fig. 3.9, after each IF receiver mixer, there is a vector modulator, VM_{ij} where $i, j = I, Q$. Each vector modulator consists of a main input and an auxiliary input. The signal for the main input is first directly fed to the vector modulator output with unity gain, corresponding to the same component from that (see Fig. 3.6) without I-Q mismatch compensation. In addition, each vector modulator imparts adjustments to its main and auxiliary path magnitudes for I-Q mismatch compensation, through weights M_{ij} and A_{ij} , respectively.

Assuming the IF receiver LO I-Q mismatch is negligible after calibration, the vector modulator I-Q mismatch compensation conditions at the I path are:

$$\begin{aligned}\sqrt{M_{II}^2 + A_{II}^2} &= \frac{1}{1 + \Delta g}, \arctan \frac{A_{II}}{M_{II}} = -\Delta\phi_F, \\ \sqrt{M_{QQ}^2 + A_{QQ}^2} &= \frac{1}{1 - \Delta g}, \arctan \frac{M_{QQ}}{A_{QQ}} = \Delta\phi_F.\end{aligned}\tag{3.10}$$

I-Q mismatch at the Q path can be similarly compensated using vector modulators VM_{IQ} and VM_{QI} .

Satisfying (3.10) across a wide instantaneous bandwidth is challenging due to the frequency selectivity difference between the vector modulators and the I-Q mismatches Δg and $\Delta\phi_F$. This challenge associated with wideband I-Q mismatch compensation is known (e.g. see [93], [94]) and similar to the challenge of wideband self-interference cancellation using frequency-flat vector modulators [97], [98]. Using two adjacent acoustic filters from the same die should reduce I-Q mismatches, increasing the image rejection bandwidth. Also, replacing frequency-flat vector modulators with multi-tap analog filters should also increase the image rejection bandwidth as demonstrated in broadband interference cancellation [99], [100].

Fortunately, in addition to widening the instantaneous bandwidth, a high IF allows us to use a fixed-frequency high-pass filter to provide additional image filtering as discussed in Section III-C.

3.3.3 Image Filtering and Frequency Planning

The high-IF architecture of the proposed widely-tunable filtering front-end allows us to insert a fixed-frequency RF high-pass filter for additional image suppression. Given an IF and an image filtering requirement, we can determine the front-end RF range.

We start with a high IF that satisfies the instantaneous bandwidth requirement. With an IF of 2.6 GHz, a 6.5% filter fractional bandwidth results in an instantaneous bandwidth of 170 MHz.

The proposed widely-tunable RF front-end with an input fixed-frequency high-pass filter is depicted in Fig. 3.10. As shown in Fig. 3.10(b), when $f_{LO1} < f_{IF}$, the signal and image bands are located at $f_S = f_{LO1} + f_{IF}$, and $f_{IM} = f_{IF} - f_{LO1}$, respectively. On the other hand, when $f_{LO1} \geq f_{IF}$, the signal remains at $f_S = f_{LO1} + f_{IF}$ but the image band changes to $f_{IM} = f_{LO1} - f_{IF}$.

To ease the RF high-pass filter design requirements, the separation between the lowest

signal frequency $f_{S,L}$ and the highest image frequency $f_{IM,H}$ should be maximized. If the lowest signal frequency is given as $f_{S,L} = f_{LO1,L} + f_{IF}$, where $f_{LO1,L}$ is the lowest front-end mixer LO frequency, the highest image frequency is $f_{IM,H} = f_{LO1,L} - f_{IF} = 2f_{IF} - f_{S,L}$. When front-end mixer operates with an LO frequency of $f_{LO1,L}$ (the signal and image interference at $f_{S,L}$ and $f_{IM,H}$, respectively), we can write the worst-case image filtering ratio (IFR) as

$$IFR_{\min} = \alpha \cdot 20 \lg \frac{f_{S,L}}{2f_{IF} - f_{S,L}}, \quad (3.11)$$

where α is the order of the RF high-pass filter. Given $\alpha = 5$ and an IFR_{\min} of 30 dB, we have $f_{S,L} = \frac{4}{3}f_{IF}$. Given $f_{IF}=2.6$ GHz, $f_{S,L} = \frac{4}{3}f_{IF}=3.47$ GHz and $f_{IM,H} = 2f_{IF} - f_{S,L}=1.73$ GHz.

Since a fixed-frequency high-pass filter is used, the highest signal frequency $f_{S,H}$ is set by $f_{S,H} - 2f_{IF} = 2f_{IF} - f_{S,L}$ to retain the worst-case image filtering ratio IFR_{\min} in (3.11). This gives us $f_{S,H} = \frac{8}{3}f_{IF}$. Given $f_{IF}=2.6$ GHz, $f_{S,H} = \frac{8}{3}f_{IF}=6.94$ GHz.

Like other high-IF superheterodyne receivers, LO feedthrough can potentially saturates the subsequent IF receivers [94]. Specifically, the RF LO can leak to the IF filters, and if the RF LO is inside the IF filter passband, it can reach the IF receiver causing possible saturation. The most significant LO feedthrough happens when $f_{LO1} = f_{IF}$, corresponding to a 5.2-GHz RF. Symmetrical mixer designs and an LO leakage cancellation circuitry (e.g. [101]) can be used to reduce the LO feedthrough.

The RF LO also can leak to the antenna port similar to mixer-first direct-conversion receivers. Unlike a direct-conversion mixer-first receiver, the LO leakage can be filtered by the input high-pass filter in our high-IF mixer-first superheterodyne front-end. For the RF range of 3.5 to 6.1 GHz, the front-end mixer LO frequency is from 0.9 to 3.5 GHz. This f_{LO1} range is outside of the high-pass filter passband, and the corresponding LO leakage will be suppressed.

3.3.4 Noise Analysis

Here, we calculate the noise figure of the mixer-first acoustic-filtering front-end with proposed mixed-domain recombination. We ignore all reactive components for our in-band noise analysis for simplicity.

Looking at Fig. 3.6, first, the total output noise at the I or Q path is $4K_{fold}^2 g_1^2 g_F^2 g_2^2 \overline{V_{n,RS}^2}$, where g_1 , g_F , g_2 are (conversion) gain of the front-end mixer, IF filter, and IF receiver, respectively, as used in Section III-A, and $K_{fold} \approx 1.13$ is a constant that factors in the noise folding effect of 25% duty-cycle 4-path mixing [102]. The factor 4 is due to the fact that the summing noises at the receiver baseband are correlated as they both originate from the same

source noise $\overline{V_{n,RS}^2}$.

Second, the contribution of the IF receiver can be determined. The IF receiver consists of two paths that combine at the baseband output, and each path has its own LNA, mixer, and baseband transconductance cells as in Fig. 3.6. Given the noise figure of a standalone single path to be F_{RX} , the total output noise at the I or Q output due to the entire IF receiver is $2(F_{RX} - 1)g_2^2\overline{V_{n,RIF}^2}$, where g_2 is the conversion gain of the standalone single-path receiver as in Section III-A, $\overline{V_{n,RIF}^2}$ is the source noise of F_{RX} . Since the thermal noise of an LTI passive network can be calculated from its impedance [9], we have $\overline{V_{n,RIF}^2} = 4kTR_{IF}$ where R_{IF} is the impedance looking into the IF filter from the IF receiver input. We have ignored noise folding for the IF receiver assuming the IF filters have significantly suppressed the out-of-band noise. Unlike the source noise, the noises of the two IF receiver paths are uncorrelated, resulting in the factor 2 in the total output noise.

Next, we will determine the noise contribution of the lossy RF front-end mixer and IF filters. The noise seen at the I or Q filter output is $V_{n,RIF} = K_{fold}g_1g_FV_{n,RS} + V_{n,RMF}$, where $V_{n,RS}$ is the RF source noise and $V_{n,RMF}$ is the thermal noise from the RF mixer and IF filter. Since $V_{n,RS}$ and $V_{n,RMF}$ are uncorrelated, we arrive at $\overline{V_{n,RMF}^2} = 4kT(R_{IF} - K_{fold}^2g_1^2g_F^2R_S)$. Therefore, the total output noise due to the lossy RF front-end mixer and IF filters is $2g_2^2\overline{V_{n,RMF}^2}$.

Finally, the total chipset noise factor F_{Total} can be expressed as

$$\begin{aligned} F_{Total} &= K_{fold}^2 + \frac{(F_{RX} - 1)g_2^2\overline{V_{n,RIF}^2} + g_2^2\overline{V_{n,RMF}^2}}{2g_1^2g_F^2g_2^2\overline{V_{n,RS}^2}} \\ &= \frac{1}{2}\left(K_{fold}^2 + \frac{F_{RX}}{g_1^2g_F^2} \frac{R_{IF}}{R_S}\right). \end{aligned} \quad (3.12)$$

From (3.12) we see the noise is halved which is another benefit of having a dual I-and-Q IF paths besides eliminating the lossy IF components in Fig. 3.5. This noise benefit is at the expense of increased dc power consumption using two IF receiving paths. In addition, interestingly, (3.12) tells us that reducing R_{IF} with respect to R_S also can reduce noise. The usage of I-Q mismatch compensation in Fig. 3.9 is expected to have negligible impact on the noise figure as the IF receiver noise figure is dominated by its LNAs. In Sections V-A, we compare simulated and measured noise figures with those predicted by (3.12), showing good matches.

3.4 Circuit Implementations

We devised a proof-of-concept prototype of the proposed mixer-first acoustic-filtering front-end with mixed-domain recombination using a 65 nm CMOS process and commodity BAW filters. The block diagram and schematic of the RF front-end mixer and IF receiver chipset two 2.6-GHz Qorvo QPQ1285 BAW filters are depicted in Fig. 3.11.

3.4.1 RF Passive Mixer with Asymmetric IF Transformer Balun

Similar to many mixer-first receivers and N -path filters [36], [38], [41], a differential architecture is utilized for the RF mixer front-end. A wideband 1:1 off-the-shelf transformer is served as a balun at the RF input to facilitate single-ended measurements. Also, the differential implementation reduces the source impedance seen by the mixer-first front-end, relaxing the impedance step-up transformation requirement [33].

Mixer switches are designed to have an on-resistance of $8\ \Omega$ for a balance between front-end power conversion loss and LO path DC power consumption. As in our prior work [33], the mixer switches are realized using deep-N-well transistors, allowing us to use bootstrapping resistors at their bulk nodes as depicted in Fig. 3.11(a). An on-chip divide-by-2 circuitry is used to generate the 25% duty-cycle clocks that drive the mixer switches. Ac coupling capacitors are utilized at the RF input which are also act as a first-order high-pass image filter.

While simultaneously acting as parts of the LC impedance shaper and the IF recombination, the on-chip transformer baluns could introduce significant loss in practice, desensitizing the receiver front-end. We have derived the transformer loss or efficiency analytically using a simplified model as in Fig. 3.12. The power efficiency defined as the ratio between the input and output power shown in Fig. 3.12 can be calculated

$$\eta = \left(1 + \frac{\omega_{IF}L_2}{Q_2R_{IF}} + \frac{1}{k^2} \frac{R_{IF}}{Q_1\omega_{IF}L_1} \right)^{-1}, \quad (3.13)$$

where $Q_i = \frac{\omega_{IF}L_i}{R_i}$, $i = 1$ or 2 , and we've assumed C_1 resonates with the inductive component at IF.

Based on (3.13), a low-loss or high-efficiency transformer requires high Q and coupling factors. However, there exists a trade-off between Q and coupling factors in integrated transformers. A coplanar transformer features high Q but has limited coupling. A stacked transformer has strong coupling but uses a lower thin metal layer, degrading the Q factor.

Interestingly, based on (3.13) we find that the transformer efficiency is asymmetrical between the primary and secondary winding Q factors, and the efficiency is mostly determined

by the primary Q_1 (see Fig. 3.12).

Based on this insight, we adopt a 2:2 stacked transformer achieving a high coupling around 0.9. The top thick metal is assigned to the primary resulting in a Q of 13.8 with 0.8 dB loss at 2.6 GHz IF while the secondary has a Q of 5.6 and a loss of 0.3 dB. Both the primary and secondary windings of IF transformers have inductance of 2 nH for a balance between area and power loss. The design considerations related to inductance choice are detailed in [33].

On each in-phase or quadrature path, a 5-bit switched capacitance bank is inserted between the mixer switches and IF transformer to tune the impedance shaper resonance frequency to 2.6 GHz. At each front-end balun output, an on-chip capacitor and a 2-mm bond wire form an L-shape matching network further boosting the IF load impedance.

In post-layout simulation, when loaded with 50-ohm termination, the RF mixer front-end has a power conversion loss of 5 dB and input matching of -13 dB with a 3.5 GHz RF. Based on (3.5), the minimal achievable loss is 1.6 dB with $8\text{-}\Omega$ R_{SW} . We found additional 1.7-dB loss due to the RF switch parasitics, 1.4-dB loss from the on-chip transformer balun, and another 0.3-dB loss due to the on-chip first-order high-pass filter capacitor, as well as finite LO rising and falling times.

3.4.2 IF Complex Receiver with I-Q Mismatch Compensation

As to the IF receiver, each I or Q path consists of a resistive feedback low-noise amplifier (LNA) as shown in Fig. 3.11(b) followed by a 4-phase passive mixer. One clock generation circuit is shared among two receiving paths. In the presence of RF input bond wire and parasitic capacitance of on-chip pad, electrostatic discharge (ESD) diodes, and package lead, each IF receiver alone has an input matching of < -13 dB and a double-side band (DSB) noise figure of 2.8 dB at 2.6 GHz RF in simulation.

As discussed in Section III-B, we compensate front-end I-Q mismatch in the IF receiver baseband. As shown in Fig. 3.11(c), we implement a 7-bit vector modulator at each IF receiver I or Q baseband output. The outputs of the vector modulators are added in the current domain for high linearity in the presence of image-band blockers. The vector modulator unit cell transconductance amplifier is similar to that reported in [103]. As illustrated by (3.10), the baseband compensation essentially uses the vector modulators to create a complex adjustment weight that mimics the I-Q mismatch. This resembles a vector-modulator-based self-interference cancellation, and it has been shown that our 7-bit vector modulators together can compensate a wide range of I-Q amplitude and phase mismatches [98].

3.5 Measurement Results

As depicted in Fig. 3.13, the RF front-end mixer and IF receiver 65-nm CMOS chips are assembled using QFN packages and mounted on an FR-4 PCB with the two Qorvo QPQ1285 2.6-GHz BAW filters. A 1:1 balun (Johanson Technology Inc., 4400BL15A0050E) is used to facilitate single-ended measurements and its loss has been de-embedded. Also, the loss of long IF PCB traces between the BAW filter outputs and the IF receiver inputs is de-embedded. Both the RF front-end and the IF receiver chips use 1.2-V supplies. The RF front-end chip has a dc power consumption of 28 to 48 mW with 3.5-to-6.5-GHz RF, and the IF receiver chip draw 62 mW power in the nominal setting.

3.5.1 Fixed LO Small-Signal Measurements

Using an RF and IF LO of 1.04 GHz and 2.6 GHz, respectively, the filtering front-end chipset was first measured operating at 3.64 GHz near the lowest RF. This corresponds to the smallest frequency separation between the signal and its image with the worst-case image filtering as discussed in Section III-C.

The measured and simulated chipset RF input reflection coefficient (S_{11}), noise figure (NF), and conversion gain from RF to receiver baseband are plotted versus input RF in Fig. 3.14 without I-Q mismatch compensation. The measured BAW filter S -parameters are also plotted as a reference.

As can be seen in Fig. 3.14, our receiver chipset conversion gain preserves the sharp frequency selectivity of the IF BAW filter but gets frequency translated to an RF-mixer-LO-defined higher frequency. Besides the IF BAW filter, the receiver chipset pass-band response is affected by the front-end mixer LC impedance shaper and the IF receiver baseband RC filtering. This results in an instantaneous bandwidth of 160-to-170 MHz controlled by the receiver baseband RC setting.

The chipset has measured conversion gain of 20 dB, noise figure of 10 dB, and input S_{11} of < -10 dB. Reasonable matches between simulated and measured gain and S_{11} results are observed. Regarding noise figure, given simulated 5-dB RF passive mixer loss g_1 and 2.8-dB standalone IF receiver noise figure F_{RX} mentioned in Section IV and BAW filter loss g_2 of 3 dB, the calculated chipset noise figure is 8.2 dB based on (3.12). This is lower than the simulated noise figure of 9.5 dB due to the non-ideal impedance matching at various RF and IF interfaces. For example, given an R_{IF} of 68 Ω which corresponds to a -16 -dB S_{11} , the calculated noise figure using (3.12) increases from 8.2 dB to 9.5 dB.

Without I-Q mismatch compensation – in other words, the receiver baseband vector modulator weights M_{ij} and A_{ij} are all set to be zero (see Fig. 3.9), the measured image

rejection ratio is from 18 dB to 21 dB with an average of 19 dB across a 160-MHz signal BW.

Next, we used IF receiver baseband vector modulators to compensate I-Q mismatch for improved image rejection ratio. The measured conversion gain and NF with I-Q mismatch compensation are plotted in Fig. 3.15. As expected, the measured signal-band conversion gain and noise figure are almost identical to those in Fig. 3.14. However, the average image rejection ratio is improved from 19 dB to 42 dB after I-Q mismatch compensation. Because of the frequency selectivity difference between the vector modulators and the I-Q mismatches [see Section III-B and (3.10)], The image rejection experiences a larger variation of 33-to-45 dB, compared to 18-to-21 dB.

Finally, we measured the chipset with a fixed-frequency RF input high-pass filter (Mini-Circuits, VHF-3100+), and the results are shown in Fig. 3.16. This high-pass filter further improves the average image rejection ratio to 81 dB across the 160-MHz bandwidth, while degrading the conversion gain and noise figure by 0.8 dB. As discussed in Section III-C and based on the measured high-pass filter response, this fixed-frequency high-pass filter would provide an additional 32-to-45 dB image rejection across the entire 3.5-to-6.5-GHz RF operation range.

3.5.2 Small-Signal Measurements Across LO Frequencies

The measured chipset conversion gain, noise figure, and input reflection coefficient (S11) across seven different RF LO frequencies (IF receiver LO is fixed at 2.6 GHz) are plotted in Fig. 3.17. For beyond-6-GHz RF, the conversion gain is measured with a noise source, and hence only in-band gain is reported. Across the entire RF range of 3.5-to-6.5 GHz, the chipset has 18-to-20 dB conversion gains, 10-to-12 dB noise figures, and < -6 dB S11. The simulated S11 results are plotted in Fig. 3.17 showing a good match with those in measurements. The S11 is degraded beyond 5-GHz RF due to parasitics associated with the QFN package, bond wire, as well as on-chip pads and ESD diodes.

3.5.3 Large-Signal Measurements

The measured mixer-first acoustic-filtering chipset in-band linearity results are shown in Fig. 3.18 with RF at 3.5 GHz. The measured output-referred in-band 1-dB compression point (P-1dB) is -4 dBm while the in-band output-referred IP3 is $+10$ dBm. The in-band linearity is dominated by the IF receiver baseband vector modulators.

The measurement setups for out-of-band linearity measurements and their results are shown in Fig. 3.19. The measured blocker-induced 1-dB compression point (B-1dB) and IIP3 at $1\times$ RF bandwidth offset are $+5$ dBm and $+27$ dBm, respectively. This high-linearity at

this close-in frequency offset is achieved through the sharp filtering from the IF BAW filters. As the out-of-band blocker frequency offset increases, the B-1dB and IIP3 saturate to about +9 dBm and +30 dBm, respectively, and they are limited by the RF mixer switches.

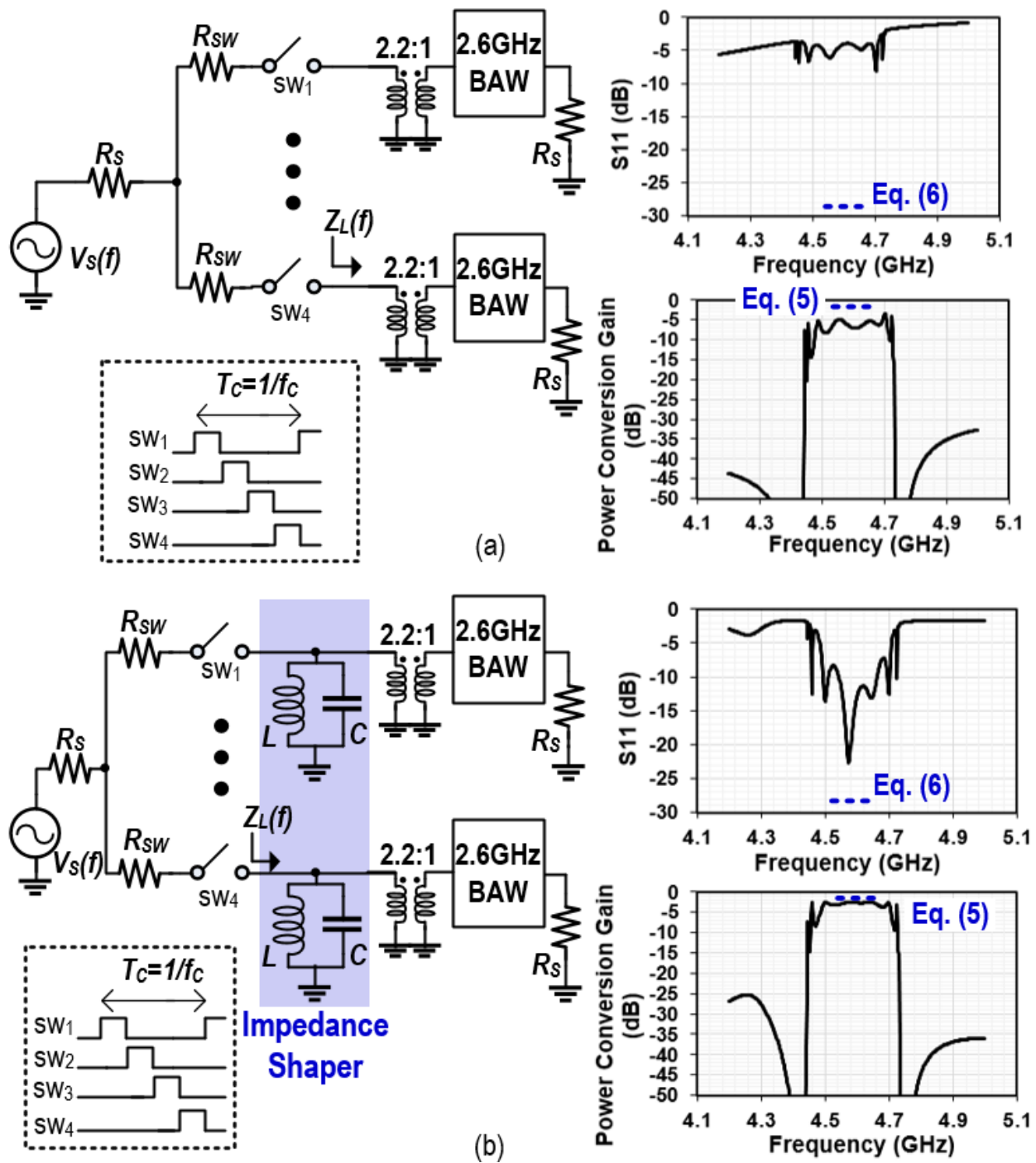


Figure 3.4: Switched-BAW-filters circuits and simulation results: (a) without and (b) with LC impedance shaper. ($R_s = 50$ ohm, $R_{SW} = 5$ ohm, $f_c = 2$ GHz, $f_o = 1/(2\pi\sqrt{LC}) = 2.6$ GHz, and $R_L LC$ tank Q of 10.)

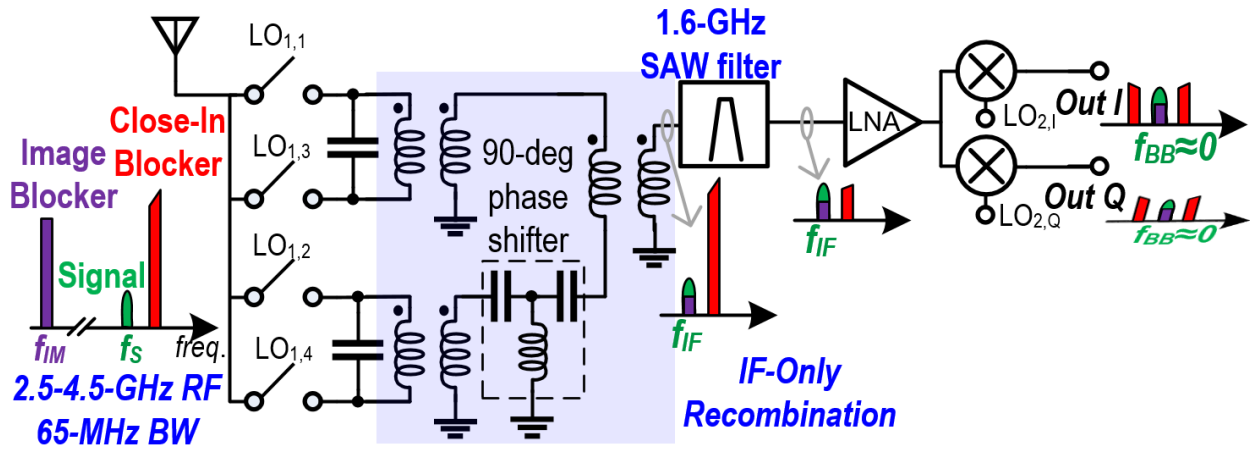


Figure 3.5: Mixer-first acoustic-filtering front-end using all-passive IF-only recombination in [32], [33].

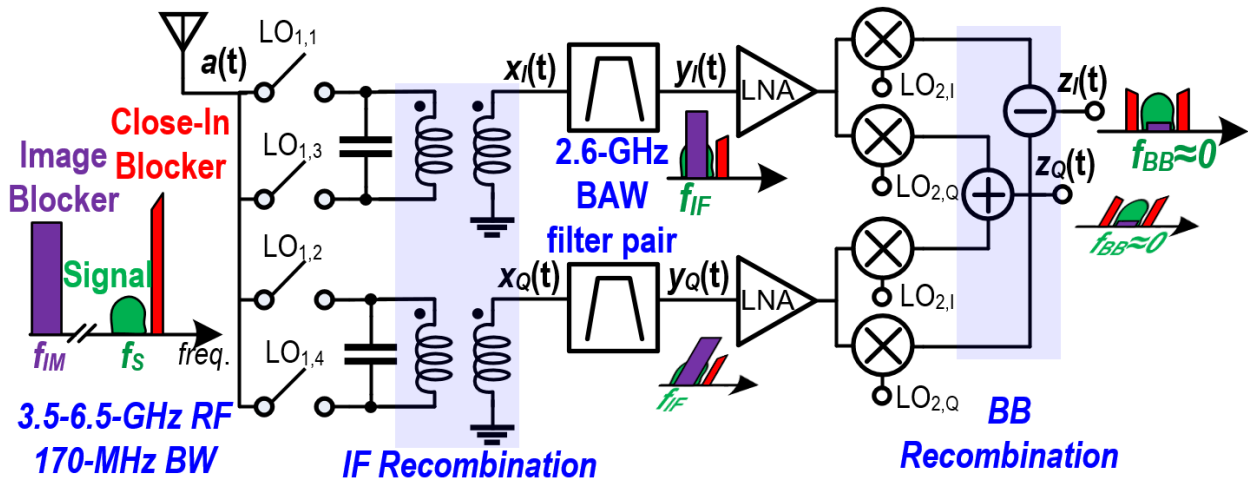


Figure 3.6: Proposed Mixer-first acoustic-filtering chipset using IF-and-baseband mixed-domain recombination. When compared to an IF-only recombination architecture, it has a higher RF, wider instantaneous bandwidth, and eliminates several bulky, lossy, and narrow-band IF components.

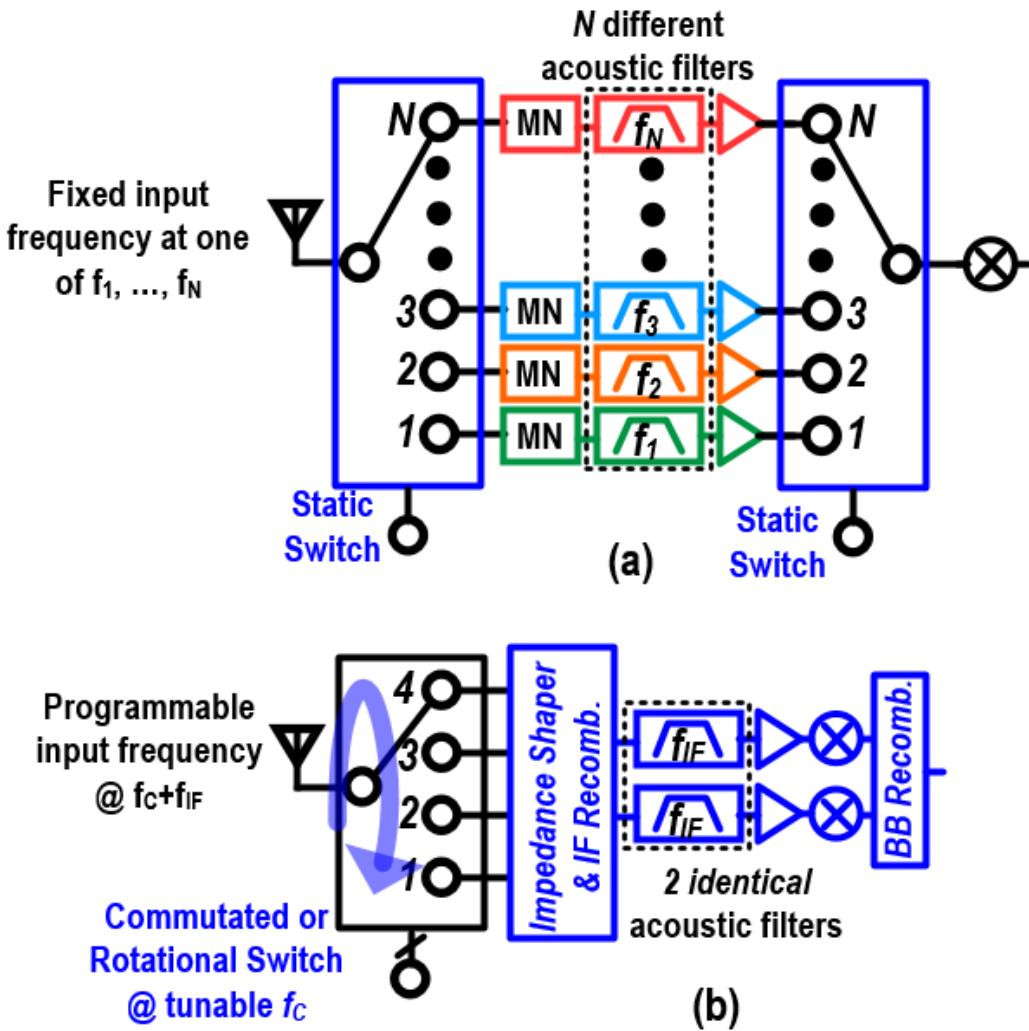


Figure 3.7: Conceptual comparison between (a) filter-bank-based multi-band front-end design and (b) our proposed mixer-first acoustic-filtering front-end.

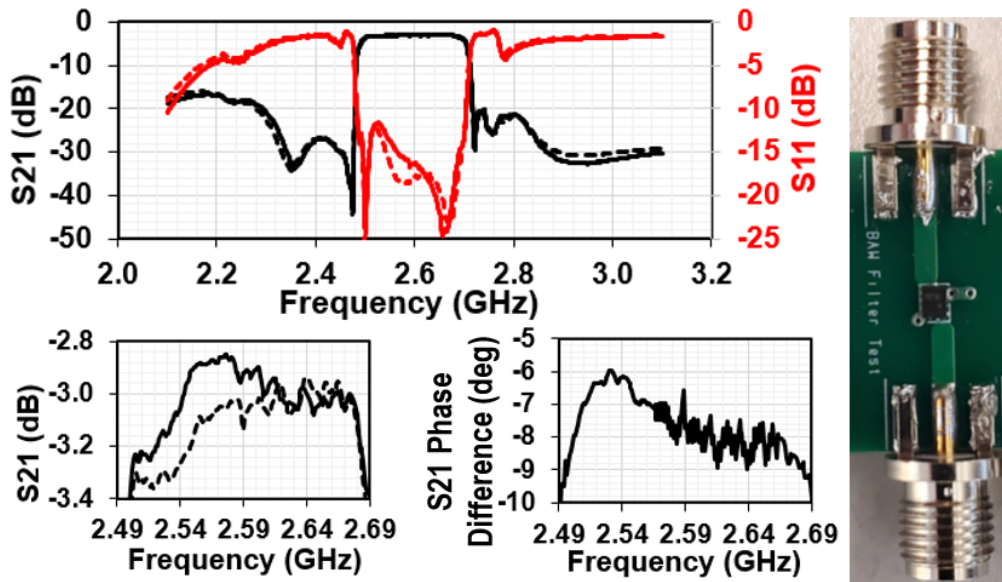


Figure 3.8: Measured S-parameters of two Qorvo QPQ1285 BAW filters (filter 1: solid line, filter 2: dashed line) and the gain and phase mismatches.

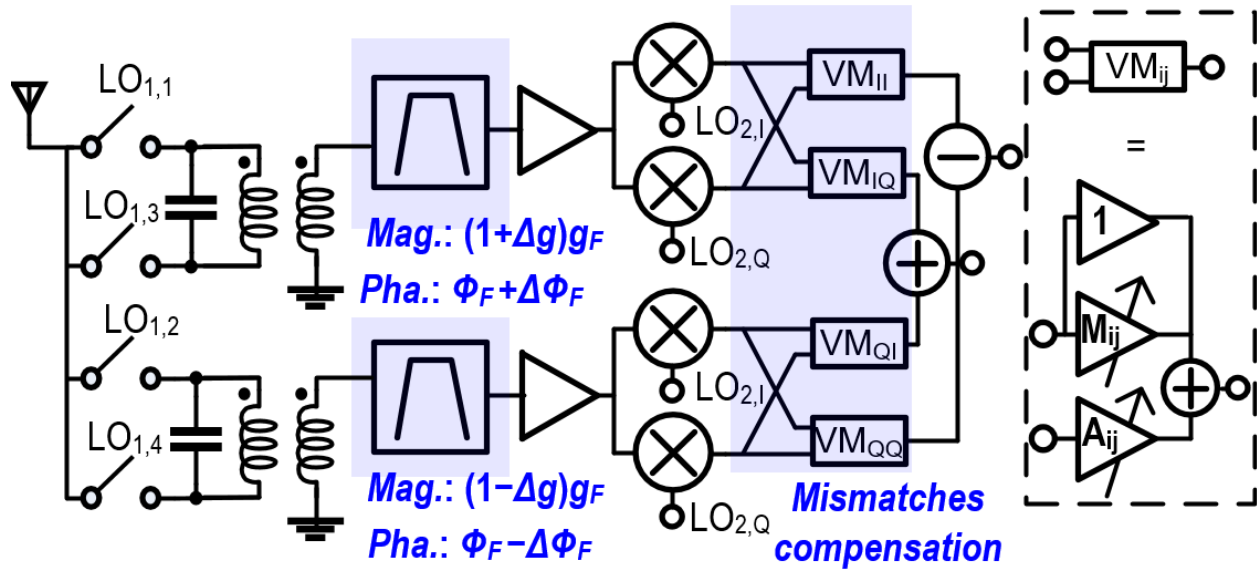


Figure 3.9: Mixer-first gigahertz-IF acoustic-filtering chipset with I-Q mismatch compensation at baseband.

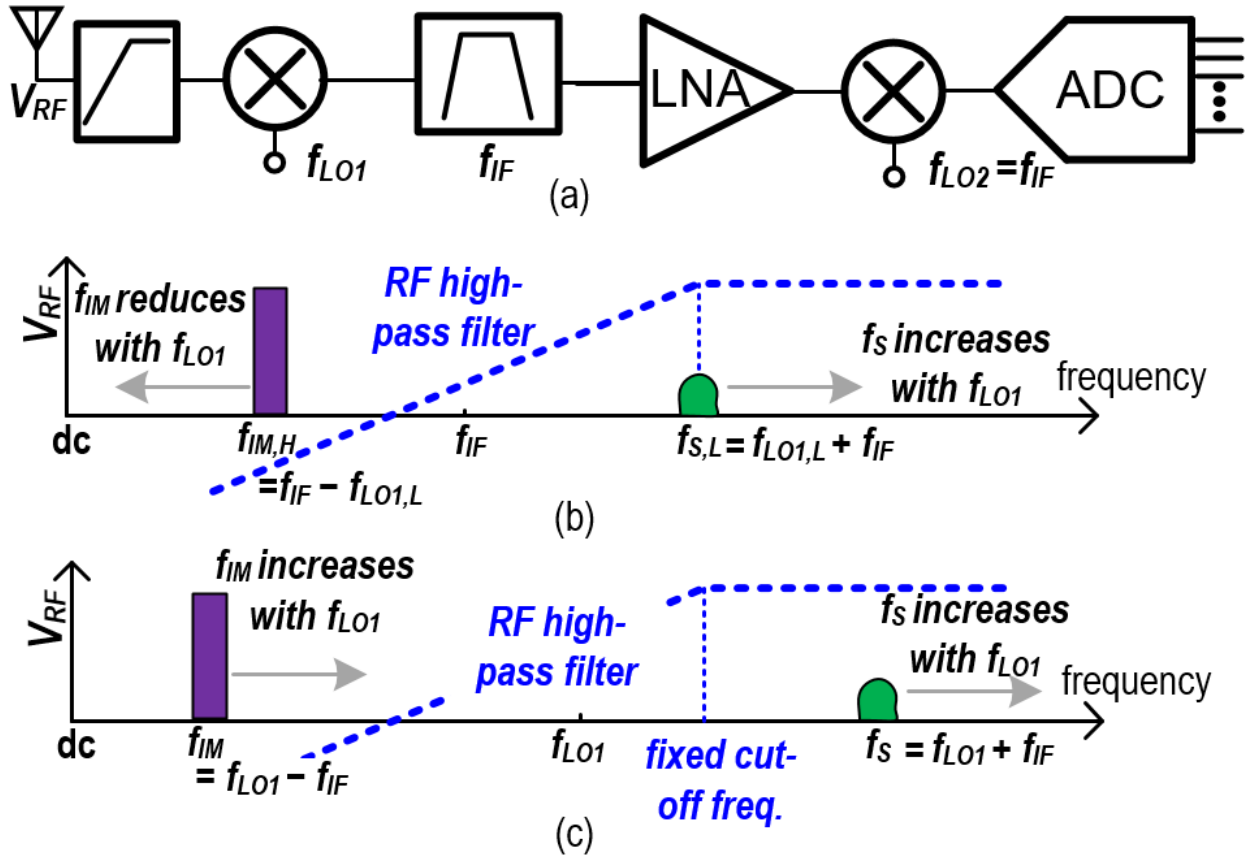


Figure 3.10: Image filtering with a fixed-frequency RF high-pass filter: (a) front-end block diagram; RF input spectrum when (b) $f_{LO1} < f_{IF}$ and (c) $f_{LO1} \geq f_{IF}$.

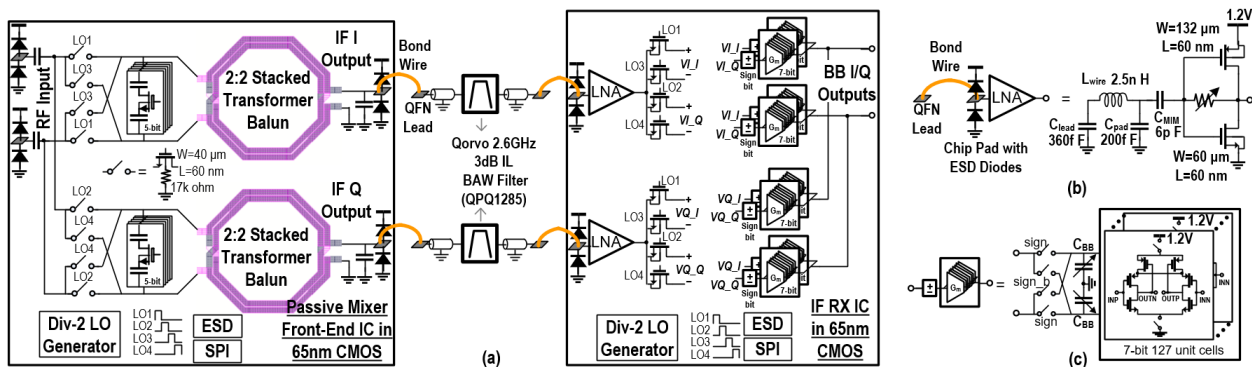


Figure 3.11: A proof-of-concept prototype of the proposed mixer-first acoustic-filtering chipset with mixed-domain recombination: (a) block diagram and top schematic; (b)(c) schematics of IF receiver LNA and baseband amplifier.

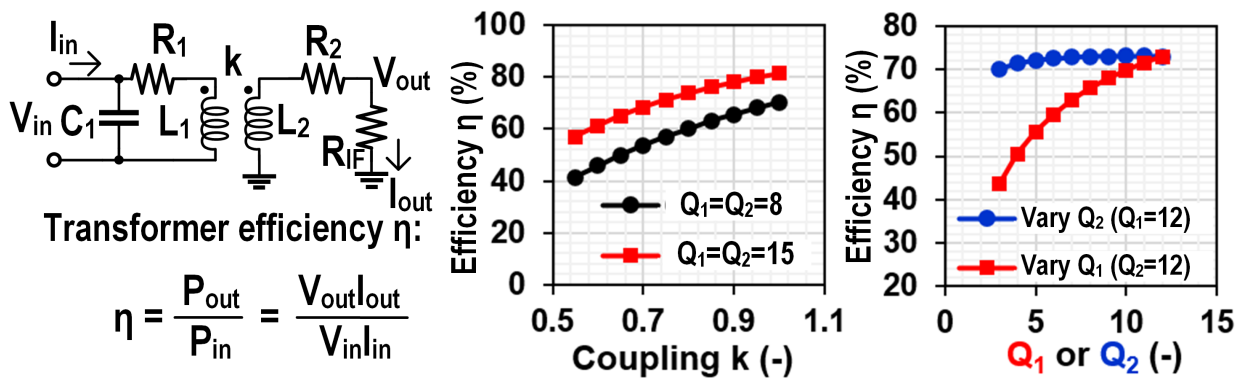


Figure 3.12: IF transformer balun efficiency is asymmetrical between the primary and secondary winding Q factors, and the efficiency is mostly determined by the primary quality factor. ($L_1=L_2=2$ nH, $R_{IF}=100$ Ω , $f_{IF}=2.6$ GHz).

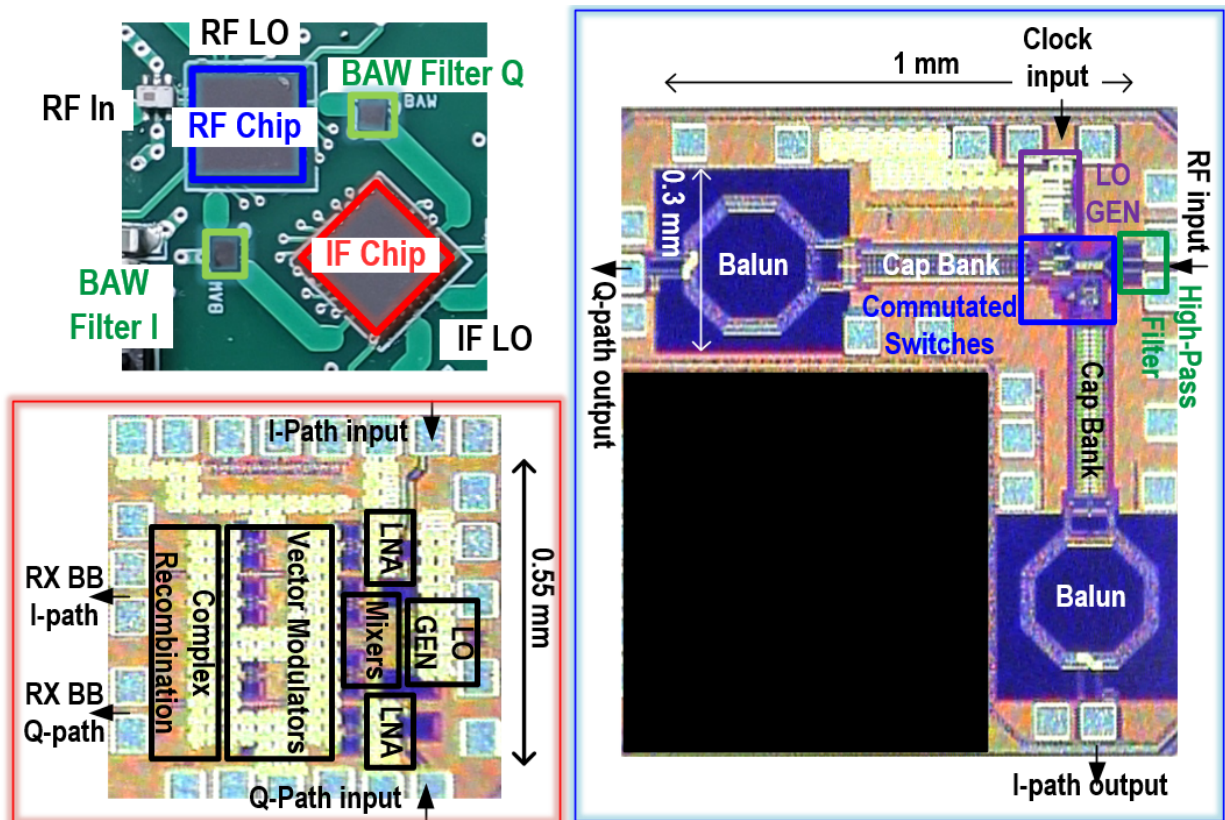


Figure 3.13: Our mixer-first acoustic-filtering proof-of-concept chipset on an FR-4 PCB with CMOS dies microphotograph.

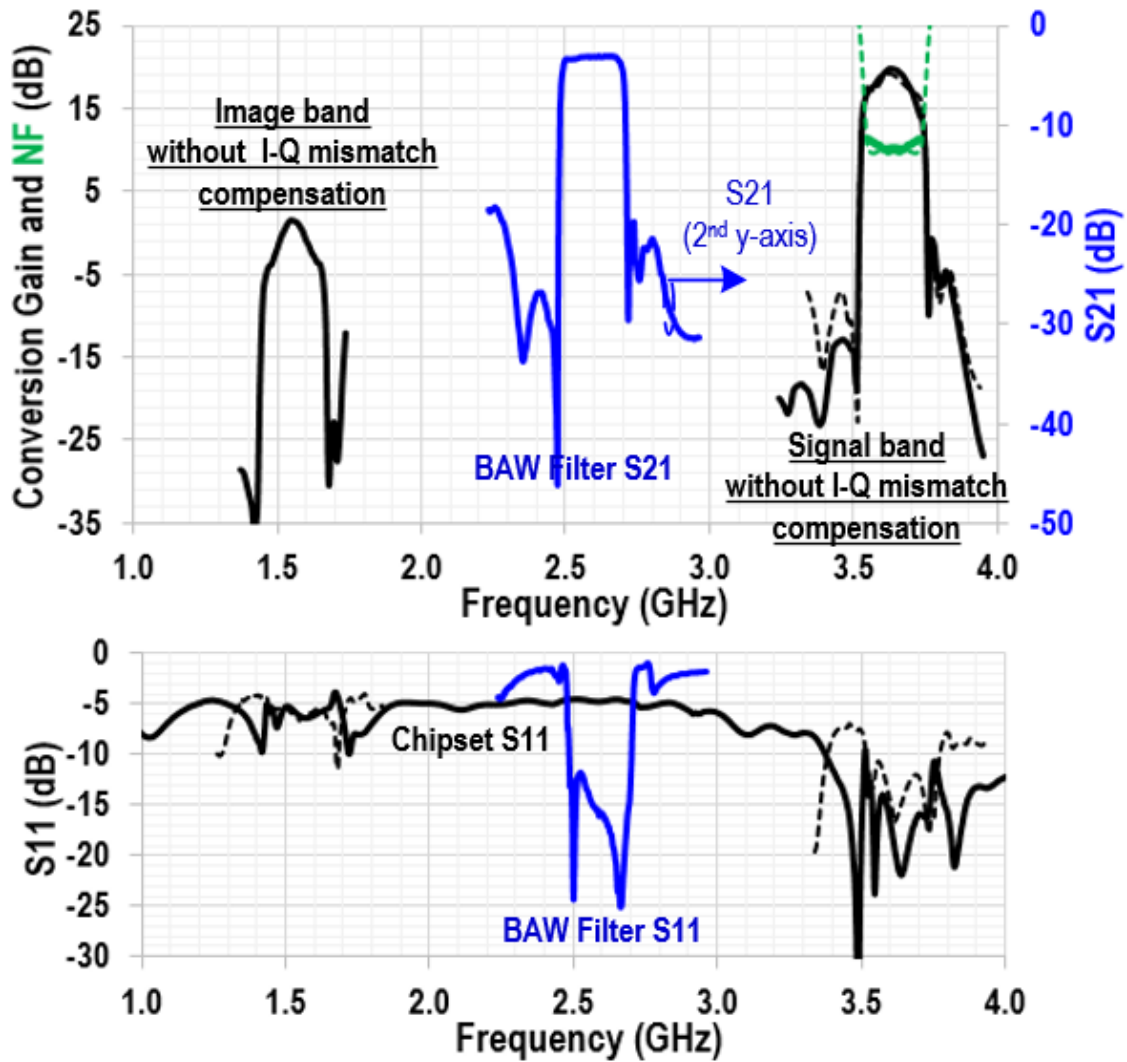


Figure 3.14: Measured (solid lines) and simulated (dashed lines) chipset RF input reflection coefficient (S11), noise figure (NF), and conversion gain from RF to receiver baseband without I-Q mismatch compensation. The measured BAW filter S -parameters are also plotted in blue as a reference.

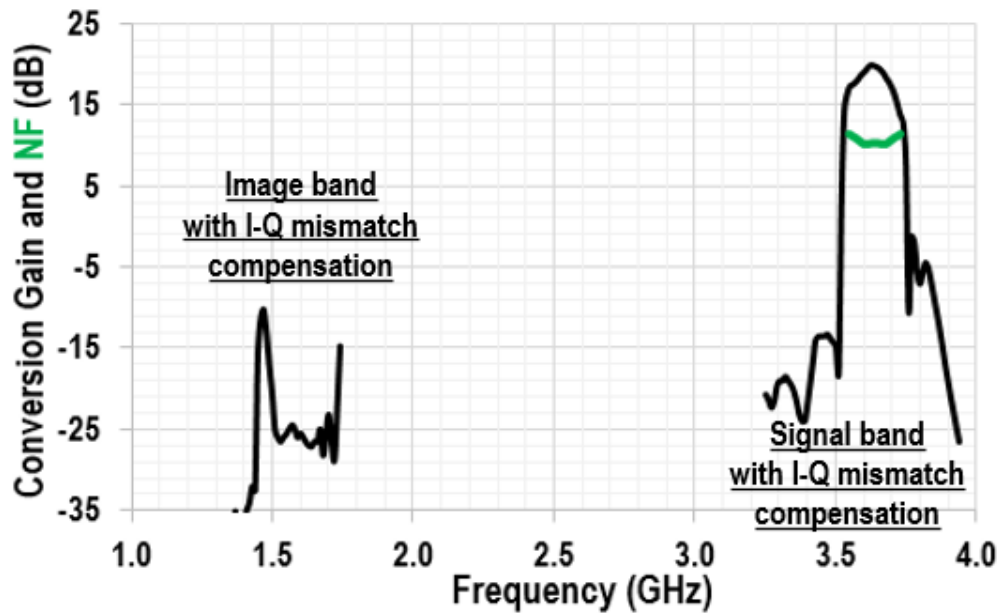


Figure 3.15: Measured chipset noise figure and conversion gain with I-Q mismatch compensation via adjusting receiver baseband vector modulators, improving the average image rejection ratio to 42 dB from 19 dB in Fig. 3.14.

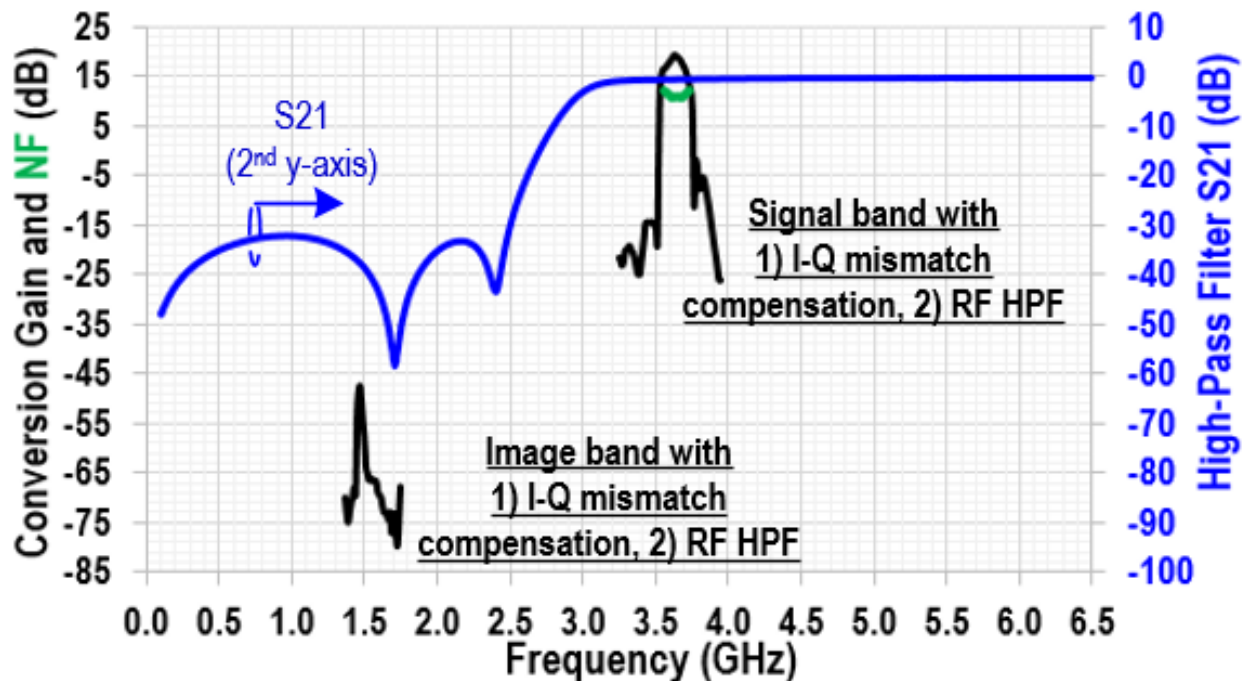


Figure 3.16: Measured chipset noise figure and conversion gain with I-Q mismatch compensation and a fixed-frequency RF input high-pass filter (Mini-Circuits, VHF-3100+). This high-pass filter further improves the average image rejection ratio to 81 dB across the 160-MHz bandwidth, while degrading the conversion gain and noise figure by 0.8 dB.

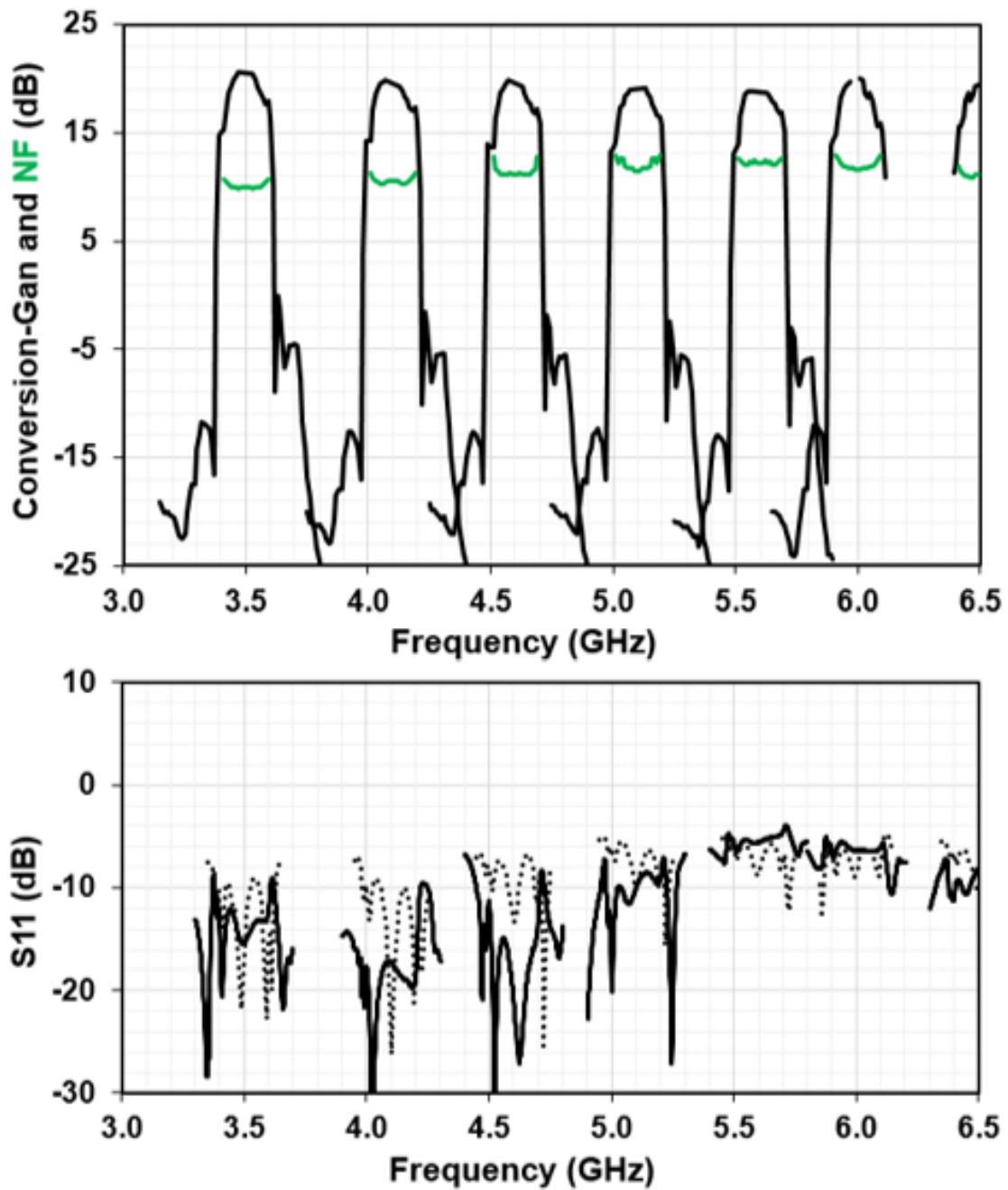


Figure 3.17: Measured chipset RF input reflection coefficient, noise figure, and conversion gain across seven different RF LO frequencies (IF receiver LO is fixed at 2.6 GHz). The simulated input S11 is plotted in dashed lines.

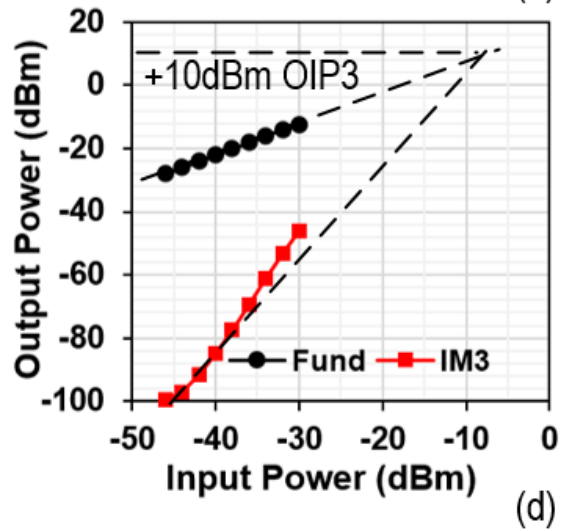
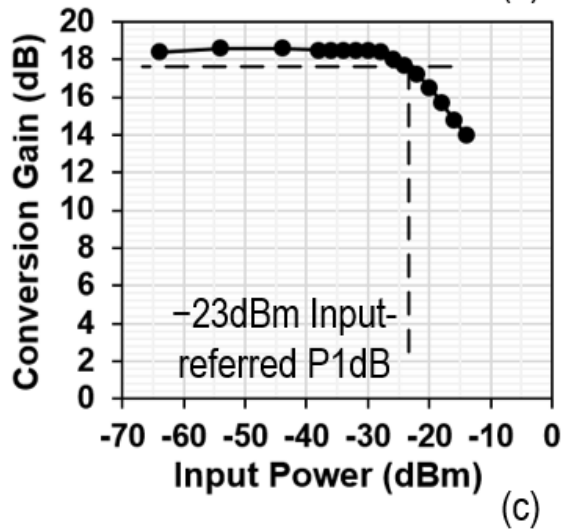
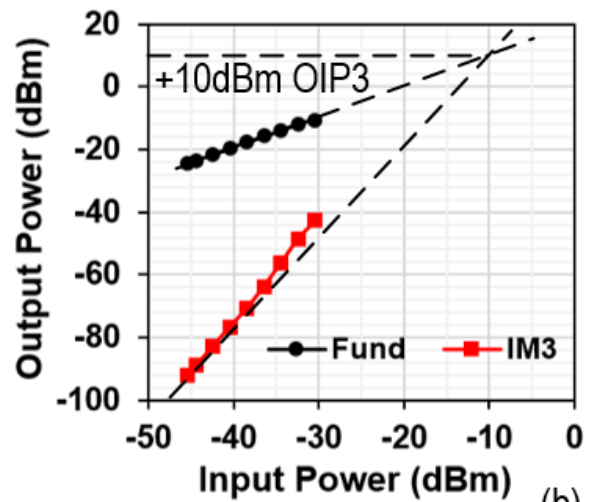
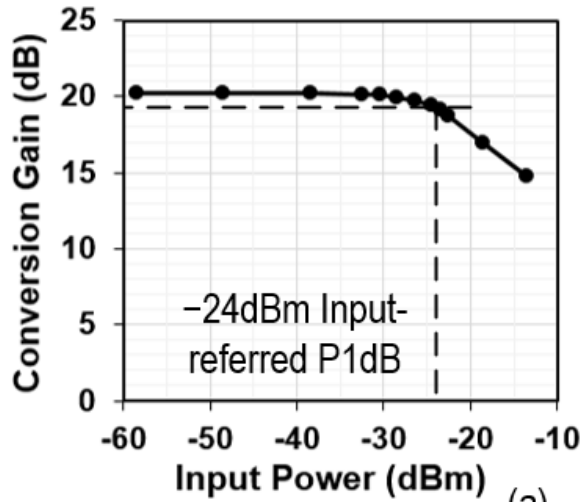


Figure 3.18: In-band linearity measurement results: (a) gain compression P-1dB, and (b) IP3.

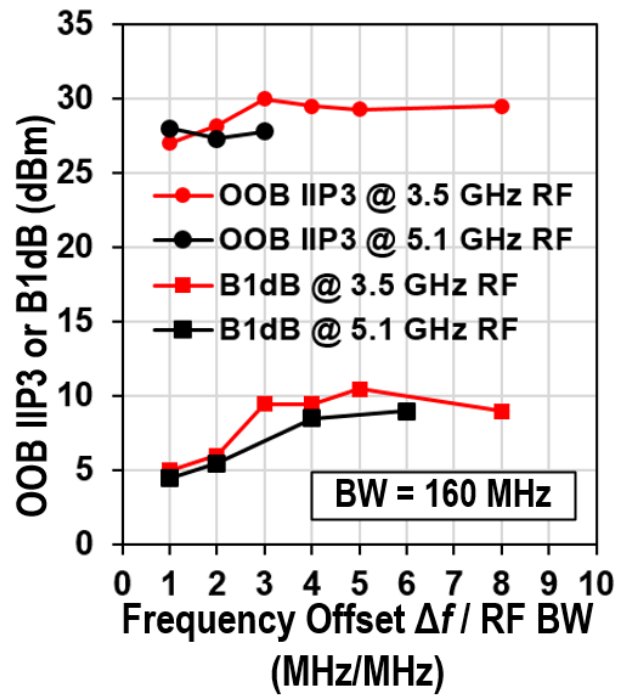
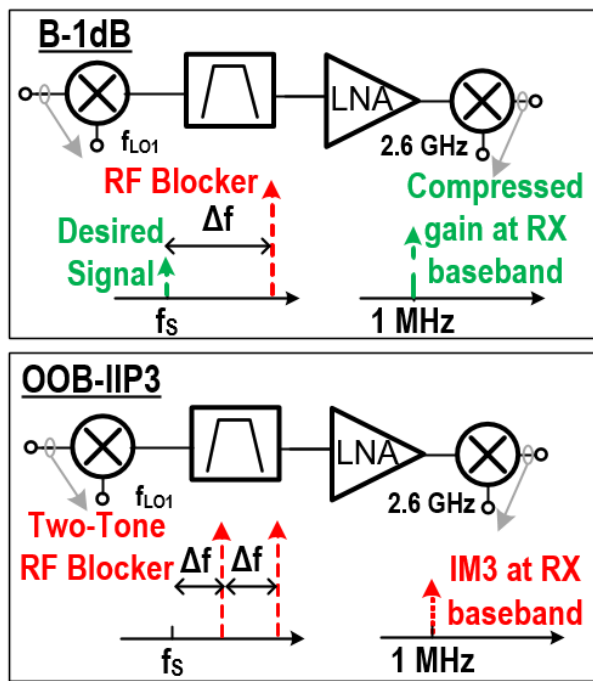


Figure 3.19: Out-of-band linearity measurement setups and results.

Table 3.1: Measurement summary and comparison with state-of-the-art works.

	RFIC 2018 [8]	JSSC 2018 [9]	JSSC 2020 [5]	JSSC 2020 [6]	JSSC 2019 [2]	ISSCC 2013 [36]	IMS 2017 [11]	JSSC 2021 [14]	This work
RF Range (GHz)	7	0.2 to 8.0	0.2 to 2	0.5 to 2	0.8 to 1.1	1.96	3 to 9	2.5 to 4.5	3.5 to 6.5
IF (MHz)	0	0	0	0	N/A	30	10250	1600	2600
3dB RF BW (MHz)	80	20	18	260	30 to 50	5	100	65	160 to 170
NF Filter Only	N/A	N/A	N/A	N/A	5.0 to 8.6	N/A	5 to 6	5.5 to 7.1	N/A
(dB) Filter & Rx	10 to 12	3.5 to 7.1	4.3 to 7.6	5.5	8.0 to 11.6#	4.5	8 to 9#	8.5 to 10.1#	10 to 12
Gain (dB)	10 to 24	21	13	32.4	-4.6 to -3.8	45	-5	-6.4 to -5.4	18 to 20
In-Band IIP3	0 to +5 dBm	+3 dBm	+1 dBm	-12 dBm	+25 dBm	-15 dBm	N/R	+20.3 dBm	-10 dBm
Rejection @ 1×BW _{RF}	10 to 15 dB	15 to 20 dB	14 dB	25 dB	10 to 15 dB	N/A	35 to 40 dB	45 to 55 dB	30 to 45 dB
OOB-IIP3 @ 1×BW _{RF}	+21 dBm	+16 dBm	+15 dBm	+16 dBm	+24 dBm	0 dBm	N/R	+29.4 dBm	+27 dBm
B-1dB @ 1×BW _{RF}	+2 dBm	0 dBm	-3 to +5 dBm	-4.4 dBm	+9 dBm	-20 dBm	N/R	+4.3 dBm	+5 dBm
Supply Voltage (V)	2.5, 4, 4.5	1.2	1.2	1.2, 1.8	-1, 1.2, 2	1.45, 1.8	N/R	1.2	1.2
Power (mW)	1466 + 656 (RF + BE)	56 to 290	147 to 179	26 to 37	80 to 97 (Filter only)	155	N/R	12 to 26 (Filter only)	28 to 48 + 62 (Filter + RX)
Integrated Circuits Technology	130-nm BiCMOS	45nm CMOS	28nm CMOS	28nm CMOS	65nm CMOS	65nm CMOS	0.2μm GaN HEMT	65nm CMOS	65nm CMOS
Chip Area (mm ²)	3.4 + 5 (RF + BB)	0.8	0.48	0.16	1.9 (Filter only)	1	3.75 (Filter only)	1.4 (Filter only)	0.5 + 0.35 (Filter + RX)
Off-Chip Component	none	RF balun	none	RF balun	RF balun	RF balun	Two isolators, hybrid coupler, and cavity filter	RF and IF baluns, IF inductor, SAW filters	RF balun, BAW filters

To facilitate comparison between the filter-only and the filtering receiver (RX) FE works, we have assumed a 3-dB-NF IF receiver for each filter-only work.

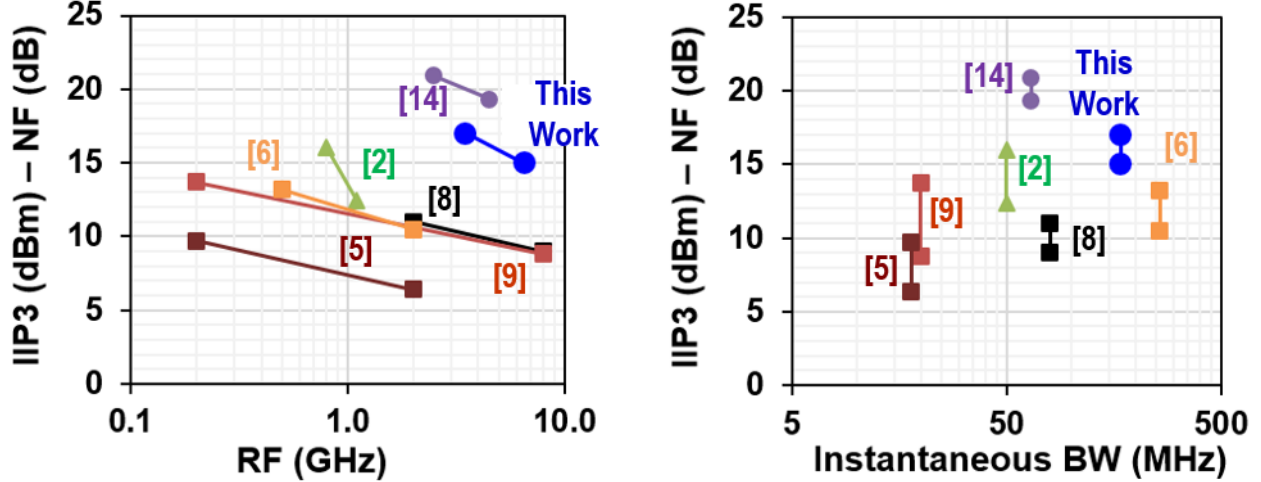


Figure 3.20: Normalized linearity-noise performances of recent state-of-the-art high-linearity receivers and filters versus RF and instantaneous bandwidth. (Squares: direction-conversion/low-IF mixer-first receivers; triangles: high-order N -path filters; circles: superheterodyne high-IF mixer-first front-ends.)

3.5.4 Summary and Comparison

A measurement summary and comparison with recent state-of-the-art works is given in Table 3.1. This work achieves +27 dBm out-of-band IIP_3 and >30 dB rejection at $1 \times BW$ offset. This is a 6-to-11-dB improvement in out-of-band IIP_3 at $1 \times BW$ offset compared to state-of-the-art monolithic mixer-first direct-conversion or low-IF receivers in [38]–[41], [54]. While the N -path filter in [36] has similar linearity performance, this work operates at $5 \times$ higher frequencies with $2 \times$ wider tuning range and >15 dB higher OOB rejection. Compared to the mixer-first acoustic-filtering FE in [32], [33], this work achieves $2.6 \times$ wider BW, operates at $1.4 \times$ higher RF, eliminates off-chip IF balun and inductor, while having comparable NF and linearity.

Normalized linearity-and-noise performance, calculated as $\frac{IIP_3}{NF \cdot P_{DC}}$, of recent state-of-the-art high-linearity receivers and filters versus RF and instantaneous bandwidth is depicted in Fig. 3.20, where IIP_3 at $1 \times BW$ offset is used. For a fair comparison, we have added a 3-dB-NF 20-mW- P_{DC} receiver to front-only works. As can be seen in Fig. 3.20, this work achieves favorable normalized linearity-and-noise performance while operating above 3.5 GHz RF and supporting a >160-MHz instantaneous bandwidth.

3.6 Conclusion

We have demonstrated a reconfigure wireless receiver front-end with a widely tunable RF from 3.5 to 6.5 GHz for future wireless communications and sensing applications. By

fusing commutated- LC passive mixer and acoustic filter technologies in a new mixed-domain recombination architecture, the front-end is capable of achieving very high linearity, especially at close-in frequency offset, with a wide 160-MHz instantaneous bandwidth and zero off-chip IF components except acoustic filters.

Chapter 4

Rotational Motion for Angular Aliasing and Source Enhancement

**

4.1 Introduction

As speech recognition and conversational AI matures, voice interactions with robots will become even more popular [105]. Robots in homes, hospitals, restaurants, and airports will interface with humans, with speech serving as the primary medium of interaction [106], [107]. In such scenarios, separating a user’s voice will be essential, especially when these interactions occur in noisy environments. In signal processing, this problem is called “source separation,” and has been studied extensively (e.g. ICA, IVA, Adaptive Beamforming) [108]–[115]; today’s results are impressive, to the extent that K source signals can be separated using M microphones, even when K is slightly larger than M [116]–[120]. Observe that this $K > M$ problem is particularly challenging not only because the K signals are unknown, but because the K channels (over which the signals arrive to the microphones) are unknown as well. Hence, this problem is specifically known as *under-determined blind source separation* (UBSS).

A rich body of work has concentrated on UBSS, and state of the art (SOTA) algorithms range from unsupervised methods (e.g., Nonlinear beamformers, Kernels) and speech specific techniques (e.g., DUET, Bayesian-DUET), to compressed sensing and supervised deep learning approaches [116], [118], [120]–[123]. However, majority of past work must rely on interpolations and regressions since some source information is lost in the (under-determined)

**This chapter is partially adopted from author’s own work [104]

mixing process. Therefore, performance degrades, understandably, as K increases for a fixed M . Said differently, any reduction in the $(K - M)$ gap can directly improve the quality of source separation.

This paper proposes to leverage robotic rotation to reduce the $(K - M)$ gap. The core idea is simple. Observe that signals arriving from different angles θ_i produce relative delays δ_i at the microphone array. Rotation of the array causes these relative delays to change non-linearly, offering the opportunity to “move” the sources in this relative-delay space. When the microphone rotates to bisect two sources — such as in Fig. 4.1 where the line joining the microphones bisects the sources A and B — the relative delays of the bisected sources become identical. Hence, in the relative-delay space, K sources manifest as $(K - 1)$ sources. This implies that the scenario in Fig. 4.1, which was originally an under-determined $[K=3, M=2]$ system, has now become determined with $[K=2, M=2]$. Even when $K > M + 1$, the reduction from K to $(K - 1)$ offers concrete improvements, both in source separation and localization.

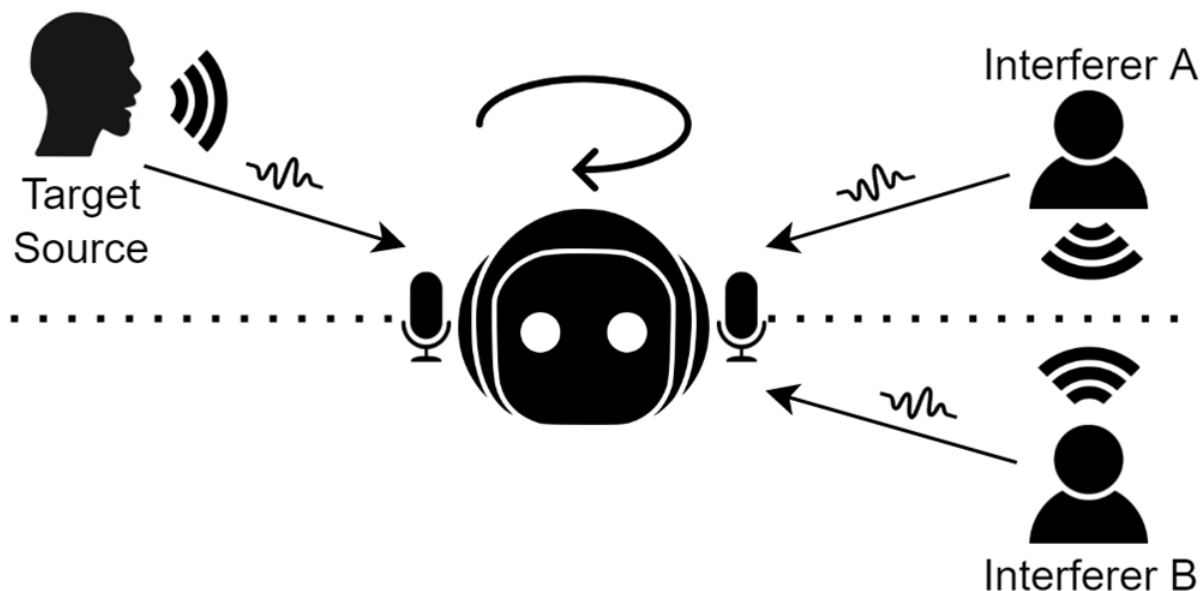


Figure 4.1: Rotation of the microphone array to the correct orientation (that bisects the sources A and B) produces a desired “aliasing” in relative delay.

Realizing the above idea presents 2 challenges:

1. Since the angle of arrivals (AoA) of the K signals are not known, the correct microphone orientation θ^* is unknown as well. Estimating all K AoAs is difficult with $M(< K)$ microphones [124]–[128], and worse, AoA estimates are plagued by front-back ambiguities

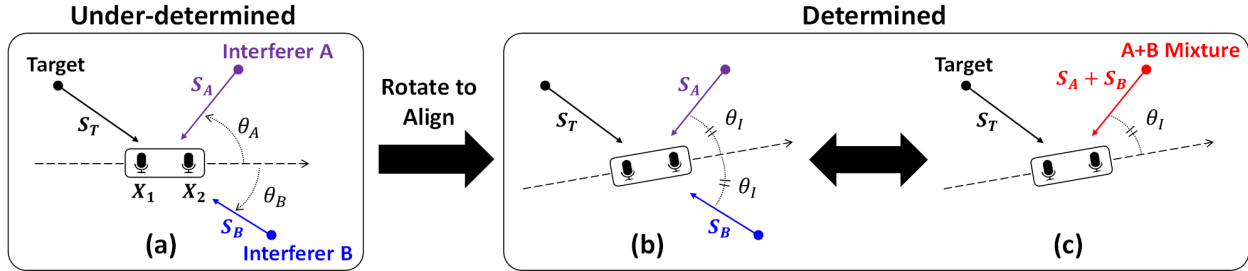


Figure 4.2: (a) 2-microphone array faced with 3 sources resulting in a UBSS problem. (b) Rotation causes interferers to arrive over the same absolute AoA angle (θ_I and $-\theta_I$). (c) The steering vector for interferers get aliased (or aligned), resulting in a determined system.

(i.e., it is difficult to tell whether a signal is arriving from a direction θ in front, or $-\theta$ from the back).

2. Even if the K AoAs are estimated, it is not clear which interferers should be bisected to maximize performance. There are $\binom{K-1}{2}$ candidate pairs to bisect, and not all of them help equally in separating the given target signal.

This paper addresses these two problems in Section 4.3 through a mobility-guided algorithm that first estimates the source AoAs and, based on the AoAs, decides on the optimal microphone orientation. Once rotated to this orientation, the recorded signal is fed to a source separation (SS) algorithm. Our proposed RoSS module is complementary, hence compatible, with most SS algorithms.

We implement RoSS on a rotating microphone prototype, and perform experiments in simulated and uncontrolled (indoor/outdoor) environments (Section 4.4). Results[†] show that RoSS achieve around 10-to-15dB of scale-invariant signal distortion ratio (SI-SDR)[129], consistently outperforming existing UBSS/BSS methods by upto 6dB in various scenarios. We believe RoSS could also be effective with smartphones, earbuds, moving video-conference systems, and surveillance cameras, all of which have limited number of microphones but contain actuators or inertial measurement units (IMUs) for angular rotation and sensing.

4.2 Formulation and Opportunity

4.2.1 Signal Model

Let $S_T(t)$, $S_A(t)$, $S_B(t)$ be 3 source signals, of which S_T is the target and others are interference (Fig. 4.2(a)). A linear 2-microphone array receives the mixture of these signals as $X_1(t)$ and

[†]More results and demos : <https://uiuc-ss.github.io/RoSS>

$X_2(t)$ and we designate $X_1(t)$ as the reference for relative delay calculations. The signals travel from the far-field over AoAs θ_k ($k=T,A,B$). We explain our proposed method with $K = 3$ signals and consider $K > 3$ later.

We make the following Assumptions:

- (A1) The sound sources are human speech, widely assumed to be mutually independent, non-Gaussian signals.
- (A2) Once a speech has been separated, it is possible to tell if it is from the target user (i.e., a voice fingerprint is available).
- (A3) Sources are not moving in the time scale of seconds.

Thus, the received (convolutive) signal mixture is:

$$X_1(t) = \sum_{k=A,B,T} S_k(t), \quad X_2(t) = \sum_{k=A,B,T} S_k(t + \tau_k) \quad (4.1)$$

where $\tau_k = \frac{d}{v_p} \cos(\theta_k)$, ($k=T,A,B$), are time-difference-of-arrivals (TDOA) between the microphones (also called relative delay), while v_p and d denote velocity-of-sound and distance-between-microphones, respectively.

Thus, in the time-frequency domain(time index omitted):

$$\vec{X}(f) = \vec{a}_T(f)S_T(f) + \vec{a}_A(f)S_A(f) + \vec{a}_B(f)S_B(f) \quad (4.2)$$

which in the matrix form can be written as:

$$\begin{bmatrix} X_1(f) \\ X_2(f) \end{bmatrix} = \begin{bmatrix} | & | & | \\ \vec{a}_T & \vec{a}_A & \vec{a}_B \\ | & | & | \end{bmatrix} \begin{bmatrix} S_T(f) \\ S_A(f) \\ S_B(f) \end{bmatrix} \quad (4.3)$$

Here $\vec{a}_k = [1 \exp(j2\pi f\tau_k)]^T$ ($k=A,B,T$) is the steering vector. Note that even if all \vec{a}_k 's are known, the system is still under-determined.

4.2.2 Interference Alignment

What if we rotate the array such that the line joining the microphones bisect the two interferers? While the correct rotation angle needs to be inferred blindly, for now let us assume we know it. Fig.4.2(b) shows the outcome. *Since the new AoAs of the two interferers*

are now θ_I and $-\theta_I$, their corresponding TDOAs become equal, or aliased, as follows:

$$\tau'_A = \frac{d}{v_p} \cos(\theta_I) = \frac{d}{v_p} \cos(-\theta_I) = \tau'_B$$

Thus, in frequency domain, interferers A and B have identical array vectors $\vec{a}_I(f) = [1 \exp(j2\pi f\tau_I)]^T$ where $\tau_I = \tau'_A = \tau'_B$. Hence, the new measurement vector $\vec{X}'(f)$ is:

$$\begin{bmatrix} X'_1(f) \\ X'_2(f) \end{bmatrix} = \begin{bmatrix} | & | \\ \vec{a}_T & \vec{a}_I \\ | & | \end{bmatrix} \begin{bmatrix} S_T(f) \\ S_A(f) + S_B(f) \end{bmatrix} \quad (4.4)$$

This expression means that the array *would sense two groups of signals, not three*; one is the target and the other is the sum of two interferers. Fig. 4.2(c) shows these two signals arriving from distinct angles. This produces a determined system of equations except that one of the mixed signals arriving from AoA \vec{a}_I is actually a sum of independent sources. If this sum ($S_A(f) + S_B(f)$) remains independent of the target signal $S_T(f)$ (as shown next), we can apply classical source separation.

4.2.3 Sum of Mutually Independence Sources

We briefly show that a mixture of two independent sources remains independent from the third source when all three are mutually independent. Define A , B and T as mutually independent continuous random variables, and $J = A + B$ is a fourth random variable. Let $F_i(\cdot)$ and $f_i(\cdot)$ be CDF and PDF of variable i , respectively. Then, the joint distribution of T and J can be written as:

$$\begin{aligned} F_{JT}(j, t) &= P(A + B \leq j, T \leq t) \\ &= \int P(A + B \leq j, T \leq t | A = a) f_A(a) da \\ &= \int P(B \leq j - a, T \leq t) f_A(a) da \\ &= \int P(B \leq j - a) f_A(a) da \cdot P(T \leq t) \\ &= P(A + B \leq j) \cdot P(T \leq t) = F_J(j) F_T(t) \end{aligned} \quad (4.5)$$

Therefore, J and T are also mutually independent [130].

4.3 RoSS: AoA Estimation and Optimal Bisection

Our end-goal now is to rotate the microphone so that the correct interferer-pair gets aligned. For this, we first need to estimate all the AoAs, and using the AoAs, determine the optimal interferer-pair that must be bisected.

4.3.1 Estimating AoAs in Under-determined Scenarios

Estimating K AoAs with $M < K$ microphones is known to be a hard problem for general signals. However, literature has shown promise with speech signals, due to what is known as the *W-Disjoint Orthogonality* (WDO) property [116]. Briefly, extensive experiments have shown that speech from two humans have a low probability of collision in a given time-frequency (TF) bin. Thus, if one calculates the TDOA for each TF bin — called *inter-microphone time difference* (ITD) — one can extract information about AoAs. Fig. 4.3 illustrates this with a toy example of red and blue signals; the calculated ITDs from the red and blue TF bins form 2 clusters. The means of these clusters partly reveals the red/blue signal’s AoA.

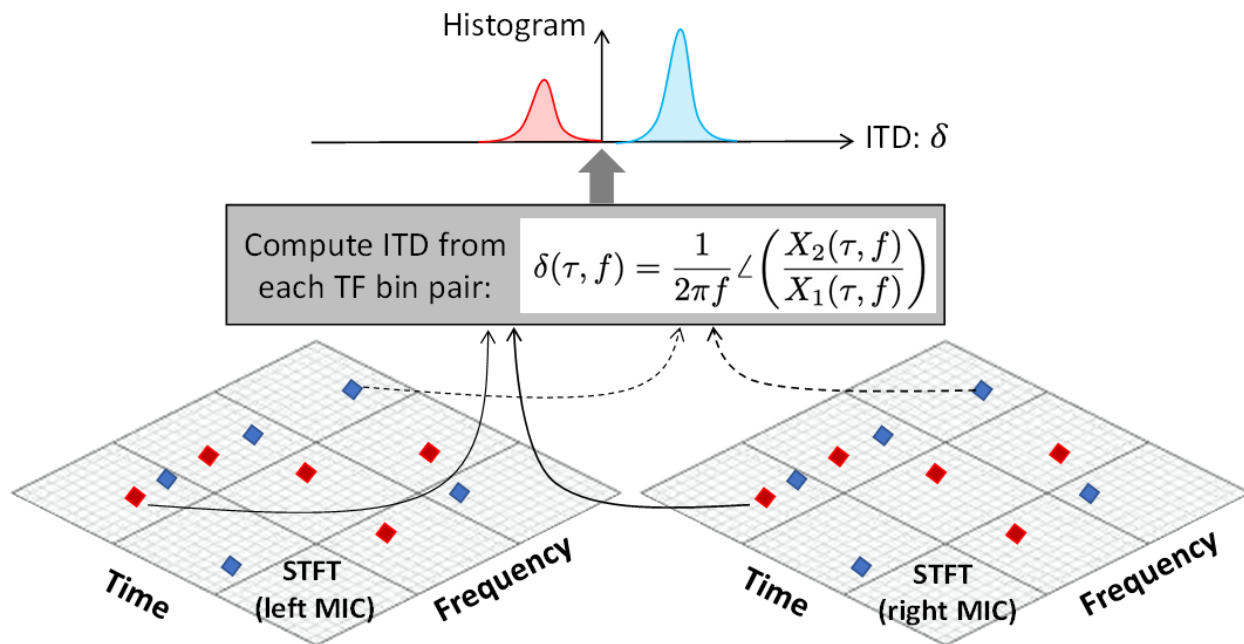


Figure 4.3: ITD computed from TF bins produce 2 clusters around two mean ITDs. These mean ITDs are estimates of AoA.

Unfortunately, the mapping between ITD and AoA is not 1:1 because AoAs of both θ and $-\theta$ produce identical ITDs at the microphone array. Said differently, ITD is calculated

as $\delta_k = \frac{d}{v_p} \cos(\theta_k)$ and both θ_k or $-\theta_k$ produce the same ITD. Fig. 4.4 shows how 2 ITD clusters map to 4 candidate AoAs (of which 2 AoAs are spurious). This is classically known as the *front back ambiguity*. Worse, if the true AoA's happen to be $\theta_1 = -\theta_2$, then it becomes difficult to even recognize the presence of 2 signals. Rotating the microphone array to the correct orientation θ_{final}^* would obviously require to resolve this ambiguity problem first.

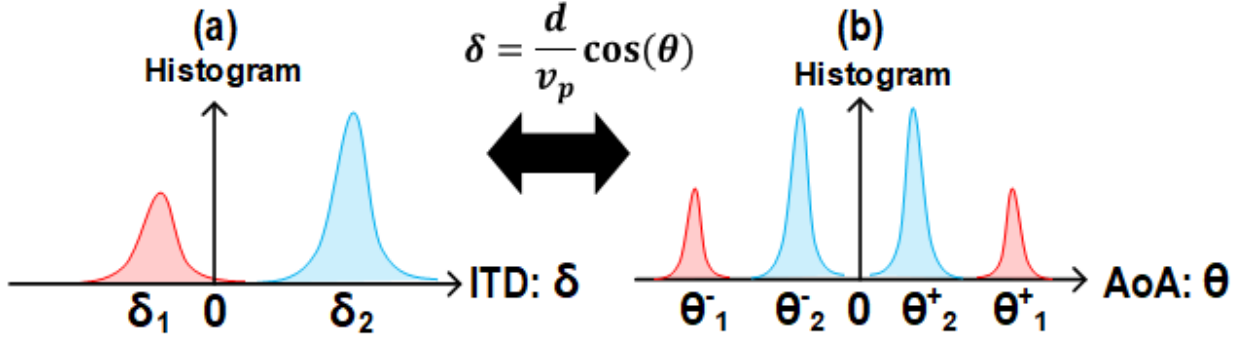


Figure 4.4: 2 ITD clusters gets mapped to 4 clusters in $(-\pi, \pi]$ AoA space.

4.3.2 Rotation-enabled AoA Disambiguation

We propose to disambiguate AoA using rotation of the microphone array. The idea is simple — as the array rotates, the ITD will change and the *direction* of this change (higher or lower) should reveal the true AoA. Fig. 4.5(a) illustrates this with a single-source example, where candidate AoAs are θ_k or $-\theta_k$. Fig. 4.5(b) plots this ITD on a graph with the X-axis showing the rotation angle of the array. Since the microphone has not made any rotation yet, the ITD is plotted for $\theta_{rot} = 0$. As the array rotates counter-clockwise, the ITD should change in one of two ways: if the true AoA = θ_k , then the ITD should increase, while for AoA = $-\theta_k$, the ITD should decrease (Figure 4.5(d)). Moreover, the trajectory of change should follow the **Cosine** curve since the ITD is a function of $\text{Cos}(\theta)$. Thus, in theory, even one small rotation should disambiguate and give us the true AoA.

Rotation-based disambiguation should be generalizable to K sources. Instead of one ITD value, we now have K ITD values at $\theta_{rot} = 0$. With rotation of the array, each ITD value would move in one of two trajectories – upward **Cosine** or downward **Cosine**, as shown in Figure 4.6 for $K = 3$. One should be able to fit K distinct **Cosine** functions through all the ITD trajectories, thereby extracting the $K = 3$ true AoAs from 6 candidates.

In practice, disambiguation is far more challenging because the ITD values become noisy. Several reasons contribute:

(1) Background interference arrives from different angles polluting the ITD clusters shown in Figure 4.4(a). Reverberations add to this pollution.

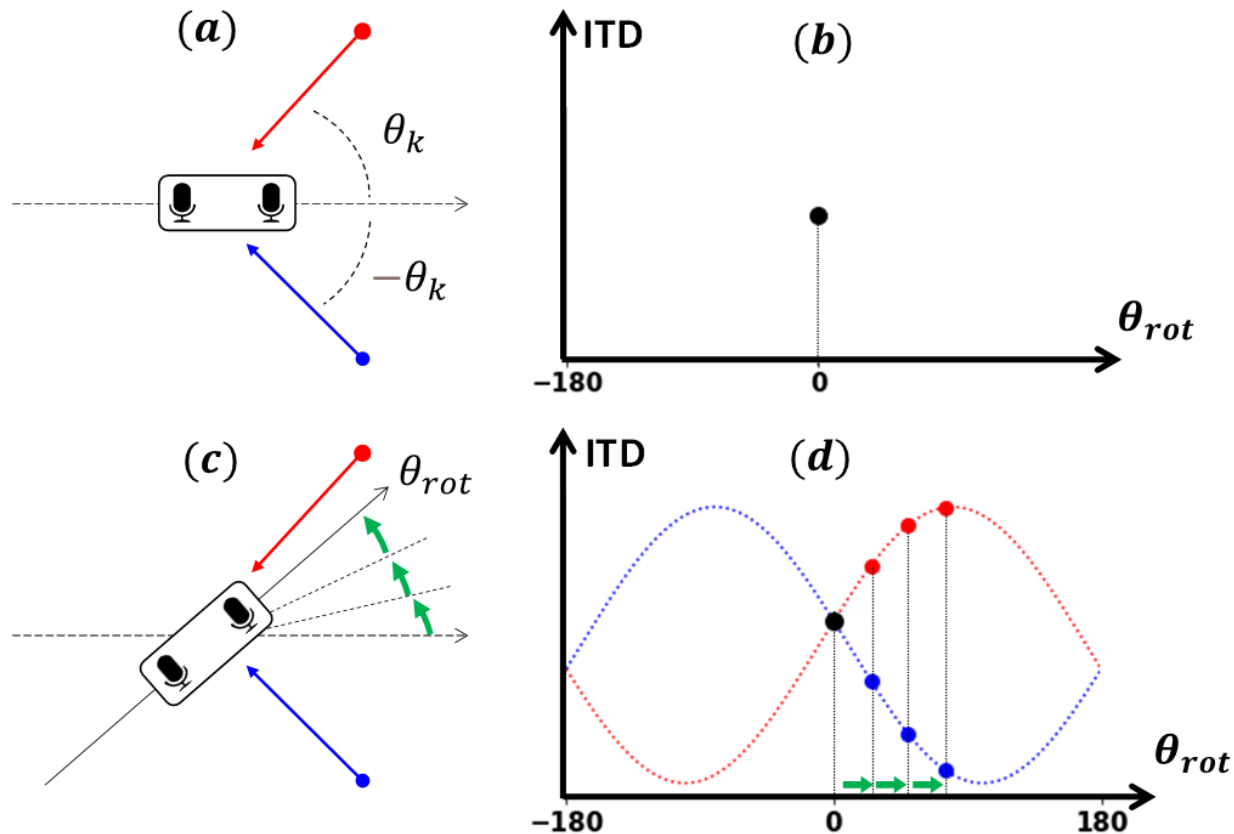


Figure 4.5: (a) Ambiguous AoAs in a static scenario, (b) Measured ITD without rotation, (c) Counter-clockwise array rotation, (d) ITD trajectory is Cosine shaped, and the direction reveals the true AoA

(2) With increasing number of sources, $K \geq 3$, the WDO property begins to break down, meaning that sources begin to collide with higher probability in time-frequency bins. Collisions produce incorrect ITD values, shifting the peaks in Figure 4.4(a).

(3) There is no guarantee that all K ITD peak values would be prominent at every step of rotation; a source pair may have similar (or identical) ITD values, say when their AoAs are 30° and -30° . This smudges the ITD estimates at that rotational step.

(4) Finally, the ITD does not vary linearly with every step of array rotation. The ITD variation is large when θ is near 90° and small when θ is 0° (note that the $\frac{d\text{Cos}(\theta)}{d\theta}$ is zero when $\theta = 0$). This implies that ITD noise must be treated differently for different regimes of θ_k .

Figure 4.7 shows measurements from a real indoor scenario where the microphone array is rotated 8 steps, with 20° per step. The smudged ITDs are from $K = 4$ different sources, implying that we have 8 candidate AoAs to disambiguate. Said differently, 4 Cosine functions need to be fitted to the measured data, essentially making it a problem in regression.

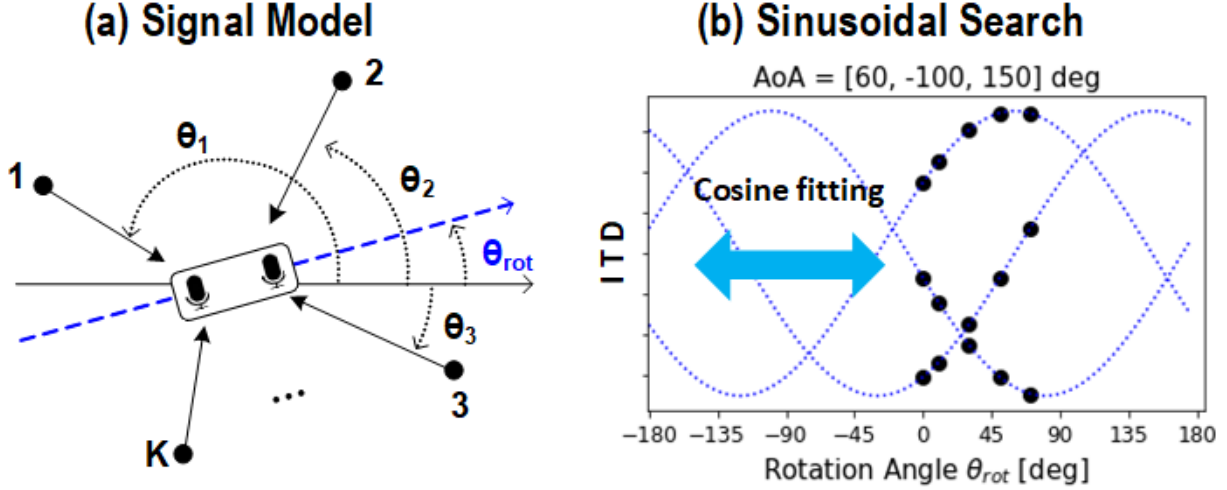


Figure 4.6: (a) Two-dimensional rotation under K sources seen from above. (b) $K = 3$ case with 3 fitted Cosine trajectories in the ITD measurements.

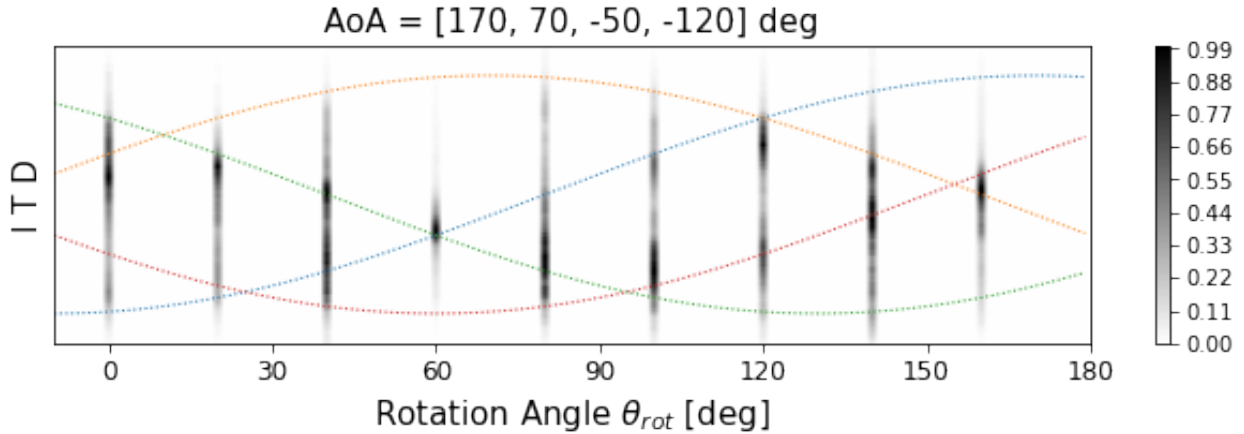


Figure 4.7: ITD measurements with $K = 4$ sources for consecutive microphone rotation, performed in a real indoor environment with background noise and reverberation.

4.3.3 Statistical Approach

Our proposed solution can be intuitively summarized as follows. We compute a likelihood for all AoAs based on the initial ITD measurements. Then, for every rotation of θ_{rot} , we model the expected ITD for each AoA and match it against the new measurement – this gives us an updated likelihood per AoA. With more rotational steps, the likelihood of the true AoAs begin to show sharper peaks, while the ambiguous and the incorrect AoAs die down. We normalize the per-AoA-likelihood and call it the “AoA spectrum” – Figure 4.8 plots real AoA spectrums after each rotation of the array. The peaks in the AoA spectrum sharpen gradually and after several rotations, converge to the $K = 4$ correct peaks. Mathematically, our algorithm can be specified in 3 essential steps as follows:

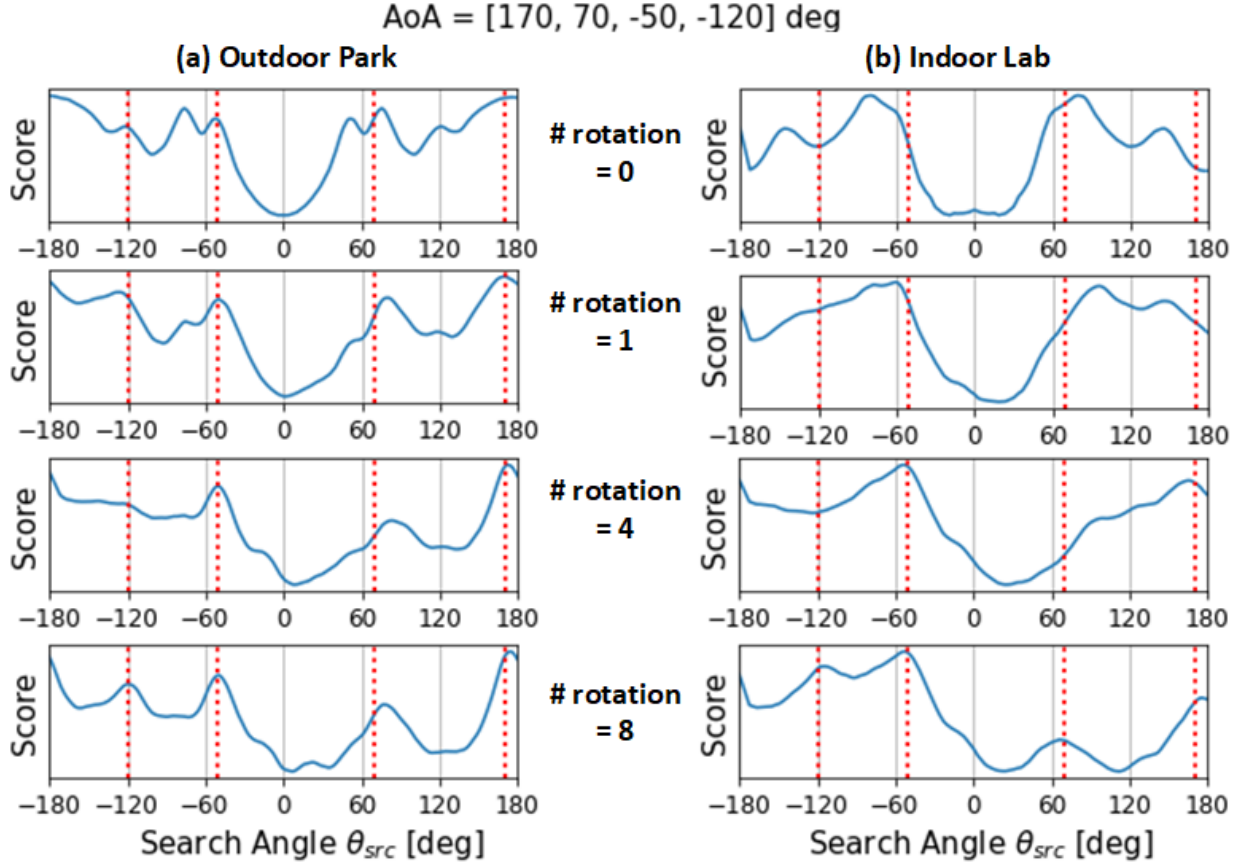


Figure 4.8: As microphone takes more rotational measurements, peaks near truth AoAs (dotted red) get clearer, offering better AoA detection.

Step 1: At each rotation angle $\theta_{rot}^{(r)}$, ($r = 0, 1, \dots, R$), use the ITD histogram to estimate probability density function (PDF) as: $\hat{p}(\delta^{(r)})$. Normalize the PDF to not penalize the ITDs that are absent.

Step 2: Calculate likelihood for each AoA, θ_{src} , at the r -th rotation as: $L^{(r)}(\theta_{src}) = \hat{p}\left(\frac{d}{v_p} \cos(\theta_{src} - \theta_{rot}^{(r)})\right)$.

Step 3: Compute overall likelihood across R rotations $\prod_{r=0}^R L^{(r)}(\theta_{src})$ with normalization. Identify θ_{src} values that do not change more than ϵ for 3 consecutive rotations; announce these as the K source AoAs.

4.3.4 Optimal Bisection Angle for Source Separation

Once AoAs are estimated, RoSS needs to rotate the microphone array to bisect two interferers. Given $K - 1$ interferers, there are $\binom{K-1}{2}$ candidate pairs. *Which pair should RoSS bisect?*

To answer this question, we need to establish two insights:

- (1) A target signal can be perfectly isolated when its ITD distribution (as shown in Figure

4.3) does not overlap with any of the interferer’s ITD distributions.

(2) Rotation of the microphone array produces unequal shifts in the ITD distributions. This is because the ITD is proportional to $\text{Cos}(AoA)$, hence for a given rotation, AoAs near 0 or 180° experience smaller ITD shifts, compared to AoAs near 90 or 270°.

Given these 2 facts, the optimal rotation becomes the following optimization question: *what final orientation angle θ_{final}^* maximizes the minimum ITD separation between the target and the interferers?* The formal optimization is as follows:

$$\theta_{final}^* = \underset{\theta_{rot}}{\operatorname{argmax}} \min_{k, k \neq T} |\delta_T - \delta_k| \tag{4.6}$$

Here δ_T is the mean ITD for the target signal (T) and δ_k is the mean ITD of each interferer. Barring some rare cases, θ_{final}^* is indeed an angle that bisects a pair of interferers (we omit the proof in the interest of space). Hence, the above optimization needs to search only across the $\binom{K-1}{2}$ bisection angles, as opposed to all possible θ_{rot} .

Isolating Any Given Target: In conclusion, given a mixture of K sources, and a target signal T for isolation, RoSS rotates to the θ_{final}^* orientation. The target signal T can be specified either by its AoA (e.g., a robot sees a person in it’s camera view and isolates that person’s voice), or the target signal’s voice fingerprint may be given to the robot, in which case it checks which voice signal matches the fingerprint. Once the fingerprint matches, RoSS continues to track that AoA and isolate that voice signal.

Delay: Note that if sources come and go, the problem is easier because K is smaller at any given time. However, if K sources are continuously present, RoSS has the time to rotate and resolve them. Once AoAs are known once, rotation to θ_{final}^* is fast, hence, any given source can be separated so long as they are not moving fast.

4.4 Evaluation

4.4.1 Experimental Settings

Measurements: RoSS is implemented on a custom-built rotary platform actuated by a NEMA-17 stepper motor (Fig. 4.9(a)). The open-loop motor uses a TB-6600 driver with peak rotation speed and acceleration of 225 deg/s and 112.5 deg/s^2 . A ReSpeaker microphone array [131] connected to a Raspberry Pi is mounted on the rotary platform and 2 adjacent microphones, with 5cm spacing, are used to record audio signals. Rotations are performed in 20° increments. The table 4.1 lists some of the environmental parameters. In each environment,

K speech signals were played from loud speakers placed radially around the microphone, at distances between 2 to 2.5m. The speech signals are 1-minute-long male/female voice recordings from 11 independent speakers, drawn from the LibriTTS dataset[132] where signal powers are almost identical, i.e., $SIR \approx -10\log(K - 1)$ for K -sources. Multiple runs were performed per configuration, with various mixtures of voices (males, females, and mixed genders), $K \in [3, 4]$, and K AoA angles chosen uniform randomly between $[0, 360]$. Fig. 4.9(b,c,d) show example images from our experiment sites.

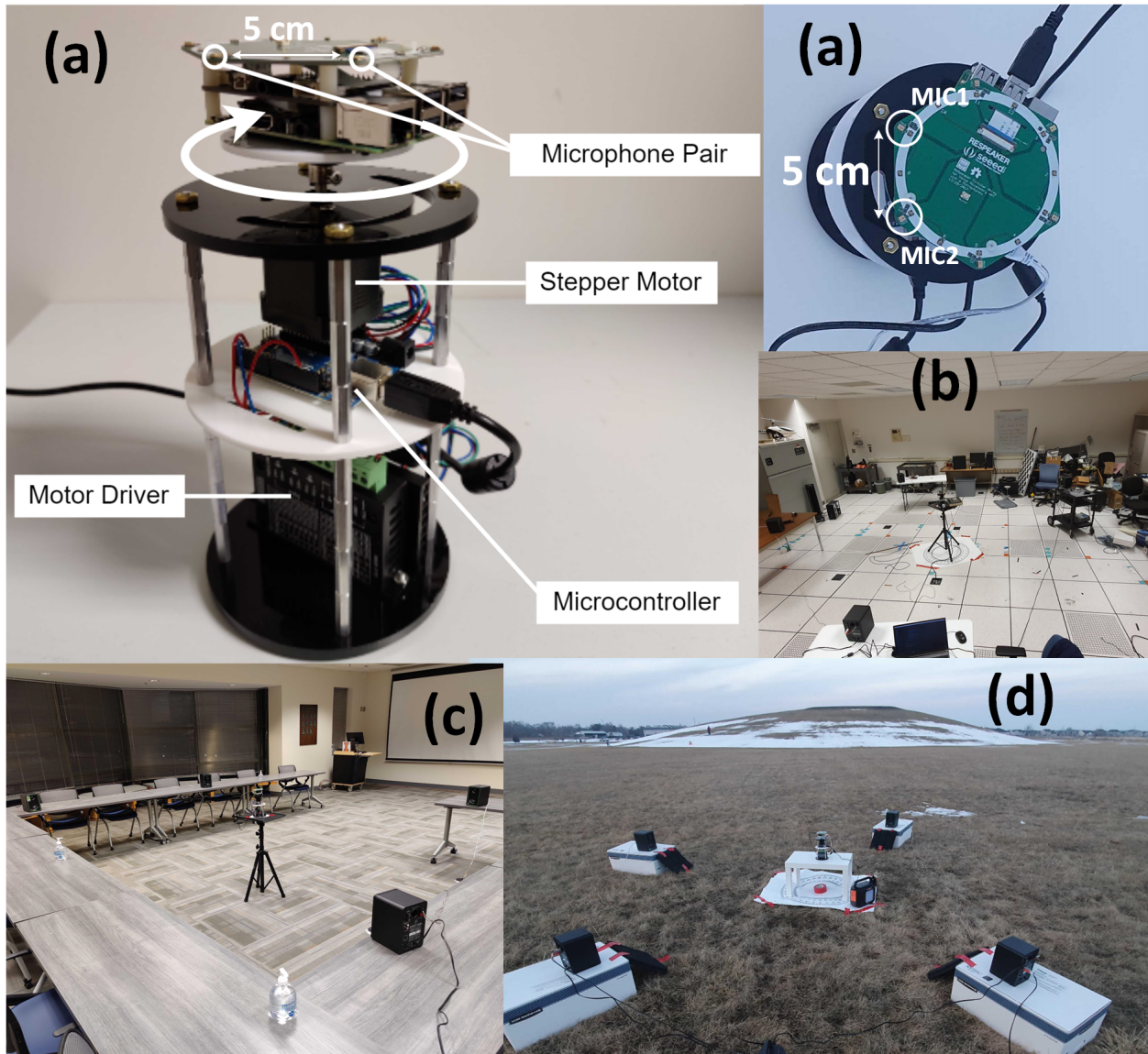


Figure 4.9: (a) Custom-built rotary platform with ReSpeaker microphone array. (b) Laboratory. (c) Conference room. (d) Local park.

The audio recordings are sampled at 16kHz, with STFT frame lengths of 512 or 1024 with 25% overlap with adjacent frames. For comparison, we use three popular source separation

Table 4.1: Evaluation Environments

Settings	Location	SNR [dB]	Room size [$m \times m$]
Lab	Indoor Lab	22	$\approx 8.4 \times 8.2$
Room	Indoor Room	23	$\approx 6 \times 8$
Park	Outdoor Park	15.4	$> 20 \times 20$
Sim	Simulation	15	10×10

algorithms, namely natural gradient-based IVA[109], DUET[116] and MVDR[110].

Simulation: To test RoSS over a wider range of parameters, we simulate the microphone recordings using a room impulse response (RIR) generator [133]. The convolutive mixtures from K sources are denoted $X_1(t), X_2(t)$. The key parameters of the simulations are:

- Room size: 10m x 10m (2-dimensional space assumed) with reverberation time T_{60} of 0, 450, 700 ms.
- Two omni-directional microphones with 5cm spacing are located in the room-center, rotating around their center.
- Gaussian noise is added so that microphone SNR is 15 dB while maintaining SIR of $-10\log(K-1)$ dB
- Separated sources are evaluated by comparing with each source alone measured at the reference microphone $X_1(t)$.
- Algorithm settings are similar to the measurement settings except for 24kHz sampling frequency.

4.4.2 Performance Metric

AoA Error: Once the AoA estimate $\hat{\theta}$ is available, the AoA error is the smaller angular difference between the ground truth AoA θ^* and the $\hat{\theta}$. However, recall that AoA ambiguity exists, meaning $2K$ AoA candidates appear for K true AoAs. In such settings, we calculate the AoA error as follows. We create K buckets, one for each true AoA. A candidate AoA is assigned to bucket j if that candidate is angularly closest to the j^{th} true AoA. The average AoA error per bucket is then computed – this gives us K AoA errors. If a bucket has no AoA, we assign a maximum possible error as a penalty.

Source Separation: Once a source has been separated as \hat{s} from a mixture m , we report SI-SDR and SI-SDR *improvement*[129], [134] defined as:

$$\text{SI-SDR}_i = \text{SI-SDR}(\hat{s}, s) - \text{SI-SDR}(m, s)$$

Here s is the source signal recorded at the microphone without any interference; this serves as ground truth.

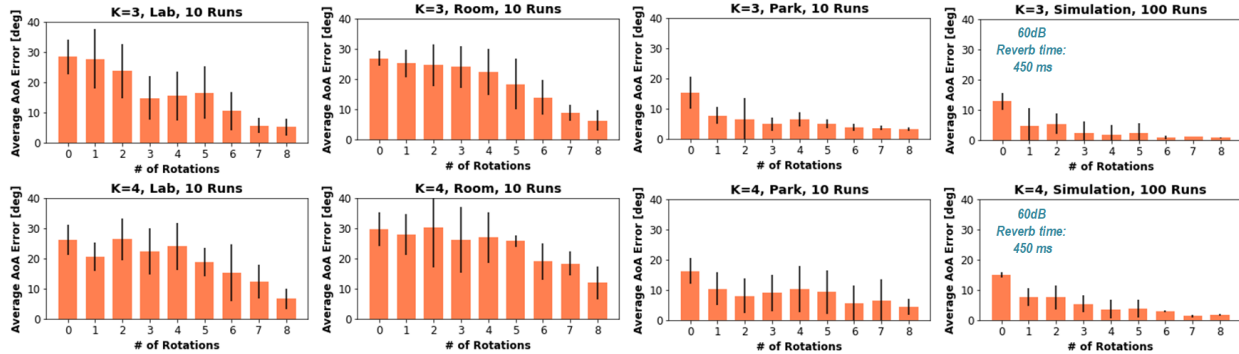


Figure 4.10: Average AoA estimation error over consecutive rotational steps in various locations and configurations. Error bars show standard deviations.

4.4.3 Results

Comparison between RoSS and Existing Algorithms: Fig. 4.11 compares RoSS’s source separation (SS) performance with SOTA algorithms, IVA and DUET. The X-axis shows the initial orientation of the microphone array – understandably, IVA and DUET’s performance vary as a function of this initial orientation. The solid lines show their median performance over 50 different configurations, while the light-color bands are [80, 20] percentiles. Since RoSS rotates to the optimal orientation, its performance remains consistent (and matches IVA when the initial orientation is luckily the optimal). With $K = 3$ sources, IVA outperforms DUET when the array orientation is favorable to it, but for other orientations (and when the sources increase to $K = 4$), DUET gains due to the inherent WDO property of speech. The yellow shaded area depicts the overall gain from RoSS, which is essentially the value of microphone rotation. Since RoSS is complementary to IVA, DUET, and other algorithms, this gain should be always available.

AoA Estimation: Fig. 4.10 plots the reduction of AoA error against rotation, where each rotation-step is ≈ 1.6 seconds. Each graph shows the average AoA error across all experiments in a given setting (Lab, Room, Park, Sim); the error bars denote standard deviations. As RoSS rotates the microphones, the AoA error reliably converges to the true AoA angle. Simulation and outdoor settings converge faster and more accurately, mainly due to lower reverberation, compared to indoor labs and rooms. Importantly, AoA estimation is a by-product of RoSS and can be leveraged as an independent capability in other applications, such as localization, imaging, and radar-based perception.

Parameterized Simulations: Fig. 4.12(a) shows how SI-SDR degrades with increasing K but RoSS continues to outperform others. Informed RoSS is a variant of RoSS where the AoAs are accurately known, such as in audio-visual systems [135], [136] — the gains are slight, implying RoSS’s AoA estimation is reliable. Fig. 4.12(b) plots SI-SDR against varying

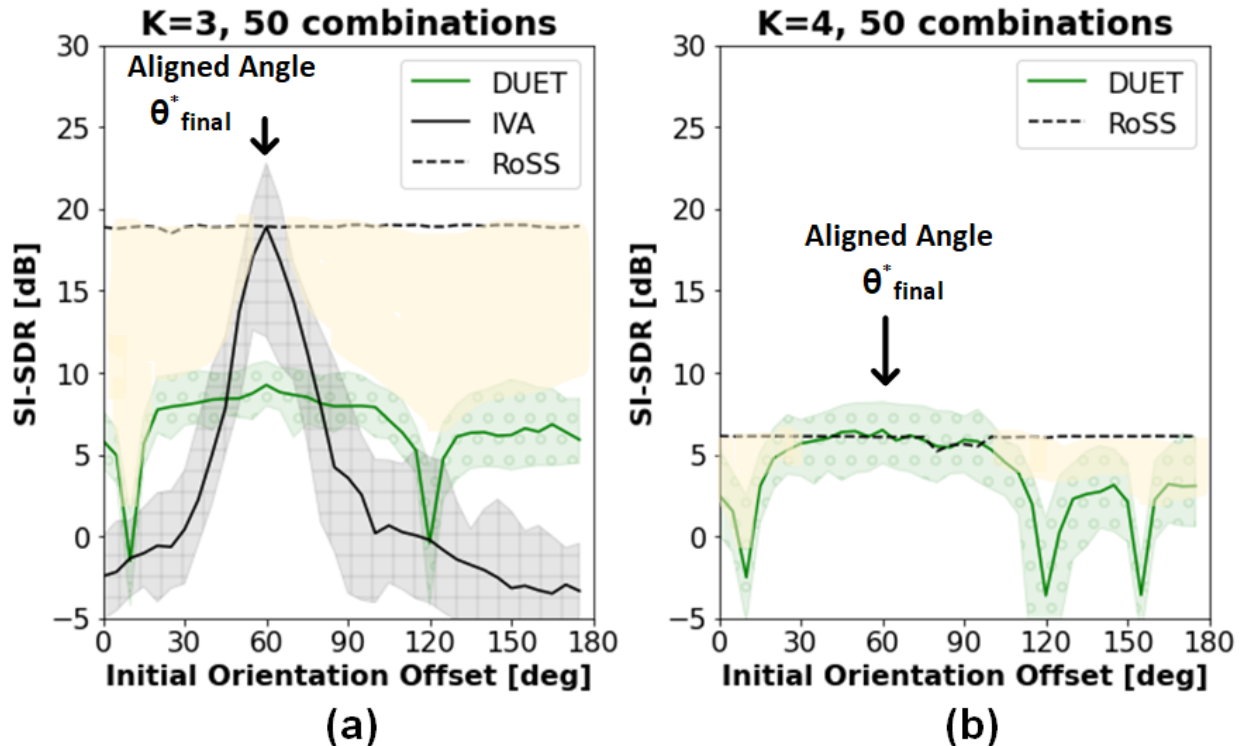


Figure 4.11: Source separation performance with different initial orientation of the microphone array, showing non-uniform patterns.

reverberation levels – the indoor setting exhibiting the highest reverberation. Performance understandably degrades with reverberation and larger K since AoA errors and TF-collisions are both high. Performance sometimes degrades outdoors from strong winds and background noise, however such degradation affect all source separation methods.

4.5 Conclusion and Future Work

We show that microphone rotation ushers an opportunity in audio AoA estimation and source separation, especially in under-determined settings. We demonstrate that optimal rotation can align/alias two interferers in the delay space, making them appear as one. This alignment is complementary to existing algorithms, offering promising results in simulations and real reverberant environments.

Further improvements are possible in at least 2 directions: (1) an adaptive rotation policy that converges faster, ideally within a few spoken words, and (2) updating the algorithm to circular microphone arrays. We leave these to future work.

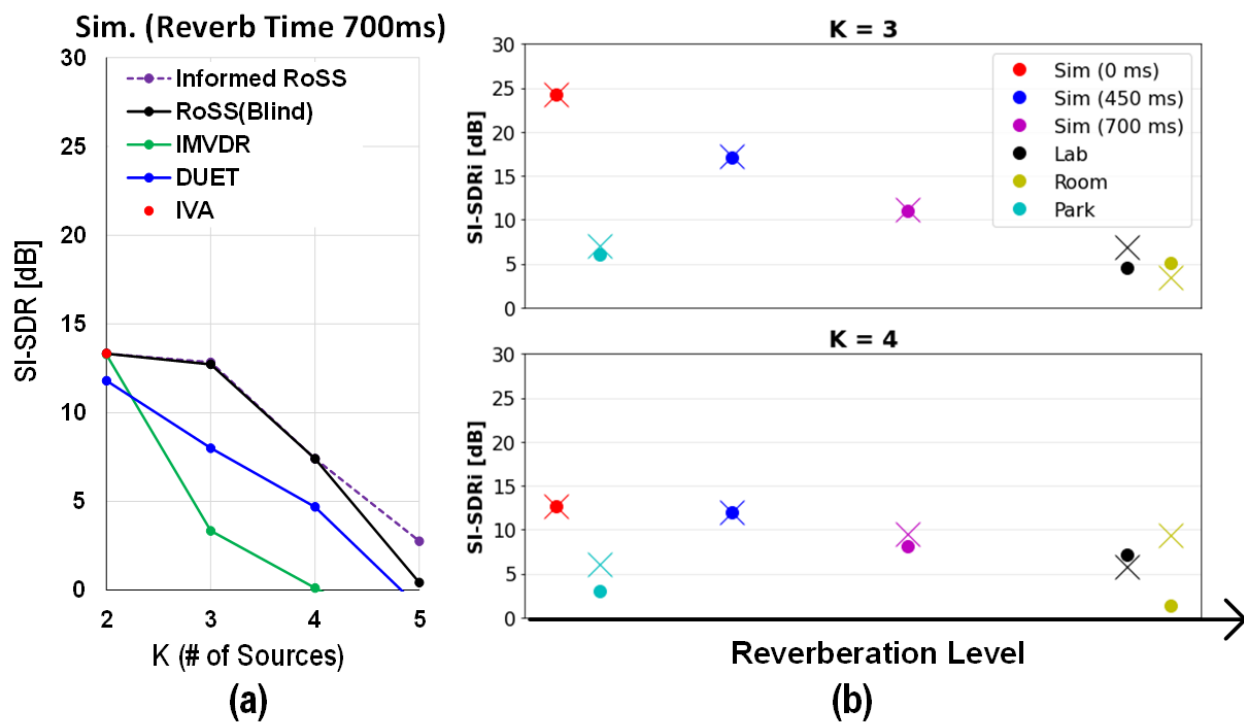


Figure 4.12: Average SI-SDR/SI-SDRi of (a) various algorithms, in (b) different setups where X markers are AoA-informed RoSS.

Chapter 5

Conclusion and Future Works

5.1 Summary of Thesis

This thesis has proposed wireless/acoustic receiver techniques to deal with interference signals in spectral/spatial domains respectively by relating the design with aliasing phenomenon. For the wireless spectral interference case, the challenge in increasing number of acoustic filters in sub-7 GHz receiver has been tackled by adopting LPTV N-path mixer topology for programmable wide center-frequency tuning capability. By showing that the mixer filter interaction becomes interesting when acoustic filter's input impedance gets noisy from harmonic feedback process, it has been demystified that noisy impedance gets aliased on top of each other where spectral anti-aliasing is required to prevent such problems. Two mixer-first super-heterodyne receiver design has been showcased with custom-designed chips fabricated in 65nm CMOS process, showing that with only one or two acoustic filters, SAW or BAW, more than 20 bands can be covered via continuous wideband tuning while maintaining sharp filter selectivity and high linearity.

Another key contribution is to reject the spatial interference signals in multi-sensor receiver arrays. Unlike prior works that suppress spatial aliasing to have unique steering beam patterns, a new idea has been proposed to exploit the spatial aliasing instead to solve under-determined inverse problem in blind source separation framework. That is, more than 2 spatial sources can be dealt with by only using 2 sensors by aligning interfering sources via rotation to put them on the same aliased beam patterns. This has been demonstrated in speech enhancement applications by having 2 rotating microphones with more than 2 speech sources. By rotation, angle-of-arrivals of all sources can be identified at the same time target speech signal can be enhanced even with linear estimators, such as adaptive beamforming weights and independent component analysis.

5.2 Future Works

5.2.1 RF-inspired Artificial Neural Network

In the past decade, deep learning has made unprecedented achievements on numerous applications including classification, regression/estimation [118], [137]. Recently, a number of different concepts for realizing artificial neurons in various domains such as analog electronics, photonics [138], [139], quantum [140]. Some of the key motivations for such approaches is said to be on high computing speed and low power consumption compared to conventional digital circuit-based multiply-accumulate (MAC) operations [139]. Thus, there are already various computing applications of in-memory computing [141], [142] or in-block analog computing [143], [144], exotic hardware-based computing [145] to quickly perform simple decision making to give prior information to digital back-end to reduce computing time. As a future work, an attempt to build a neuron utilizing impedance aliasing phenomenon introduced in Chapter 1, 2, and 3 is introduced here.

Typical artificial neural network contains a neuron as a unit block. And it takes input vector $\vec{X} = [X_1, \dots, X_N]^T$ then multiply with the transpose of weight vector $\vec{w} = [w_1, \dots, w_N]^T$. Then, by adding a bias b , some sort of non-linearity is introduced afterwards as an activation function ϕ . This is depicted in Fig. 5.1.

Now, let us remind ourselves on the N-path circuit in Fig. 1.4. Based on equation (1.11) as copied below where harmonic gain $\gamma_n = \frac{1}{N} \text{sinc}^2(\frac{n\pi}{N})$,

$$Z_{x,open}(\omega) = \frac{V_x(\omega)}{I_S(\omega)} = \sum_{n=-\infty}^{\infty} \gamma_n Z_L(\omega - n\omega_{LO}) \quad (5.1)$$

Note that the voltage at harmonic locations contain modulated information that has weighted sum of harmonic gain values γ_n and shifted impedance values $Z_L(\omega - n\omega_{LO})$. In previous Chapters, we suppressed this aliased impedance values. But, can we exploit this property to build a neuron?

There are several key challenges here, though. First, impedance values at harmonic frequency $Z_L(\omega - n\omega_{LO})$ has to be freely synthesized which is not easy in impedance domain. Second, pulling out the impedance or voltage value only at one frequency and adding bias value in each domain then applying nonlinearity is not a trivial job at RF due to various loading effect. Third, γ_n value is not continuous, but discrete fixed values given by $\frac{1}{N} \text{sinc}^2(\frac{n\pi}{N})$.

Here are some ways to improve the situation: For the first challenge, non-identical load impedance can be loaded behind each branch of N-path structure. To explain, let us modify the circuit as in Fig. 5.2.

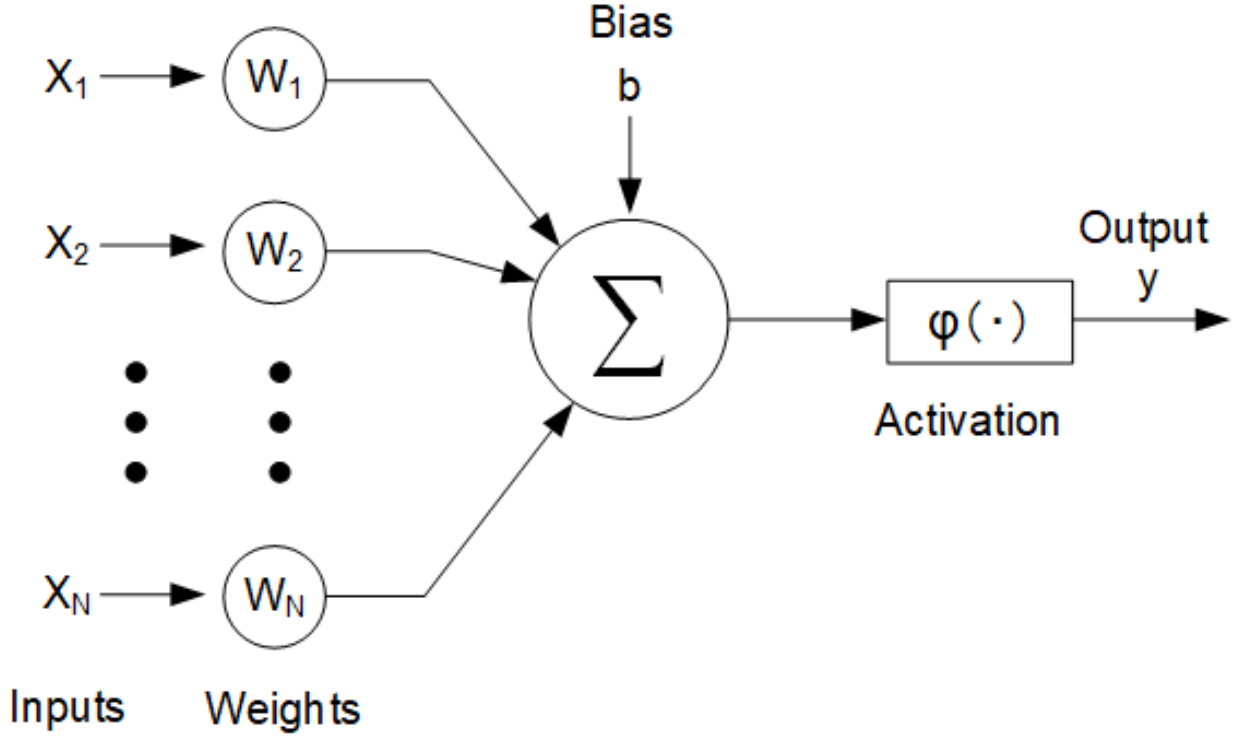


Figure 5.1: Artificial neural network

If we write down the expression for voltage at shared node x similarly:

$$\begin{aligned}
 V_x(\omega) &= \sum_{i=1}^N \sum_{m=-\infty}^{\infty} \sum_{n=-\infty}^{\infty} a_{m,i} a_{n,i} Z_{L,i}(\omega - n\omega_{LO}) I_S(\omega - (m+n)\omega_{LO}) \\
 &= \sum_{m=-\infty}^{\infty} \sum_{n=-\infty}^{\infty} a_m a_n I_S(\omega - (m+n)\omega_{LO}) \sum_{i=1}^N e^{-j\frac{2\pi}{N}(m+n)i} Z_{L,i}(\omega - n\omega_{LO})
 \end{aligned} \tag{5.2}$$

This time, complex vectors do not cancel out due to non-identical impedance values. However, it can be seen that all voltage harmonic tone contains modulated weighted sum of $e^{-j\frac{2\pi}{N}(m+n)i} Z_{L,i}(\omega - n\omega_{LO})$. For simplicity, if we make each load impedance a simple 1-peak response that can change its peak value and tuned at N frequency values, n_i :

$$V_x(\omega) = \sum_{m=-\infty}^{\infty} \sum_{i=1}^N a_m a_{n_i} I_S(\omega - (m+n_i)\omega_{LO}) e^{-j\frac{2\pi}{N}(m+n_i)i} Z_{L,i}(\omega - n_i\omega_{LO}) \tag{5.3}$$

Observing voltage at RF input current frequency should give:

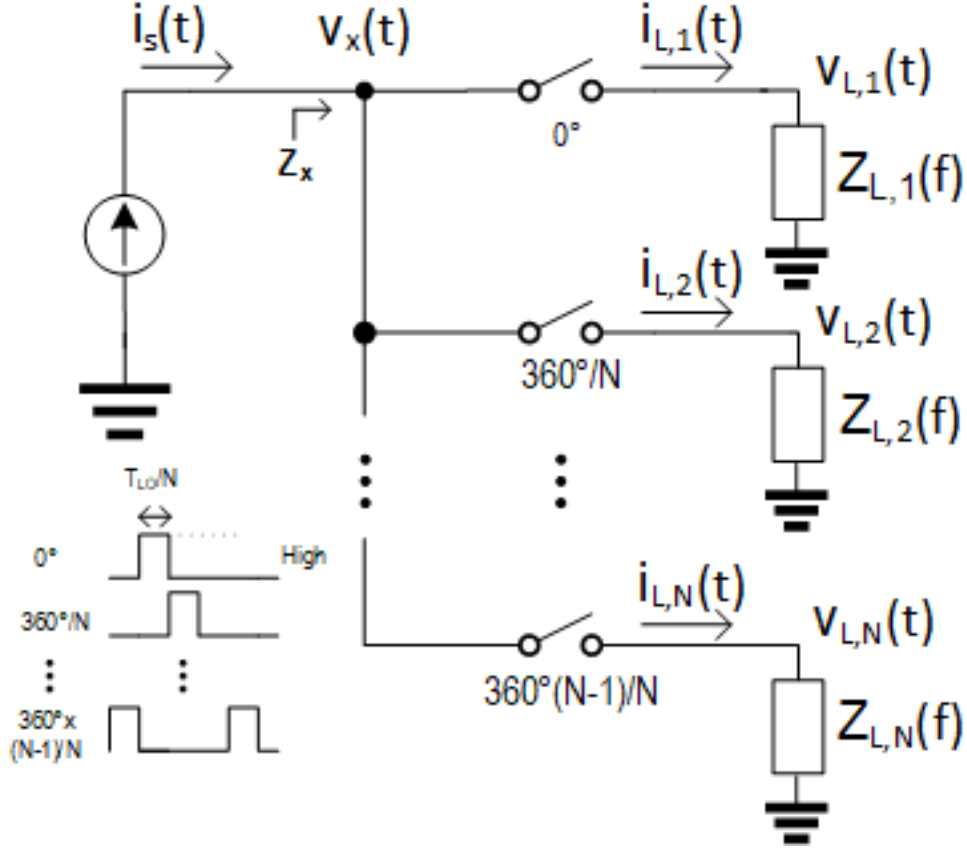


Figure 5.2: N-path structure loaded with N different load impedance

$$V_x(\omega) = \sum_{i=1}^N \gamma_{n_i} Z_L(\omega - n_i \omega_{LO}) I_S(\omega) \quad (5.4)$$

Equivalently, input impedance becomes:

$$Z_x(\omega) = \sum_{i=1}^N \gamma_{n_i} Z_L(\omega - n_i \omega_{LO}) \quad (5.5)$$

Therefore, we still keep the weighted sum formulation even with non-identical load but with 1 peak at specific location. This type of load should be much easier to implement in practice, even at RF.

Also, for the second challenge about adding a bias and applying nonlinearity, here are some potential solutions. For bias in impedance domain, switch resistance could be varied for real-impedance value change. For nonlinearity, reflection coefficient could be utilized by letting the wave travel through the transmission line to get reflected by this N-path structure

to introduce reflection coefficient of:

$$\Gamma = \frac{Z_x - Z_o}{Z_x + Z_o} \quad (5.6)$$

where Z_o is characteristic impedance of transmission line. Note that our weighted sum, Z_x , is inside a nonlinear activation function $\frac{x-a}{x+a}$.

Finally, for the third challenge on discrete γ values, LO signal that drives switches can be modulated instead to have a desired value at each frequency location. For instance, currently, the switch is driven by pulse signals where it creates sinc function in γ . By driving the switch with a different type of signal, harmonic gain can be adjusted.

In conclusion, implementing a neuron based on N-path structure has been suggested here as a future work. While feasibility is not explored at this point, the author believes that new spaces for exploration can be opened up as a new form of neuromorphic structure in direct-RF computing applications such as one proposed in here, **in-mixer computing**. Such direct-RF computing/processing can be useful in multiple applications such as 1) RF-domain self-interference cancellation problem for full-duplex communication [146], 2) end-to-end optimization in quantum controller subsystem where many quantum processors adopt qubits that have microwave frequencies 5GHz [147], 14GHz [148] which can learn the qubit state transition behavior for generating optimal control signal shapes.

5.2.2 Additional Features for Mixer-first Acoustic Filtering Receivers

In Chapter 2 and 3, the author focused on frequency translation capability by demonstrating upconverted frequency response of acoustic filter bandpass filters. However, there are further practical challenges when it comes to actual usage in modern wireless transceivers for state-of-the-art cellular or Wi-Fi applications. Depending on scenarios such as the number of simultaneous users, channel state information (CSI), available bandwidth, blocker signal level etc., it is imperative to have features mentioned below:

- Bandwidth Adjustment

Bandwidth of proposed mixer-first acoustic filtering receivers is directly inheriting the bandwidth of the acoustic filter used as a reference. However, in realistic scenarios, bandwidth adjustment is required to handle problems such as ISI (InterSymbol Interference) and channel equalization under multi-path scenarios. One potential way to simply adjust the bandwidth is to use bandwidth reconfigurable acoustic device as the reference filter such as [149]. Since center frequency tuning is handled by mixer-first N-path architecture, only bandwidth

adjustment modes need to be implemented within acoustic device itself. Another way to adjust the bandwidth is to change the impedance shaper's bandwidth in CMOS side, while keeping the acoustic response the same. As long as strong blocker is filtered out within the band, channel selection part might not need acoustic-filter-like roll-off depending on applications. In this regard, there are potential opportunities on CMOS-acoustic co-design, since proposed mixer-first acoustic filtering receiver concept benefits directly from both CMOS and acoustic device technology improvements.

- Carrier Aggregation

In conventional filter bank approaches as in Fig. 3.7-(a), instead of selecting just one band, there are cases where multiple bands have to be selected at the same time to achieve carrier aggregation. While there have been research works on multi-band mixer-first receivers by utilizing modulated LO [150], [151], the number of bands that can be occupied is limited to 2. One potential direction to investigate would be up-converting simplified filter bank that handles carrier aggregation within the selected band while band itself is tuned by mixer-first structure. This way, instead of implementing $N \gg 1$ acoustic filters and static switches as a filter bank, one could deploy $K \ll N$ filters and switches which only cover total number of channels within a band (fine-tuning), while band selection can happen coarsely by LO-tuning via N-path structures, for instance.

- Advanced Impedance Shaper and Passband Improvement

In proposed mixer-first acoustic filtering designs, the acoustic filter's passband response is not maintained after mixer up-conversion especially when acoustic filter has a wide bandwidth as in Fig. 3.14. There are multiple parameters within the signal path of the receiver that shrink the filter bandwidth, basically. One is LC-tank impedance shaper which has 2nd-order response as opposed to acoustic bandpass response which has higher-order flat passband response.

To resolve this problem, one straightforward potential solution is to design a higher-order impedance shaper to match the bandwidth of acoustic filter. However, this would end up increasing overall NF of the receiver chain because complicated bandpass response would either need series/parallel on-chip LC resonators which has limited Q-factor. One might consider implementing impedance shaper using N-path resonators, but this would face issues in existing cascaded N-path resonators. Another way to handle passband deformation is to compensate the suppression level in BB/digital domain similar to channel equalization. Before deployment, inverse transfer function of impedance shaper and other blocks that limit the bandwidth can be learned and cancelled out later on via off-line training for instance as long as OOB response is not corrupted for blocker suppression purpose.

- Adaptive Center Frequency Tuning

Now that we have the programmable tuning capability of acoustic filter center frequency using a mixer-first approach, it is of great interest knowing how fast can we tune the frequency. Due to bidirectional nature where there is harmonically coupled feedback process within N-path structure as derived in (1.11) in Chapter 1, (2.4) in Chapter 2, and contents in Chapter A, convergence time for the proposed structure to be stabilized for given LO input is not merely twice the group-delay of acoustic filters. Thus, it would be useful if transient analysis can be done on generalized N-path structure considering convergence time when control frequency (LO) is changed from one to another to find minimum bounds for adaptive tuning time.

5.2.3 Reducing Further Degrees of Freedom on Spatially Aligned Interferers in RoSS

In this thesis work regarding RoSS in Chapter 4, the proposed idea basically aligns a pair of interference to reduce the number of sources from K to K-1 while there are M microphone sensors available. Thus, degree-of-freedom gain is only 1 because one alignment can only handle a pair of interferers. Now the question is, can we do better by aligning more than 2 interferers in one rotation angle to achieve > 1 degree-of-freedom gain?

One idea is to intentionally utilize spatial aliasing patterns at each side along with front-back ambiguity by not meeting the condition (1.3) intentionally. When the spacing between sensor node d becomes larger than $\frac{\lambda_{fmax}}{2}$, aliasing over array axis would happen which authors suppressed earlier to only exploit front-back ambiguity. By adding the control over the spacing d on top of array alignment angle θ_{rot} , one could design a problem to align as many interference sources as possible in more than one ambiguity grating line, which gives equal phase shift at that frequency which was introduced as hyperbolic lines for wide-band case. Thus, for narrowband applications such as wireless array processing where all the signals are centered around carrier frequency and fractional bandwidth (FBW) is fairly limited, alignment of more than 2 interference sources on equi-phase lines may be possible. For instance, 5-source 2-antenna problem might be simplified to 2-source 2-antenna problem when there are two sensor nodes, such as drones collaborating each other with 1 antenna each.

References

- [1] M. Fitz, *Fundamentals of Communications Systems* (Communications Engineering), 1st ed. McGraw-Hill Professional, 2007, ISBN: 0071482806; 9780071482806.
- [2] J. Pahl, *Interference Analysis: Modelling Radio Systems for Spectrum Management*, 1st ed. Wiley, 2016, ISBN: 9781119065289; 1119065283.
- [3] A. E. G. Venugopal V. Veeravalli, *Interference Management in Wireless Networks: Fundamental Bounds and the Role of Cooperation*. Cambridge University Press, 2018, ISBN: 9781107165007; 1107165008.
- [4] J. S. S J. Ling and W. et al., *University Physics I-III*. openstax, 2016, ISBN: 978-1-938168-27-7.
- [5] G. C. Holst, *Sampling, aliasing, and data fidelity for electronic imaging systems, communications and data acquisition*. JCD Publishing, 1998.
- [6] E. W. Hobson, *The Theory of Functions of a Real Variable and the Theory of Fourier's Series*. Cambridge University Press, 1907.
- [7] P. M. Morse and H. Feshbach, *Fourier Transforms*. McGraw-Hill, 1953.
- [8] C. Shannon, "Communication in the presence of noise," *Proceedings of the IRE*, vol. 37, no. 1, pp. 10–21, 1949. DOI: [10.1109/JRPROC.1949.232969](https://doi.org/10.1109/JRPROC.1949.232969).
- [9] B. Razavi, *RF microelectronics*. Upper Saddle River, NJ: Prentice Hal, 2011.
- [10] M. Mikhemar, D. Murphy, A. Mirzaei, and H. Darabi, "A cancellation technique for reciprocal-mixing caused by phase noise and spurs," *IEEE Journal of Solid-State Circuits*, vol. 48, no. 12, pp. 3080–3089, 2013. DOI: [10.1109/JSSC.2013.2283758](https://doi.org/10.1109/JSSC.2013.2283758).
- [11] A. Hagelauer, G. Fattinger, C. C. W. Ruppel, M. Ueda, K. Hashimoto, and A. Tag, "Microwave Acoustic Wave Devices: Recent Advances on Architectures, Modeling, Materials, and Packaging," *IEEE Trans. Microw. Theory and Techn.*, vol. 66, no. 10, pp. 4548–4562, 2018.

- [12] P. Warder and A. Link, “Golden Age for Filter Design: Innovative and Proven Approaches for Acoustic Filter, Duplexer, and Multiplexer Design,” *IEEE Microw. Mag.*, vol. 16, no. 7, pp. 60–72, 2015.
- [13] T. Bauer, C. Eggs, K. Wagner, and P. Hagn, “A Bright Outlook for Acoustic Filtering: A New Generation of Very Low-Profile SAW, TC SAW, and BAW Devices for Module Integration,” *IEEE Microw. Mag.*, vol. 16, no. 7, pp. 73–81, 2015.
- [14] M. Zolfagharloo Koochi and A. Mortazawi, “Reconfigurable Radios Employing Ferroelectrics: Recent Progress on Reconfigurable RF Acoustic Devices Based on Thin-Film Ferroelectric Barium Strontium Titanate,” *IEEE Microw. Mag.*, vol. 21, no. 5, pp. 120–135, 2020.
- [15] E. A. Klumperink, H. J. Westerveld, and B. Nauta, “N-path filters and mixer-first receivers: A review,” in *2017 IEEE Custom Integrated Circuits Conference (CICC)*, 2017, pp. 1–8. DOI: [10.1109/CICC.2017.7993643](https://doi.org/10.1109/CICC.2017.7993643).
- [16] J. M. Manley and H. E. Rowe, “Some general properties of nonlinear elements-part i. general energy relations,” *Proceedings of the IRE*, vol. 44, no. 7, pp. 904–913, 1956. DOI: [10.1109/JRPROC.1956.275145](https://doi.org/10.1109/JRPROC.1956.275145).
- [17] H. E. Rowe, “Some general properties of nonlinear elements. ii. small signal theory,” *Proceedings of the IRE*, vol. 46, no. 5, pp. 850–860, 1958. DOI: [10.1109/JRPROC.1958.286938](https://doi.org/10.1109/JRPROC.1958.286938).
- [18] M. C. M. Soer, E. A. M. Klumperink, P. de Boer, F. E. van Vliet, and B. Nauta, “Unified Frequency-Domain Analysis of Switched-Series-RC Passive Mixers and Samplers,” *IEEE Trans. Circuits Syst. I: Reg. Papers*, vol. 57, no. 10, pp. 2618–2631, 2010.
- [19] A. Ghaffari, E. A. M. Klumperink, M. C. M. Soer, and B. Nauta, “Tunable High-Q N-Path Band-Pass Filters: Modeling and Verification,” *IEEE J. Solid-State Circuits*, vol. 46, no. 5, pp. 998–1010, 2011.
- [20] N. Reiskarimian and H. Krishnaswamy, “Design of all-passive higher-order CMOS N-path filters,” in *IEEE Radio Frequency Integrated Circuits Symposium (RFIC) Dig.*, 2015, pp. 83–86.
- [21] A. Mirzaei, H. Darabi, and D. Murphy, “Architectural Evolution of Integrated M-Phase High-Q Bandpass Filters,” *IEEE Trans. Circuits Syst. I: Reg. Papers*, vol. 59, no. 1, pp. 52–65, 2012.
- [22] F. J. Harris, *Multirate Signal Processing for Communication Systems*. Prentice Hall, 2004, ISBN: 0137009054; 9780137009053; 4094174184; 9784094174182.

- [23] O. of engineering, technology policy, and rules division, “Fcc online table of frequency allocations,” 2021. [Online]. Available: <https://www.fcc.gov/file/21474/download>.
- [24] M. A. Bee and C. Micheyl, “The cocktail party problem: What is it? how can it be solved? and why should animal behaviorists study it?,” vol. 122(3), pp. 235–251, 2008. DOI: [10.1037/0735-7036.122.3.235](https://doi.org/10.1037/0735-7036.122.3.235).
- [25] J. H. McDermott, “The cocktail party problem,” vol. 19, 2009. DOI: [10.1016/j.cub.2009.09.005](https://doi.org/10.1016/j.cub.2009.09.005).
- [26] S. M. et al., “Audio source separation,” Springer, 2018.
- [27] S. Makino, S. Araki, S. Winter, and H. Sawada, “Underdetermined blind source separation using acoustic arrays,” in *Handbook on Array Processing and Sensor Networks*, Wiley, 2009.
- [28] H. Sawada, N. Ono, H. Kameoka, D. Kitamura, and H. Saruwatari, “A review of blind source separation methods: Two converging routes to ilrma originating from ica and nmf,” *APSIPA Transactions on Signal and Information Processing*, vol. 8, e12, 2019. DOI: [10.1017/ATSIP.2019.5](https://doi.org/10.1017/ATSIP.2019.5).
- [29] B. Van Veen and K. Buckley, “Beamforming: A versatile approach to spatial filtering,” *IEEE ASSP Magazine*, vol. 5, no. 2, pp. 4–24, 1988. DOI: [10.1109/53.665](https://doi.org/10.1109/53.665).
- [30] X.-L. Li, *Independent vector analysis with deep neural network source priors*, 2020. arXiv: [2008.11273](https://arxiv.org/abs/2008.11273) [eess.AS].
- [31] J. Shlens, *A tutorial on independent component analysis*, 2014. arXiv: [1404.2986](https://arxiv.org/abs/1404.2986) [cs.LG].
- [32] H. Seo and J. Zhou, “A 2.5-to-4.5-GHz Switched-LC-Mixer-First Acoustic-Filtering RF Front-End Achieving <6dB NF, +30dBm IIP3 at 1 x Bandwidth Offset,” in *IEEE Radio Frequency Integrated Circuits Symposium (RFIC) Dig.*, 2020.
- [33] H. Seo and J. Zhou, “A Passive-Mixer-First Acoustic-Filtering Superheterodyne RF Front-End,” *IEEE J. Solid-State Circuits*, vol. 56, no. 5, pp. 1438–1453, 2021.
- [34] P. Cheng, Z. Chen, M. Ding, Y. Li, B. Vucetic, and D. Niyato, “Spectrum Intelligent Radio: Technology, Development, and Future Trends,” *IEEE Commun. Mag.*, vol. 58, no. 1, pp. 12–18, 2020.
- [35] M. Darvishi, “Active N-path Filters: Theory and Design,” *Ph.D. Dissertation*, 2013.
- [36] P. Song and H. Hashemi, “RF Filter Synthesis Based on Passively Coupled N-Path Resonators,” *IEEE J. Solid-State Circuits*, vol. 54, no. 9, pp. 2475–2486, 2019.

- [37] F. Amin, S. Raman, and K. Koh, “Integrated Synthetic Fourth-Order Q -Enhanced Bandpass Filter With High Dynamic Range, Tunable Frequency, and Fractional Bandwidth Control,” *IEEE J. Solid-State Circuits*, vol. 54, no. 3, pp. 768–784, 2019.
- [38] Y. Lien, E. A. M. Klumperink, B. Tenbroek, J. Strange, and B. Nauta, “Enhanced-Selectivity High-Linearity Low-Noise Mixer-First Receiver With Complex Pole Pair Due to Capacitive Positive Feedback,” *IEEE J. Solid-State Circuits*, vol. 53, no. 5, pp. 1348–1360, 2018.
- [39] E. C. Szoka and A. Molnar, “Circuit Techniques for Enhanced Channel Selectivity in Passive Mixer-First Receivers,” in *IEEE Radio Frequency Integrated Circuits Symposium (RFIC) Dig.*, 2018, pp. 292–295.
- [40] S. Krishnamurthy and A. M. Niknejad, “Design and Analysis of Enhanced Mixer-First Receivers Achieving 40-dB/decade RF Selectivity,” *IEEE J. Solid-State Circuits*, vol. 55, no. 5, pp. 1165–1176, 2020.
- [41] G. Pini, D. Manstretta, and R. Castello, “Analysis and Design of a 260-MHz RF Bandwidth +22-dBm OOB-IIP3 Mixer-First Receiver With Third-Order Current-Mode Filtering TIA,” *IEEE J. Solid-State Circuits*, vol. 55, no. 7, pp. 1819–1829, 2020.
- [42] Y. Yang, R. Lu, T. Manzanque, and S. Gong, “Toward Ka Band Acoustics: Lithium Niobate Asymmetrical Mode Piezoelectric MEMS Resonators,” in *2018 IEEE International Frequency Control Symposium (IFCS)*, 2018, pp. 1–5.
- [43] R. Aigner, G. Fattinger, M. Schaefer, K. Karnati, R. Rothmund, and F. Dumont, “BAW Filters for 5G Bands,” in *2018 IEEE International Electron Devices Meeting (IEDM)*, 2018, pp. 14.5.1–14.5.4.
- [44] L. Gao, T. Lin, and G. M. Rebeiz, “Design of Tunable Multi-Pole Multi-Zero Bandpass Filters and Diplexer With High Selectivity and Isolation,” *IEEE Trans. Circuits Syst. I: Reg. Papers*, vol. 66, no. 10, pp. 3831–3842, 2019.
- [45] Z. Yang, R. Zhang, and D. Peroulis, “Design and Optimization of Bidirectional Tunable MEMS All-Silicon Evanescent-Mode Cavity Filter,” *IEEE Trans. Microw. Theory and Techn.*, vol. 68, no. 6, pp. 2398–2408, 2020.
- [46] A. Abbaspour-Tamijani, L. Dussopt, and G. M. Rebeiz, “Miniature and tunable filters using MEMS capacitors,” *IEEE Trans. Microw. Theory and Techn.*, vol. 51, no. 7, pp. 1878–1885, 2003.

- [47] H. Joshi, H. H. Sigmarsson, S. Moon, D. Peroulis, and W. J. Chappell, “High-Q Fully Reconfigurable Tunable Bandpass Filters,” *IEEE Trans. Microw. Theory and Techn.*, vol. 57, no. 12, pp. 3525–3533, 2009.
- [48] N. Testi, R. Berenguer, X. Zhang, S. Munoz, and Y. Xu, “A 2.4GHz 72dB-variable-gain 100dB-DR 7.8mW 4th-order tunable Q-enhanced LC band-pass filter,” in *IEEE Radio Frequency Integrated Circuits Symposium (RFIC) Dig.*, 2015, pp. 87–90.
- [49] M. Lee, H. Wu, and C. Clive Tzuang, “1.58-GHz Third-Order CMOS Active Bandpass Filter With Improved Passband Flatness,” *IEEE Trans. Microw. Theory and Techn.*, vol. 59, no. 9, pp. 2275–2284, 2011.
- [50] J. Zhou, T.-H. Chuang, T. Dinc, and H. Krishnaswamy, “Integrated wideband self-interference cancellation in the RF domain for FDD and full-duplex wireless,” *IEEE J. Solid-State Circuits*, vol. 50, no. 12, pp. 3015–3031, Dec. 2015.
- [51] K. Kibaroglu and G. M. Rebeiz, “An N-path bandpass filter with a tuning range of 0.1–12 GHz and stopband rejection > 20 dB in 32 nm SOI CMOS,” in *IEEE International Microwave Symposium (IMS) Dig.*, 2016, pp. 1–3.
- [52] C. Andrews and A. C. Molnar, “A Passive Mixer-First Receiver With Digitally Controlled and Widely Tunable RF Interface,” *IEEE J. Solid-State Circuits*, vol. 45, no. 12, pp. 2696–2708, 2010.
- [53] C. Andrews and A. C. Molnar, “Implications of Passive Mixer Transparency for Impedance Matching and Noise Figure in Passive Mixer-First Receivers,” *IEEE Trans. Circuits Syst. I: Reg. Papers*, vol. 57, no. 12, pp. 3092–3103, 2010.
- [54] P. K. Sharma and N. Nallam, “Breaking the performance tradeoffs in n-path mixer-first receivers using a second-order baseband noise-canceling filter,” *IEEE J. Solid-State Circuits*, pp. 1–1, 2020.
- [55] Y. Lien, E. A. M. Klumperink, B. Tenbroek, J. Strange, and B. Nauta, “High-Linearity Bottom-Plate Mixing Technique With Switch Sharing for N -path Filters/Mixers,” *IEEE J. Solid-State Circuits*, vol. 54, no. 2, pp. 323–335, 2019.
- [56] R. Chen and H. Hashemi, “A 0.5-to-3 GHz Software-Defined Radio Receiver Using Discrete-Time RF Signal Processing,” *IEEE J. Solid-State Circuits*, vol. 49, no. 5, pp. 1097–1111, 2014.
- [57] P. Song and H. Hashemi, “mm-Wave Mixer-First Receiver with Passive Elliptic Low-Pass Filter,” in *IEEE Radio Frequency Integrated Circuits Symposium (RFIC) Dig.*, 2020.

- [58] J. C. Rudell, J. .-. Ou, T. B. Cho, *et al.*, “A 1.9-GHz wide-band IF double conversion CMOS receiver for cordless telephone applications,” *IEEE J. Solid-State Circuits*, vol. 32, no. 12, pp. 2071–2088, 1997.
- [59] A. Mirzaei, H. Darabi, and D. Murphy, “A Low-Power Process-Scalable Super-Heterodyne Receiver With Integrated High-Q Filters,” *IEEE J. Solid-State Circuits*, vol. 46, no. 12, pp. 2920–2932, 2011.
- [60] I. Madadi, M. Tohidian, K. Cornelissens, P. Vandenameele, and R. B. Staszewski, “A High IIP2 SAW-Less Superheterodyne Receiver With Multistage Harmonic Rejection,” *IEEE J. Solid-State Circuits*, vol. 51, no. 2, pp. 332–347, 2016.
- [61] M. C. M. Soer, E. A. M. Klumperink, Z. Ru, F. E. van Vliet, and B. Nauta, “A 0.2-to-2.0GHz 65nm CMOS receiver without LNA achieving $\gg 11$ dBm IIP3 and $\ll 6.5$ dB NF,” in *IEEE Int. Solid-State Circuits Conf. (ISSCC) Dig. Tech. Papers*, 2009, 222–223, 223a.
- [62] A. A. Abidi, “Direct-conversion radio transceivers for digital communications,” *IEEE J. Solid-State Circuits*, vol. 30, no. 12, pp. 1399–1410, 1995.
- [63] H. Hedayati, M. Darvishi, J. D. Dunworth, and F. Sabouri, “High rejection wideband bandpass N-path filter,” *U.S. Patent US10128819B2*, 2018.
- [64] J. A. Weldon, R. S. Narayanaswami, J. C. Rudell, *et al.*, “A 1.75-GHz highly integrated narrow-band CMOS transmitter with harmonic-rejection mixers,” *IEEE J. Solid-State Circuits*, vol. 36, no. 12, pp. 2003–2015, 2001.
- [65] A. Mirzaei and H. Darabi, “Analysis of Imperfections on Performance of 4-Phase Passive-Mixer-Based High-Q Bandpass Filters in SAW-Less Receivers,” *IEEE Trans. Circuits Syst. I: Reg. Papers*, vol. 58, no. 5, pp. 879–892, 2011.
- [66] *SAW filter B3519 Data Sheet*, München, Germany: Qualcomm RF360.
- [67] *The piezoelectric vibrator: Definitions and methods of measurements*, IRE 14.S1, 1957: IRE Standards on Piezoelectric crystals.
- [68] R. Hartley, “Modulation system,” in *U.S. Patent 1 666 206*, 1928.
- [69] I. Aoki, S. D. Kee, D. B. Rutledge, and A. Hajimiri, “Distributed active transformer-a new power-combining and impedance-transformation technique,” *IEEE Trans. Microw. Theory and Techn.*, vol. 50, no. 1, pp. 316–331, 2002.
- [70] D. Yang, C. Andrews, and A. Molnar, “Optimized Design of N-Phase Passive Mixer-First Receivers in Wideband Operation,” *IEEE Trans. Circuits Syst. I: Reg. Papers*, vol. 62, no. 11, pp. 2759–2770, 2015.

- [71] A. R. Shahani, D. K. Shaeffer, and T. H. Lee, “A 12-mW wide dynamic range CMOS front-end for a portable GPS receiver,” *IEEE J. Solid-State Circuits*, vol. 32, no. 12, pp. 2061–2070, 1997.
- [72] G. Qi, B. van Liempd, P. Mak, R. P. Martins, and J. Craninckx, “A SAW-Less Tunable RF Front End for FDD and IBFD Combining an Electrical-Balance Duplexer and a Switched-LC N-Path LNA,” *IEEE J. Solid-State Circuits*, vol. 53, no. 5, pp. 1431–1442, 2018.
- [73] A. Nagulu, T. Chen, G. Zussman, and H. Krishnaswamy, “29.3 Non-Magnetic 0.18 μ m SOI Circulator with Multi-Watt Power Handling Based on Switched-Capacitor Clock Boosting,” in *IEEE Int. Solid-State Circuits Conf. (ISSCC) Dig. Tech. Papers*, 2020, pp. 444–446.
- [74] A. Nagulu and H. Krishnaswamy, “Non-Magnetic CMOS Switched-Transmission-Line Circulators With High Power Handling and Antenna Balancing: Theory and Implementation,” *IEEE J. Solid-State Circuits*, vol. 54, no. 5, pp. 1288–1303, 2019. DOI: [10.1109/JSSC.2019.2905146](https://doi.org/10.1109/JSSC.2019.2905146).
- [75] D. Murphy, A. Mirzaei, H. Darabi, M. F. Chang, and A. Abidi, “An LTV Analysis of the Frequency Translational Noise-Cancelling Receiver,” *IEEE Trans. Circuits Syst. I: Reg. Papers*, vol. 61, no. 1, pp. 266–279, 2014.
- [76] R. Chen and H. Hashemi, “Passive coupled-switched-capacitor-resonator-based reconfigurable RF front-end filters and duplexers,” in *IEEE Radio Frequency Integrated Circuits Symposium (RFIC) Dig.*, 2016, pp. 138–141.
- [77] S. Hameed and S. Pamarti, “Design and Analysis of a Programmable Receiver Front End With Time-Interleaved Baseband Analog-FIR Filtering,” *IEEE J. Solid-State Circuits*, vol. 53, no. 11, pp. 3197–3207, 2018.
- [78] H. Seo, M. Sha, and J. Zhou, “A 3.5-to-6.2-GHz Mixer-First Acoustic-Filtering Chipset with Mixed-Domain Asymmetric IF and Complex BB Recombination Achieving 170 MHz BW and +27 dBm IIP3 at 1xBW offset,” in *IEEE Radio Frequency Integrated Circuits Symposium (RFIC) Dig.*, 2021.
- [79] H. Seo, M. Sha, and J. Zhou, “A passive-mixer-first acoustic-filtering chipset using mixed-domain recombination,” *IEEE Transactions on Microwave Theory and Techniques*, vol. 70, no. 7, pp. 3346–3360, 2022. DOI: [10.1109/TMTT.2022.3156053](https://doi.org/10.1109/TMTT.2022.3156053).
- [80] S. Bu, S. Hameed, and S. Pamarti, “Periodically Time-Varying Noise Cancellation for Filtering-by-Aliasing Receiver Front Ends,” *IEEE J. Solid-State Circuits*, vol. 56, no. 3, 2021.

- [81] Q. Wu, X. Zou, S. Qin, and Y. E. Wang, "Frequency translational RF receiver with time varying transmission lines (TVTL)," in *IEEE MTT-S Int. Microwave Symposium (IMS)*, 2017, pp. 1767–1769.
- [82] M. Hedayati, L. K. Yeung, M. Panahi, X. Zou, and Y. E. Wang, "Parametric Down-converter for Mixer-First Receiver Front Ends," *IEEE Trans. Microw. Theory and Techn.*, vol. 69, no. 5, pp. 2712–2721, 2021.
- [83] K. Badiyari, N. Nallam, and S. Chatterjee, "An N-Path Band-Pass Filter With Parametric Gain-Boosting," *IEEE Trans. Circuits Syst. I: Reg. Papers*, vol. 66, no. 10, pp. 3700–3712, 2019.
- [84] S. Gong, R. Lu, Y. Yang, L. Gao, and A. E. Hassanien, "Microwave Acoustic Devices: Recent Advances and Outlook," *IEEE J. Microw.*, vol. 1, no. 2, pp. 601–609, 2021.
- [85] F. Z. Bi and B. P. Barber, "Bulk acoustic wave RF technology," *IEEE Microw. Mag.*, vol. 9, no. 5, pp. 65–80, 2008.
- [86] *RF front-end (RFFE) filters: 313.85MHz SAW Filter B39311B3768Z810*, San Diego, CA: Qualcomm.
- [87] *165 MHz SAW filter SF2170D*, Carrollton, TX: RFMi.
- [88] K.-Y. Hashimoto, T. Kimura, T. Matsumura, *et al.*, "Moving Tunable Filters Forward: A "Heterointegration" Research Project for Tunable Filters Combining MEMS and RF SAW/BAW Technologies," *IEEE Microw. Mag.*, vol. 16, no. 7, pp. 89–97, 2015.
- [89] T. H. Lee, *The Design of CMOS Radio-Frequency Integrated Circuits, Second Edition*. Cambridge, United Kingdom: Cambridge University Press, 2003.
- [90] C. Andrews and A. C. Molnar, "Implications of Passive Mixer Transparency for Impedance Matching and Noise Figure in Passive Mixer-First Receivers," *IEEE Trans. Circuits Syst. I: Reg. Papers*, vol. 57, no. 12, pp. 3092–3103, 2010.
- [91] S. Gong and G. Piazza, "Design and Analysis of Lithium–Niobate-Based High Electromechanical Coupling RF-MEMS Resonators for Wideband Filtering," *IEEE Trans. Microw. Theory and Techn.*, vol. 61, no. 1, pp. 403–414, 2013.
- [92] T.-H. Wu and C. Meng, "5.2/5.7-GHz 48-dB Image Rejection GaInP/GaAs HBT Weaver Down-Converter Using LO Frequency Quadrupler," *IEEE J. Solid-State Circuits*, vol. 41, no. 11, pp. 2468–2480, 2006.
- [93] L. Sundstrom, M. Anderson, R. Strandberg, *et al.*, "A receiver for LTE Rel-11 and beyond supporting non-contiguous carrier aggregation," in *IEEE Int. Solid-State Circuits Conf. (ISSCC) Dig. Tech. Papers*, 2013, pp. 336–337.

- [94] L. Gao, Q. Ma, and G. M. Rebeiz, “A 20–44-GHz Image-Rejection Receiver With 75-dB Image-Rejection Ratio in 22-nm CMOS FD-SOI for 5G Applications,” *IEEE Trans. Microw. Theory and Techn.*, vol. 68, no. 7, pp. 2823–2832, 2020.
- [95] J. Lee, B. Kang, S. Joo, *et al.*, “6.1 A Low-Power and Low-Cost 14nm FinFET RFIC Supporting Legacy Cellular and 5G FR1,” in *IEEE Int. Solid-State Circuits Conf. (ISSCC) Dig. Tech. Papers*, vol. 64, 2021, pp. 90–92.
- [96] S. Hwu and B. Razavi, “An RF Receiver for Intra-Band Carrier Aggregation,” *IEEE J. Solid-State Circuits*, vol. 50, no. 4, pp. 946–961, 2015.
- [97] J. Zhou, T.-H. Chuang, T. Dinc, and H. Krishnaswamy, “Integrated wideband self-interference cancellation in the RF domain for FDD and full-duplex wireless,” *IEEE J. Solid-State Circuits*, vol. 50, no. 12, pp. 3015–3031, Dec. 2015.
- [98] D.-J. van den Broek, E. A. M. Klumperink, and B. Nauta, “An In-Band Full-Duplex Radio Receiver With a Passive Vector Modulator Downmixer for Self-Interference Cancellation,” *IEEE J. Solid-State Circuits*, vol. 50, no. 12, pp. 3003–3014, 2015. DOI: [10.1109/JSSC.2015.2482495](https://doi.org/10.1109/JSSC.2015.2482495).
- [99] Y. Cao, X. Cao, H. Seo, and J. Zhou, “An Integrated Full-Duplex/FDD Duplexer and Receiver Achieving 100MHz Bandwidth 58dB/48dB Self-Interference Suppression Using Hybrid-Analog-Digital Autonomous Adaptation Loops,” in *IEEE MTT-S Int. Microwave Symposium (IMS)*, 2020, pp. 1203–1206.
- [100] A. Nagulu, S. Garikapati, M. Essawy, *et al.*, “6.6 Full-Duplex Receiver with Wideband Multi-Domain FIR Cancellation Based on Stacked-Capacitor, N-Path Switched-Capacitor Delay Lines Achieving >54dB SIC Across 80MHz BW and >15dBm TX Power-Handling,” in *IEEE Int. Solid-State Circuits Conf. (ISSCC) Dig. Tech. Papers*, vol. 64, 2021, pp. 100–102.
- [101] R. Michaelsen, T. Johansen, and K. Tamborg, “Investigation of LO-leakage cancellation and DC-offset influence on flicker-noise in X-band mixers,” in *Proc. Eur. Microw. Integr. Circuits Conf. (EuMIC)*, 2012, pp. 99–102.
- [102] J. Zhou, A. Chakrabarti, P. R. Kinget, and H. Krishnaswamy, “Low-Noise Active Cancellation of Transmitter Leakage and Transmitter Noise in Broadband Wireless Receivers for FDD/Co-Existence,” *IEEE J. Solid-State Circuits*, vol. 49, no. 12, pp. 3046–3062, 2014.
- [103] Y. Lien, E. Klumperink, B. Tenbroek, J. Strange, and B. Nauta, “24.3 A high-linearity CMOS receiver achieving +44dBm IIP3 and +13dBm B1dB for SAW-less LTE radio,” in *IEEE Int. Solid-State Circuits Conf. (ISSCC) Dig. Tech. Papers*, 2017, pp. 412–413.

- [104] H. Seo, S. B. Karnoor, and R. R. Choudhury, *Ross: Utilizing robotic rotation for audio source separation*, 2022. DOI: [10.48550/ARXIV.2203.10072](https://arxiv.org/abs/2203.10072). [Online]. Available: <https://arxiv.org/abs/2203.10072>.
- [105] H. G. Okuno and K. Nakadai, “Robot audition: Its rise and perspectives,” in *2015 IEEE International Conference on Acoustics, Speech and Signal Processing (ICASSP)*, 2015, pp. 5610–5614. DOI: [10.1109/ICASSP.2015.7179045](https://doi.org/10.1109/ICASSP.2015.7179045).
- [106] T. Mizumoto, K. Nakadai, T. Yoshida, *et al.*, “Design and implementation of selectable sound separation on the texai telepresence system using hark,” in *2011 IEEE International Conference on Robotics and Automation*, 2011, pp. 2130–2137. DOI: [10.1109/ICRA.2011.5979849](https://doi.org/10.1109/ICRA.2011.5979849).
- [107] I. Hara, F. Asano, H. Asoh, *et al.*, “Robust speech interface based on audio and video information fusion for humanoid hrp-2,” in *2004 IEEE/RSJ International Conference on Intelligent Robots and Systems (IROS)*, vol. 3, 2004, 2404–2410 vol.3. DOI: [10.1109/IROS.2004.1389768](https://doi.org/10.1109/IROS.2004.1389768).
- [108] A. Hyvärinen, J. Karhunen, and E. Oja, “Independent component analysis,” Wiley, vol. VII, 2001.
- [109] T. Kim, H. T. Attias, S.-Y. Lee, and T.-W. Lee, “Blind source separation exploiting higher-order frequency dependencies,” *IEEE Transactions on Audio, Speech, and Language Processing*, vol. 15, no. 1, pp. 70–79, 2007. DOI: [10.1109/TASL.2006.872618](https://doi.org/10.1109/TASL.2006.872618).
- [110] O. Frost, “An algorithm for linearly constrained adaptive array processing,” *Proceedings of the IEEE*, vol. 60, no. 8, pp. 926–935, 1972. DOI: [10.1109/PROC.1972.8817](https://doi.org/10.1109/PROC.1972.8817).
- [111] K. Nakadai, H. Nakajima, G. Ince, and Y. Hasegawa, “Sound source separation and automatic speech recognition for moving sources,” in *2010 IEEE/RSJ International Conference on Intelligent Robots and Systems*, 2010, pp. 976–981. DOI: [10.1109/IROS.2010.5651167](https://doi.org/10.1109/IROS.2010.5651167).
- [112] M. Heckmann, F. Joublin, and E. Korner, “Sound source separation for a robot based on pitch,” in *2005 IEEE/RSJ International Conference on Intelligent Robots and Systems*, 2005, pp. 2197–2202. DOI: [10.1109/IROS.2005.1544982](https://doi.org/10.1109/IROS.2005.1544982).
- [113] K. Noda, N. Hashimoto, K. Nakadai, and T. Ogata, “Sound source separation for robot audition using deep learning,” in *2015 IEEE-RAS 15th International Conference on Humanoid Robots (Humanoids)*, 2015, pp. 389–394. DOI: [10.1109/HUMANOIDS.2015.7363579](https://doi.org/10.1109/HUMANOIDS.2015.7363579).
- [114] Y. Luo and N. Mesgarani, “Tasnet: Time-domain audio separation network for real-time, single-channel speech separation,” in *ICASSP*, 2018.

- [115] M. Maazaoui, K. Abed-Meraim, and Y. Grenier, “Blind source separation for robot audition using fixed hrtf beamforming,” *EURASIP Journal on Advances in Signal Processing*, vol. 2012, no. 1, p. 58, Mar. 2012. DOI: [10.1186/1687-6180-2012-58](https://doi.org/10.1186/1687-6180-2012-58).
- [116] O. Yilmaz and S. Rickard, “Blind separation of speech mixtures via time-frequency masking,” *IEEE Transactions on Signal Processing*, vol. 52, no. 7, pp. 1830–1847, 2004.
- [117] A. Deleforge, F. Forbes, and R. Horaud, “Acoustic space learning for sound-source separation and localization on binaural manifolds,” *International Journal of Neural Systems*, vol. 25, no. 01, p. 1440003, 2015, PMID: 25164245. DOI: [10.1142/S0129065714400036](https://doi.org/10.1142/S0129065714400036).
- [118] E. Nachmani, Y. Adi, and L. Wolf, “Voice separation with an unknown number of multiple speakers,” in *International Conference on Machine Learning*, 2020.
- [119] J. Yang, Y. Guo, Z. Yang, and S. Xie, “Under-determined convolutive blind source separation combining density-based clustering and sparse reconstruction in time-frequency domain,” *IEEE Transactions on Circuits and Systems I: Regular Papers*, pp. 3015–3027, 2019. DOI: [10.1109/TCSI.2019.2908394](https://doi.org/10.1109/TCSI.2019.2908394).
- [120] Y. Luo and N. Mesgarani, “Conv-tasnet: Surpassing ideal time-frequency magnitude masking for speech separation,” in *IEEE/ACM transactions on audio, speech, and language processing*, 2019.
- [121] S. Miyabe, B.-H. Juang, H. Saruwatari, and K. Shikano, “Kernel-based nonlinear independent component analysis for underdetermined blind source separation,” in *2009 IEEE International Conference on Acoustics, Speech and Signal Processing*, 2009, pp. 1641–1644.
- [122] G. F. Edelmann and C. F. Gaumont, “Beamforming using compressed sensing,” *The Journal of Acoustic Society of America*, 2011.
- [123] H. Sawada, N. Ono, H. Kameoka, D. Kitamura, and H. Saruwatari, “A review of blind source separation methods: Two converging routes to ilrma originating from ica and nmf,” *APSIPA Transactions on Signal and Information Processing*, vol. 8, e12, 2019. DOI: [10.1017/ATSIP.2019.5](https://doi.org/10.1017/ATSIP.2019.5).
- [124] C. Rascon and I. Meza, “Localization of sound sources in robotics: A review,” *Robotics and Autonomous Systems*, vol. 96, pp. 184–210, 2017, ISSN: 0921-8890.
- [125] E. Vincent, A. Sini, and F. Charpillat, “Audio source localization by optimal control of a mobile robot,” in *2015 IEEE International Conference on Acoustics, Speech and Signal Processing (ICASSP)*, 2015, pp. 5630–5634. DOI: [10.1109/ICASSP.2015.7179049](https://doi.org/10.1109/ICASSP.2015.7179049).

- [126] K. Nakamura, K. Nakadai, F. Asano, and G. Ince, “Intelligent sound source localization and its application to multimodal human tracking,” in *2011 IEEE/RSJ International Conference on Intelligent Robots and Systems*, 2011, pp. 143–148. DOI: [10.1109/IROS.2011.6094558](https://doi.org/10.1109/IROS.2011.6094558).
- [127] J.-M. Valin, F. Michaud, B. Hadjou, and J. Rouat, “Localization of simultaneous moving sound sources for mobile robot using a frequency- domain steered beamformer approach,” in *IEEE International Conference on Robotics and Automation, 2004. Proceedings. ICRA '04. 2004*, vol. 1, 2004, 1033–1038 Vol.1. DOI: [10.1109/ROBOT.2004.1307286](https://doi.org/10.1109/ROBOT.2004.1307286).
- [128] X. Li, H. Liu, and X. Yang, “Sound source localization for mobile robot based on time difference feature and space grid matching,” in *2011 IEEE/RSJ International Conference on Intelligent Robots and Systems*, 2011, pp. 2879–2886. DOI: [10.1109/IROS.2011.6094667](https://doi.org/10.1109/IROS.2011.6094667).
- [129] J. L. Roux, S. Wisdom, H. Erdogan, and J. R. Hershey, “Sdr-half-baked or well done?” In *ICASSP*, 2019.
- [130] H. Pishro-Nik, *Introduction to Probability, Statistics, and Random Processes*. Kappa Research, LLC, 2014, ISBN: 9780990637202. [Online]. Available: https://books.google.com/books?id=3yq%5C_oQEACAAJ.
- [131] *Respeaker 6 mic circular array kit for raspberry pi*. [Online]. Available: <https://wiki.seeedstudio.com/>.
- [132] H. Zen, V. Dang, R. Clark, *et al.*, “Libritts: A corpus derived from librispeech for text-to-speech,” *arXiv preprint arXiv:1904.02882*, 2019.
- [133] E. Habets, *Ehabets/rir-generator: Rir generator*, version v2.1.20141124, Oct. 2020. DOI: [10.5281/zenodo.4096349](https://doi.org/10.5281/zenodo.4096349). [Online]. Available: <https://github.com/ehabets/RIR-Generator>.
- [134] M. Maciejewski, J. Shi, S. Watanabe, and S. Khudanpur, “Training noisy single-channel speech separation with noisy oracle sources: A large gap and a small step,” in *ICASSP*, 2021.
- [135] S. Majumder, Z. Al-Halah, and K. Grauman, “Move2hear: Active audio-visual source separation,” in *Proceedings of the IEEE/CVF International Conference on Computer Vision (ICCV)*, Oct. 2021, pp. 275–285.

- [136] C. Gan, Y. Zhang, J. Wu, B. Gong, and J. B. Tenenbaum, “Look, listen, and act: Towards audio-visual embodied navigation,” in *2020 IEEE International Conference on Robotics and Automation (ICRA)*, 2020, pp. 9701–9707. DOI: [10.1109/ICRA40945.2020.9197008](https://doi.org/10.1109/ICRA40945.2020.9197008).
- [137] A. Krizhevsky, I. Sutskever, and G. E. Hinton, “Imagenet classification with deep convolutional neural networks,” in *Advances in Neural Information Processing Systems*, F. Pereira, C. J. C. Burges, L. Bottou, and K. Q. Weinberger, Eds., vol. 25, Curran Associates, Inc., 2012. [Online]. Available: <https://proceedings.neurips.cc/paper/2012/file/c399862d3b9d6b76c8436e924a68c45b-Paper.pdf>.
- [138] J. Feldmann, N. Youngblood, C. D. Wright, and et al., “All-optical spiking neurosynaptic networks with self-learning capabilities,” *Nature*, 2019.
- [139] T. F. de Lima, B. J. Shastri, A. N. T. ad Mitchell A. Nahmias, and P. R. Prucnal, “Progress in neuromorphic photonics,” *Nanophotonics*, 2017.
- [140] S. C. Iris Cong and M. D. Lukin, “Quantum convolutional neural networks,” *Nature Physics*, 2019.
- [141] L. Jung S., S. H. Myung, and et al., “A crossbar array of magnetoresistive memory devices for in-memory computing,” *Nature*, vol. 601, pp. 211–216, 2022. DOI: <https://doi.org/10.1038/s41586-021-04196-6>.
- [142] H. Song, S. Oh, J. Salinas, S.-Y. Park, and E. Yoon, “A 5.1ms low-latency face detection imager with in-memory charge-domain computing of machine-learning classifiers,” in *2021 Symposium on VLSI Circuits*, 2021, pp. 1–2. DOI: [10.23919/VLSICircuits52068.2021.9492432](https://doi.org/10.23919/VLSICircuits52068.2021.9492432).
- [143] M. Lefebvre, L. Moreau, R. Dekimpe, and D. Bol, “7.7 a 0.2-to-3.6tops/w programmable convolutional imager soc with in-sensor current-domain ternary-weighted mac operations for feature extraction and region-of-interest detection,” in *2021 IEEE International Solid-State Circuits Conference (ISSCC)*, vol. 64, 2021, pp. 118–120. DOI: [10.1109/ISSCC42613.2021.9365839](https://doi.org/10.1109/ISSCC42613.2021.9365839).
- [144] Z. Wang, J. Zhang, and N. Verma, “Realizing low-energy classification systems by implementing matrix multiplication directly within an adc,” *IEEE Transactions on Biomedical Circuits and Systems*, vol. 9, no. 6, pp. 825–837, 2015. DOI: [10.1109/TBCAS.2015.2500101](https://doi.org/10.1109/TBCAS.2015.2500101).
- [145] E. H. Lee and S. S. Wong, “Analysis and design of a passive switched-capacitor matrix multiplier for approximate computing,” *IEEE Journal of Solid-State Circuits*, vol. 52, no. 1, pp. 261–271, 2017. DOI: [10.1109/JSSC.2016.2599536](https://doi.org/10.1109/JSSC.2016.2599536).

- [146] Y. Cao, X. Cao, H. Seo, and J. Zhou, “An integrated full-duplex/fdd duplexer and receiver achieving 100mhz bandwidth 58db/48db self-interference suppression using hybrid-analog-digital autonomous adaptation loops,” in *2020 IEEE/MTT-S International Microwave Symposium (IMS)*, 2020, pp. 1203–1206. DOI: [10.1109/IMS30576.2020.9223872](https://doi.org/10.1109/IMS30576.2020.9223872).
- [147] D. J. Frank, S. Chakraborty, K. Tien, *et al.*, “A cryo-cmos low-power semi-autonomous qubit state controller in 14nm finfet technology,” in *2022 IEEE International Solid-State Circuits Conference (ISSCC)*, vol. 65, 2022, pp. 360–362. DOI: [10.1109/ISSCC42614.2022.9731538](https://doi.org/10.1109/ISSCC42614.2022.9731538).
- [148] J. P. G. Van Dijk, B. Patra, S. Subramanian, *et al.*, “A scalable cryo-cmos controller for the wideband frequency-multiplexed control of spin qubits and transmons,” *IEEE Journal of Solid-State Circuits*, vol. 55, no. 11, pp. 2930–2946, 2020. DOI: [10.1109/JSSC.2020.3024678](https://doi.org/10.1109/JSSC.2020.3024678).
- [149] M. Z. Koohi, S. Nam, and A. Mortazawi, “Intrinsically switchable and bandwidth reconfigurable ferroelectric bulk acoustic wave filters,” *IEEE Transactions on Ultrasonics, Ferroelectrics, and Frequency Control*, vol. 67, no. 5, pp. 1025–1032, 2020. DOI: [10.1109/TUFFC.2019.2958675](https://doi.org/10.1109/TUFFC.2019.2958675).
- [150] G. Han, T. Haque, M. Bajor, J. Wright, and P. R. Kinget, “A 0.3-to-1.3ghz multi-branch receiver with modulated mixer clocks for concurrent dual-carrier reception and rapid compressive-sampling spectrum scanning,” in *2019 IEEE Radio Frequency Integrated Circuits Symposium (RFIC)*, 2019, pp. 95–98. DOI: [10.1109/RFIC.2019.8701751](https://doi.org/10.1109/RFIC.2019.8701751).
- [151] G. Han, T. Haque, M. Bajor, J. Wright, and P. R. Kinget, “A multi-branch receiver with modulated mixer clocks for concurrent dual-carrier reception and rapid compressive-sampling spectrum scanning,” *IEEE Journal of Solid-State Circuits*, vol. 56, no. 1, pp. 235–253, 2021. DOI: [10.1109/JSSC.2020.3014063](https://doi.org/10.1109/JSSC.2020.3014063).
- [152] H. Seo and J. Zhou, “Periodically switched acoustic-filtering rf front-ends using commutated-lc circuits for wireless receivers,” in *2022 IEEE 22nd Annual Wireless and Microwave Technology Conference (WAMICON)*, 2022, pp. 1–4. DOI: [10.1109/WAMICON53991.2022.9786200](https://doi.org/10.1109/WAMICON53991.2022.9786200).

Appendix A

Derivation of full equation solution with general LTI impedance response

Here, we derive the RF input impedance Z_{in} of a mixer-first front-end with a load impedance $Z_L(f)$ that is not limited to a low-pass frequency response and could have significant impedance components at LO harmonic frequencies [33]

Consider an N-path mixer-first front-end in Fig. 2.7(a). The RF voltage V_{in} can be written as [65]

$$V_{in}(\omega) = R_{SW}I_S(\omega) + N \sum_{n=-\infty}^{\infty} \sum_{m=-\infty}^{\infty} a_n a_m \times I_S(\omega - (n+m)\omega_{LO}) Z_L(\omega - n\omega_{LO}), \quad (\text{A.1})$$

where N is the number of paths and $a_n = \frac{\text{sinc}(\frac{n\pi}{N})}{N} e^{-j\frac{n\pi}{N}}$. Applying KVL at the input, V_{in} can be also calculated as

$$V_{in}(\omega) = V_S(\omega) - R_S I_S(\omega). \quad (\text{A.2})$$

Assuming that the frequency components of an input signal in the desired frequency band $V_S(\omega)$ are confined to be between $\omega_{IF} + \omega_{LO}/2$ and $\omega_{IF} + 3\omega_{LO}/2$, $V_S(\omega)$ can be written as

$$V_S(\omega) = V_{S,1,-}(\omega + \omega_{LO}) + V_{S,1,+}(\omega - \omega_{LO}), \quad (\text{A.3})$$

where $V_{S,1,+}(\omega)$ and $V_{S,1,-}(\omega)$ are two complex IF signals representing portions of the spectrum of that center around $+\omega_{IF}$ and $-\omega_{IF}$, respectively. Given the LPTV nature of the system, $I_S(\omega)$ can be expressed in terms of a summation of frequency-shifted complex IF signals

around LO harmonics:

$$\begin{aligned}
I_S(\omega) &= \sum_{n=-\infty}^{\infty} I_{S,n}(\omega) \\
&= \sum_{n=-\infty}^{\infty} [I_{S,n,-}(\omega + n\omega_{LO}) + I_{S,n,+}(\omega - n\omega_{LO})],
\end{aligned} \tag{A.4}$$

where $I_{S,n,+}(\omega)$ and $I_{S,n,-}(\omega)$ are two complex IF signals representing portions of the spectrum of that center around $+n\omega_{IF}$ and $-n\omega_{IF}$, respectively.

Substituting (A.2), (A.3), and (A.4) into (A.1), we have

$$\begin{aligned}
&V_{S,1,-}(\omega + \omega_{LO}) + V_{S,1,+}(\omega - \omega_{LO}) \\
&= R'_S \sum_{n=-\infty}^{\infty} (I_{S,n,-}(\omega + n\omega_{LO}) + I_{S,n,+}(\omega - n\omega_{LO})) \\
&+ N \sum_{n=-\infty}^{\infty} \sum_{k=-\infty}^{\infty} \sum_{m=-\infty}^{\infty} a_n a_{Nk-n} Z_L(\omega - n\omega_{LO}) \times \\
&[I_{S,m,-}(\omega + (m - Nk)\omega_{LO}) + I_{S,m,+}(\omega - (m + Nk)\omega_{LO})],
\end{aligned} \tag{A.5}$$

where $R'_S = R_S + R_{SW}$.

Assuming $2f_{IF}$ is not integer multiples of f_{LO} as we discussed in Section III and $Z_L(\omega)$ has a band-pass frequency response with significant impedance only around $\pm\omega_{IF}$, (A.5) can be simplified as

$$\begin{aligned}
&V_{S,1,-}(\omega + \omega_{LO}) + V_{S,1,+}(\omega - \omega_{LO}) \\
&= R'_S \sum_{n=-\infty}^{\infty} (I_{S,n,-}(\omega + n\omega_{LO}) + I_{S,n,+}(\omega - n\omega_{LO})) \\
&+ N \sum_{n=-\infty}^{\infty} \sum_{k=-\infty}^{\infty} a_n a_{Nk-n} Z_L(\omega - n\omega_{LO}) \times \\
&[I_{S,Nk-n,-}(\omega - n\omega_{LO}) + I_{S,-(Nk-n),+}(\omega - n\omega_{LO})].
\end{aligned} \tag{A.6}$$

This is because unless harmonic currents $I_{S,m,-}$ and $I_{S,m,+}$ are aligned with the impedance peak around $n\omega_{LO}$, the resultant voltages can be neglected. Given the assumption that $Z_L(\omega)$ has a band-pass frequency response with significant impedance only around $\pm\omega_{IF}$ and $2f_{IF}$

is not integer multiples of f_{LO} , (A.6) is similar to that in a direct-conversion zero/low-IF mixer-first front-end [65]. Using the procedures outlined in [65], (2.1) and (2.2) in Section III-A can be obtained.

As discussed in Section III, when loaded with high-order acoustic filters, Z_L components outside of $\pm\omega_{IF}$ can be significant. Harmonic currents flow into these impedance components creating impedance aliasing. Let us consider the general case where $M + 1$ harmonic currents see significant IF impedance, (A.6) can be modified as

$$\begin{aligned}
& V_{S,1,-}(\omega + \omega_{LO}) + V_{S,1,+}(\omega - \omega_{LO}) \\
&= R'_S \sum_{n=-\infty}^{\infty} (I_{S,n,-}(\omega + n\omega_{LO}) + I_{S,n,+}(\omega - n\omega_{LO})) \\
&+ N \sum_{n=-\infty}^{\infty} \sum_{k=-\infty}^{\infty} a_n a_{Nk-n} Z_L(\omega - n\omega_{LO}) \times \\
&\sum_{i=0}^M [I_{S,Nk-n+p_i,-}(\omega - (n - p_i)\omega_{LO}) + \\
&I_{S,-(Nk-n-p_i),+}(\omega - (n + p_i)\omega_{LO})],
\end{aligned} \tag{A.7}$$

where a single pair of harmonic currents in (A.6) is replaced with $M + 1$ pairs of harmonic currents that see significant Z_L components outside of $\pm\omega_{IF}$. i is the index of Z_L at p_i -th LO harmonic. Assuming there is always impedance at the desired IF, we have $p_0 = 0$.

Since $V_S(\omega)$ only has components around $\omega_{IF} + \omega_{LO}$ and $I_{S,n}(\omega)$ is bounded between $\omega_{IF} + (2n - 1)\omega_{LO}/2$ and $\omega_{IF} + (2n + 1)\omega_{LO}/2$ based on its definition given in (A.4), (A.7) can be simplified and split into two parts as

$$\begin{aligned}
& V_{S,n,+}(\omega - n\omega_{LO}) \\
&= R'_S I_{S,n,+}(\omega - n\omega_{LO}) \\
&+ N \sum_{i=0}^M a_{n-i} Z_{IF}(\omega - (n - p_i)\omega_{LO}) I_{S,sum}(\omega, n, i),
\end{aligned} \tag{A.8}$$

$$\begin{aligned}
& V_{S,n,-}(\omega + n\omega_{LO}) \\
&= R'_S I_{S,n,-}(\omega + n\omega_{LO}) \\
&+ N \sum_{i=0}^M a_{-(n-i)} Z_{IF}(\omega + (n - p_i)\omega_{LO}) I_{S,sum}(\omega, -n, i),
\end{aligned} \tag{A.9}$$

where $I_{S,sum}(\omega, n, i)$ is a weighted currents sum corresponding to the Z_L at p_i -th LO harmonic:

$$I_{S,sum}(\omega, n, i) = \sum_{k=-\infty}^{\infty} a_{Nk-n+i} I_{s,-(Nk-n),+}(\omega - n\omega_{LO}). \quad (\text{A.10})$$

Also, in (A.8) and (A.9), $V_{s,n,\pm}(\omega) = V_{s,1,\pm}(\omega)$ when $n = 1$; otherwise, $V_{s,n,\pm}(\omega) = 0$. Let us focus on (A.8) only as $v_S(t)$ and $i_S(t)$ are real signals and hence $V_{S,n,-}(\omega) = V_{S,-n,-}^*(-\omega)$ and $I_{S,n,-}(\omega) = I_{S,-n,-}^*(-\omega)$.

In (A.8), the weighted currents sum $I_{S,sum}(\omega, n, i)$ is evidently periodic with respect to n with a period of N . Hence, we may replace n in (A.8) with $n = -(Nk - n)$. Also, making a notation change of $\omega - n\omega_{LO} = \omega$, (A.8) becomes

$$\begin{aligned} & V_{S,-(Nk-n),+}(\omega) \\ &= R'_S I_{S,-(Nk-n),+}(\omega) + \\ & N \sum_{i=0}^M a_{-(Nk-n+i)} Z_{IF}(\omega + i\omega_{LO}) I_{S,sum}(\omega + n\omega_{LO}, n, i). \end{aligned} \quad (\text{A.11})$$

Multiplying both sides of (A.11) by a_{Nk-n+i} and then taking the summation over entire integer values of k leads to:

$$\begin{aligned} & a_{-1+i} V_{S,1,+}(\omega) \\ &= R'_S I_{S,sum}(\omega + n\omega_{LO}, n, i) + N \sum_{k=-\infty}^{\infty} a_{Nk-n+i} \times \\ & \sum_{i=0}^M a_{-(Nk-n+i)} Z_{IF}(\omega + i\omega_{LO}) I_{S,sum}(\omega + n\omega_{LO}, n, i). \end{aligned} \quad (\text{A.12})$$

Using (A.12) and substituting i from 0 to M results in a matrix equation given as

$$[R'_S \mathbf{I} + \mathbf{Z}_M] \mathbf{I}_{S,sum} = V_{s,1,+}(\omega) \mathbf{a}, \quad (\text{A.13})$$

where \mathbf{I} is an identity matrix of size $M + 1$, the i -th row and j -th column element of $(M + 1)$ -by- $(M + 1)$ matrix \mathbf{Z}_M is

$$Z_{m,i,j} = Z_L(\omega + j\omega_{LO}) \sum_{k=-\infty}^{\infty} a_{-(Nk-n+i)} a_{-(Nk-n+j)}$$

,

$$\mathbf{I}_{S,\text{sum}}(\mathbf{n}, \omega) = [\mathbf{I}_{S,\text{sum}}(\omega + n\omega_{LO}, n, 0), I_{S,\text{sum}}(\omega + n\omega_{LO}, n, 1), \dots, I_{S,\text{sum}}(\omega + n\omega_{LO}, n, M)]^T \quad (\text{A.14})$$

and

$$\mathbf{a} = [a_{-1}, a_0, \dots, a_{M-1}]^T$$

Dividing both sides of (A.13) by $V_{s,1,+}(\omega)$ results in (2.6). Finally, by letting $n=1$ and replacing ω with $\omega - \omega_{LO}$ in (A.12), the input impedance can be expressed as in (2.4).

When there are two controlled impedance peaks in $Z_L(\omega)$, (2.4) can be solved analytically and the result is given in (A.15). In (A.15), $R_{sh,p} = (R_S + R_{SW}) \frac{N\gamma_p}{1-N\gamma_p}$, $Z_{L,p} = Z_L(\omega_S + p\omega_{LO})$, N is the number of paths,

$$\gamma_p = \frac{\text{sinc}^2(p\pi/N)}{N}$$

$$G_0 = \frac{\text{sinc}(\frac{\pi}{N})\text{sinc}(\frac{p}{N}\pi)}{N^2}$$

and

$$G_s = \sum_{k=-\infty}^{\infty} \frac{\text{sinc}(\frac{Nk-1}{N}\pi)\text{sinc}(\frac{Nk+p}{N}\pi)}{N^2}$$

$$\begin{aligned} & Z_{in,2peaks} \\ &= R_{SW} + \frac{\gamma_{-1}Z_{L,-1} + \gamma_p Z_{L,p} + \frac{\gamma_{-1}Z_{L,-1}\gamma_p Z_{L,p}}{R_{sh,p}R_{sh,-1}} + \frac{2N^2 G_0 Z_{L,-1} Z_{L,p}}{R_{SW} + R_S} (G_0 - G_s)}{1 + \frac{\gamma_{-1}Z_{L,-1}}{R_{sh,-1}} + \frac{\gamma_p Z_{L,p}}{R_{sh,p}} + \frac{\gamma_{-1}Z_{L,-1}\gamma_p Z_{L,p}}{R_{sh,p}R_{sh,-1}} - \frac{N^2 Z_{L,-1} Z_{L,p}}{(R_{SW} + R_S)^2} (G_0 - G_s)^2} \end{aligned} \quad (\text{A.15})$$

Appendix B

Frequency Planning for Optimal IF Frequency Selection for Super-heterodyne Architectures

This appendix chapter discusses about the logic behind choosing intermediate frequency f_{IF} which sets the center frequency of acoustic bandpass filter when desired RF tuning range is given in super-heterodyne receiver architectures [152]. Consider the scenario where RF signal frequency $f_S \in [f_{S,L}, f_{S,U}]$ where upper and lower bounds of tuning range is defined as $f_{S,U}$ and $f_{S,L}$ respectively. Now, tuning range amount Δf_S is given as:

$$\Delta f_S = f_{S,U} - f_{S,L} \quad (\text{B.1})$$

While we want to maximize our signal tuning range, there is image signal band that would limit the RF signal range because it would be indistinguishable if two bands, signal and image bands, overlap in spectral domain. Therefore, let us consider the case where we want to down-convert the RF signals sitting at upper side via LO signal f_{LO} while image band sits at lower side of f_{LO} ; thus, image signal frequency is given as $f_{IM} = |f_S - 2f_{IF}|$. Notice that $f_{IM} \leq f_S$ always holds and following optimization goal can be set.

- Maximize Δf_S while image band does not overlap with signal bands

\leftrightarrow maximize Δf_S such that $\max(f_{IM})$ is minimized.

$$\leftrightarrow f_{IF}^* = \operatorname{argmin}_{f_{IF}} \left(\max_{f_S \in [f_{S,U}, f_{S,L}]} |f_{IM}| \right) = \operatorname{argmin}_{f_{IF}} \left(\max_{f_S \in [f_{S,U}, f_{S,L}]} |f_S - 2f_{IF}| \right) \quad (\text{B.2})$$

From now, we prove that there exists unique analytical solution f_{IF}^* and apply these values for determining our IF frequencies.

First, let us expand the inner maximize operator part.

$$\begin{aligned}
\max_{f_S \in [f_{S,U}, f_{S,L}]} |f_S - 2f_{IF}| &= \max(|f_{S,L} - 2f_{IF}|, |f_{S,U} - 2f_{IF}|) \\
&= \max(|f_{S,L} - 2f_{IF}|^2, |f_{S,U} - 2f_{IF}|^2) \\
&= \frac{1}{2} \left((f_{S,L} - 2f_{IF})^2 + (f_{S,U} - 2f_{IF})^2 + |f_{S,L} + f_{S,U} - 4f_{IF}|(f_{S,L} - f_{S,U}) \right) \\
&= \left(\left| 2f_{IF} - \frac{f_{S,L} + f_{S,U}}{2} \right| + \frac{|f_{S,L} - f_{S,U}|}{2} \right)^2 \geq \left| 2f_{IF} - \frac{f_{S,L} + f_{S,U}}{2} \right|^2
\end{aligned} \tag{B.3}$$

Therefore, original objective equation (B.2) can be rewritten as follows yielding analytical solution to this ranged optimization problem.

$$\begin{aligned}
f_{IF}^* &= \operatorname{argmin}_{f_{IF}} \left(\max_{f_S \in [f_{S,U}, f_{S,L}]} |f_S - 2f_{IF}| \right) \\
&= \operatorname{argmin}_{f_{IF}} \left| 2f_{IF} - \frac{f_{S,L} + f_{S,U}}{2} \right|^2 \\
&= \frac{f_{S,L} + f_{S,U}}{4}
\end{aligned} \tag{B.4}$$

Now, by inserting optimal IF frequency value f_{IF}^* into equation (B.3) gives the condition below.

$$\begin{aligned}
\max_{f_S \in [f_{S,U}, f_{S,L}]} |f_S - 2f_{IF}^*| &= \frac{f_{S,U} - f_{S,L}}{2} \\
&= \frac{\Delta f_S}{2} \leq f_{S,L}
\end{aligned} \tag{B.5}$$

Therefore, in order to maximize RF tuning range Δf_S , it can only be maximized subject to $\Delta f_S \leq 2f_{S,L}$. in summary, optimal frequency planning condition to maximize Rf tuning range while avoiding collision with image band is given as (B.4) and (B.5).

As an example, for the target design RF tuning range of $f_S \in [2.5, 4.5]$ GHz, $f_{IF}^* = 1.75$ GHz, and 1.6 GHz off-the-shelf SAW acoustic filter is selected in Chapter 2. Similarly, for $f_S \in [3.5, 6.5]$ GHz, $f_{IF}^* = 2.5$ GHz, and 2.6 GHz off-the-shelf BAW acoustic filter is selected in Chapter 3.